UC San Diego

UC San Diego Electronic Theses and Dissertations

Title

Enhancement and analysis of nonlinear optical processes in designed microstructures

Permalink

https://escholarship.org/uc/item/3jw3r1h9

Author

Klemens, Guy

Publication Date

2007

Peer reviewed|Thesis/dissertation

eScholarship.org Powered by the California Digital Library
University of California

UNIVERSITY OF CALIFORNIA, SAN DIEGO

Enhancement and Analysis of Nonlinear Optical Processes in Designed Microstructures

A dissertation submitted in partial satisfaction of the
requirements for the degree
Doctor of Philosophy

in

Electrical Engineering (Applied Physics)

by

Guy Klemens

Committee in charge:

Professor Yeshaiahu Fainman, Chair
Professor Philip E. Gill
Professor Michael J. Holst
Professor Vitaliy Lomakin
Professor Kevin B. Quest

2007

Copyright
Guy Klemens, 2007
All rights reserved.

The dissertation of Guy Klemens is approved, and it is acceptable in quality and form for publication on microfilm:

_____

_____

_____

_____

_____

Chair

University of California, San Diego

2007

TABLE OF CONTENTS

LIST OF FIGURES

ACKNOWLEDGEMENTS

Portions of Chapter 3 are adapted from G. Klemens and Y. Fainman, "Optimization-based calculation of optical nonlinear processes in a micro-resonator", *Optics Express*, Vol. 14, No. 21, pg. 9864–9872 (2006) and G. Klemens and Y. Fainman, "Exact optimization-based analysis method applied to nonlinear processes in a multi-cavity micro-resonator", *2007 Conference on Lasers and Electro-Optics*.

VITA

1994	B. S., University of Maryland at College Park
1995	M. S., University of Illinois, Urbana-Champaign
1996-	Engineer, QUALCOMM, Inc, San Diego
2007	Ph. D., University of California San Diego

PUBLICATIONS

G. Klemens, V. Aparin and K. Gard, "The enhancement of static simulator package characterization through conductor segmentation," *IEEE Topical Meeting on Electrical Performance of Electronic Packaging*, 79-82 (1997).

G. Klemens, W. Nakagawa, R.C. Tyan and Y. Fainman, "Phase matching in anisotropic form-birefringent nanostructres," Nonlinear Optics of Nanostructured Materials, *OSA Annual Meeting*, Long Beach (2001).

G. Klemens, E. Ozaki and A. Tran, "Balanced, retractable mobile phone antenna," US Patent #6,239,755 (2001).

G. Klemens, M. Bhagat, D. Jessie and N. Frederick, "Analysis of circuit modeling of on-chip transformers," *Topical Meeting on Silicon Monolithic Integrated Circuits in RF Systems*, 167-170 (2004).

G. Klemens, C.H. Chen and Y. Fainman, "Design of optimized dispersive resonant cavities for nonlinear wave mixing," *Optics Express* **13**, 9388-9397 (2005).

G. Klemens and Y. Fainman, "Optimization-based calculation of nonlinear optical processes in a micro-resonator," *Optics Express* **14**, 9864-9872 (2006).

G. Klemens and Y. Fainman, "Exact optimization-based analysis method applied to nonlinear processes in a multi-cavity micro-resonator", *2007 Conference on Lasers and Electro-Optics* (2007).

ABSTRACT OF THE DISSERTATION

Enhancement and Analysis of Nonlinear Optical Processes in Designed Microstructures

by

Guy Klemens

Doctor of Philosophy in Electrical Engineering (Applied Physics)

University of California San Diego, 2007

Professor Yeshaiahu Fainman, Chair

The efficiency of nonlinear processes are limited by two effects: the small absolute scale of the nonlinear coefficients and the phase-mismatch effect. Micrometer scale structures with designed physical parameters offer a means to compensate for these limitations. This dissertation examines several types of structures that can provide more efficiency for a nonlinear processes than the same processes carried out in bulk crystal. Many of the structures use resonance to build the internal electric fields, and therefore increase the nonlinear response. Since numerous reflected waves exist within a resonant cavity, simple analysis methods for nonlinear processes do not apply. The reflected beams within the cavity interfere with each other as well as interact with the nonlinearity in the medium. No method of analysis for nonlinear processes in a resonator offered the accuracy and general applicability needed for these designs, so a new method is presented here. The new method is general and flexible, so that effects such as loss, gain, multiple nonlinear processes, and multiple cavities can be included in the modeling. The resulting field solution satisfies all of the imposed conditions and modeled effects, and is therefore as

accurate as the modeling equations. This method is then used to examine complicated structures that could not be accurately characterized before. Included are multi-cavity bistable devices and microcavities exhibiting modulation instability.

1

Introduction

1.1 Nonlinear Optical Processes

The field of nonlinear optics encompasses many processes in which photons interact with each other through the mechanism of the surrounding medium. As examples, some nonlinear processes are:

- Wavelength conversion. This includes the combination of two, three or more photons into one photon (second-, third- or higher harmonic generation), or the coupling of power between beams of different frequencies. Since lasers produce light in certain set wavelengths, these processes are used to create light in other wavelengths that may be needed, and to make tunable wavelength sources.

- Field-dependent propagation. This includes the Pockels effect, in which the refractive index of the medium (and therefore the wave speed) is affected by an electric field. The Kerr effect similarly adjusts the refractive index based on the beam intensity (proportional to the squared magnitude of the electric field). These effects, particularly the Pockels effect, are used to create high-speed optical modulators, phase-shifters and shutters.

- Optical limiters and multistable cavities. In these devices, the intensity of the input beam determines the output behavior. In an optical limiter, for example, the Kerr effect causes a filter structure to change from the passband to the stopband when the light intensity is high.

- Nonlinear signal propagation. As a wave packet of light travels through a fiber, it can be distorted by nonlinear effects. Alternatively, by tuning the appropriate parameters, it is possible for the nonlinear effects to compensate for the material dispersion. This creates a wave called a soliton, which maintains its shape even after long propagation distances.

The nonlinear aspect of the interaction of electromagnetic waves with matter is small and, in general, suppressed by phase mismatch effects. The first demonstration of a nonlinear optical effect may have been in 1875 when John Kerr showed that the refractive index of a cell filled with gas or fluid could be changed with an applied electric field [1]. The development of most useful nonlinear effects, however, came after the introduction of the laser, which provides a high-intensity light source. With high-intensity light, the small nonlinearity can yield significant output. Most nonlinear effects are still negligible due to interference effects (the phase-mismatch). This dissertation examines ways of enhancing nonlinear optical effects through the use of engineered microstructures. The creation of such microstructures has become possible with recent fabrication techniques, opening a new subfield in nonlinear optics for exploration. Structures that would increase nonlinear efficiency are presented and their design process is explained. Of equal prominence is the novel techniques that are shown for the analysis of the nonlinear processes in these structures.

1.2 Origin of Nonlinear Optical Effects

While the interaction of electric and magnetic fields as described by Maxwell's equations are linear, the interaction of those fields with matter contains a nonlinear component. Texts in nonlinear optics (e.g., [2, 3]) commonly use the model of the anharmonic oscillator to explain nonlinearity. In this analogy, the valence electron of an atom is bound to an immobile nucleus with a spring-like force. An impinging electric field moves the electron, converting the electric energy to kinetic energy. The moving electron then radiates an electromagnetic wave, returning the energy to the electric field. In a realistic spring model, the force is written as a power series of the displacement, including nonlinear terms. While the incoming electromagnetic field may be monochromatic, therefore, the radiated field has other frequency components. The nonlinear terms become increasingly small as the order increases, and therefore have an appreciable effect only for large displacements. In a general atom model, the electron is bound to a nucleus with an electric field of approximately $10^{10}\frac{V}{\mathrm{m}}$, so the electron displacement caused by most electromagnetic waves is not large enough to cause noticeable nonlinearity. Sunlight, for example, has an electric field less than $1000\frac{V}{\mathrm{m}}$ [2]. With the introduction of the laser in 1960 [4], light sources with high intensity and narrow wavelength bandwidth became available, and the study of nonlinear optical effects rose to prominence. For example, a 1 W beam with a diameter of 1 mm^2 has an electric field intensity of approximately $10^5\frac{V}{\mathrm{m}}$, and lasers are available with a higher peak power and can be focused into smaller spots.

1.3 Limiting Factors in Nonlinear Optics

Although electromagnetic waves interacting with atoms involves nonlinearity, those effects can be negligibly small due to limiting factors. For a centro-symmetric

material, some of the overall nonlinear constants are effectively zero. These are the processes that act on an even power of the electric field. For such processes, there is no preferred polarization for the generated wave. Neighboring atoms can therefore emit waves with opposite polarizations, leading to cancelation. Centro-symmetric crystals can, however, have nonzero nonlinear constants that involve odd powers of the electric field. For such processes, the sign, positive or negative, of the impinging field is preserved, so there is a preferred polarization for the output wave. Note that a crystal can be isotropic, meaning that the refractive index is the same in all directions, but still be non-centrosymmetric. An example is gallium arsenide, in which the gallium and arsenic atoms are arranged in a zincblende (diamond-like) structure ([3], p. 49). The structure appears symmetric in all directions, but the presence of two different atoms with different nonlinear responses negates the centro-symmetry described above.

The coefficients that describe the nonlinear processes are small, and become smaller with each order. This can be understood by considering the number of photons involved. In a second-order nonlinear process, two photons may be combined by an atom to produce a third photon with energy equal to the sum of the previous two. For this to occur, two photons must reach the atom simultaneously. More precisely, a photon will change the electron state, and then a second photon must enter the atom before the electron has returned to it's unperturbed state and radiated the first photon. Unless the photon field is dense (high electric field), the probability of this occurring is low. Each additional photon required for a nonlinear process lowers the probability of occurrence. For example in a third-order process after one photon is absorbed by an atom, two more must be absorbed before the first photon is radiated for the process to occur. Second-order nonlinear constants are generally of the order 10^{-13}–10^{-10} $\frac{\mathrm{m}}{V}$, while third-order nonlinear constants are in the range of 10^{-20}–10^{-22} $\frac{\mathrm{m}^2}{V^2}$. Despite the small value of these terms, any nonlinear process could be appreciable if the propagation distance is long

enough. There is, however, the further limiting effect of phase matching.

Phase mismatch stops energy from being transferred permanently between waves of different frequencies. The speed at which electromagnetic waves propagate through a material is frequency-dependent. The variation of a material's optical propagation properties with frequency is called dispersion. At some point in the propagation, the waves are in phase, while at a later point, the waves are exactly 180 degrees out of phase, and the in-phase and out-of-phase points continue periodically along the entire propagation distance. The generated wave from the nonlinear process will alternatively add constructively and destructively to the existing wave. As an example, in second-harmonic generation, energy will be transferred from the fundamental wave to its harmonic (wave with twice the frequency) at the in-phase points, and transfer from the harmonic to the fundamental at the out-of-phase points. The energy is shuttled between the two waves and the harmonic wave is unable to build. The distance between in-phase and out-of-phase points in a typical material is tens of micrometers, so only a negligible amount of energy is converted before it is returned to the fundamental. Due to the phase mismatch effect, a long interaction length will not, in general, improve nonlinear conversion efficiency. Only if the phase mismatch is compensated though some means will an increase in interaction length be worthwhile.

1.4 Microstructure fabrication

New methods of creating structures with micrometer feature sizes have opened new areas of study in nonlinear optics. While driven by the microelectronics industry, the advances in fabrication are also useful for optical structures. Optical wavelengths are on the order of one micrometer; with this level of detail in fabrication, we can design structures that use precise interference effects to control the response.

One fabrication task is the creation of thin films, for which there are several methods [5]. Evaporation-based methods are one common method. A sample of metal, such as gold or aluminum, is heated by a filament or an electron beam. The added kinetic energy leads the atoms to break from their crystal structure (melting) and then to escape from the metal into space (evaporation). A wafer of material such as silicon is exposed to the metal vapor. The metal vapor atoms cool on the wafer surface, which forms the metal layer. While slow, this process can create layers with thicknesses that are precise to the fraction of a micrometer. A deposition rate accuracy of 1 Å/second (10^{-10} m/second) is currently achievable. Chemical vapor deposition (CVD) is similar in principle, although with multiple sources. To deposit silicon dioxide, for example, silane (SiH_2) is evaporated in a furnace and mixed with oxygen to form silicon dioxide, SiO_2, with a hydrogen by-product. Many such chemical reactions are used in CVD systems, yielding some variety in the materials that can be deposited. Typical deposition rates are in the hundreds of Angstroms per minute, so vapor deposition is suited to layer thicknesses of less than a micrometer.

Many of the structures described in this dissertation are dependent upon deposition of multiple sub-micron layers. By specifying the thickness of each layer in a stack of a dozen or more layers, we can create a mirror with the complex reflection coefficient that is needed for an application. By adding enough layers, it is possible to meet reflection coefficient goals at multiple frequencies. The design of such mirrors is discussed in Chapter 4.

1.5 Numerical analysis of nonlinear processes in resonant microstructures

One of the significant contributions of this dissertation is the introduction of a new method for calculating the response of resonant cavities with nonlinear effects. The calculation method for the energy flow between electromagnetic waves of different frequencies through a nonlinearity has been well-established [6]. This method, which represents the nonlinear process through a set of coupled differential equations, is outlined in Section 2.2. This method applies, however, only for the case of waves co-propagating in an unbounded medium. This assumption is not valid for a resonant cavity. The one-dimensional resonant cavities examined here consist of a propagation length in a nonlinear crystal (or multiple materials) with mirrors placed at each end. These simple structures will contain multiple reflected waves traveling in both directions. These waves will add to form overall standing waves, and will interact through the nonlinearity. The early literature introduced a multiplier to the nonlinear process based on the field build-up in the cavity [7]. Later published research used a more sophisticated two-step method [8]. First the amplitude and phase distribution of the input waves are calculated inside the cavity as if the material were linear. Then those results are used as a distributed source to calculate the waves produced by the nonlinear process. While effective in some applications, this method will not work for others. For example, in a cavity in which the Kerr effect is used to produce bistability (described in Chapter 5), there is not a clear demarcation between input and output waves. Similarly, to calculate modulation instability in a resonant cavity (as in Chapter 6), a method is needed that simultaneously accounts for all the waves in the cavity and all the interference and mirror effects. Since we were interested in examining such applications, a new analysis method had to be developed. I found a technique used in circuit simulators to analyze resonant circuits

containing nonlinear elements. Taking the basic outline of this method and translating the details to electromagnetic waves propagating in nonlinear crystals, I wrote several programs to calculate the response of different types of nonlinear processes. The analysis method is presented in Chapter 3, and calculation results from the programs based on this method are subsequently shown.

1.6 Dissertation Overview

The goal of this dissertation is to examine the issues related to the design of structures to create efficient nonlinear processes. Most of the structures presented are micrometer-size in order to use interference effects that become significant when feature sizes are near, or less than, optical wavelengths. Besides design considerations, one of the main contributions is a new calculation method for analyzing nonlinear processes in resonant structures. The new method is then used to examine several applications that could not be sufficiently calculated with previous methods.

The subsequent chapters each examine an aspect or application of nonlinear optics in designed structures. First, Chapter 2 describes the mathematical analysis of nonlinear optical processes, including explicit statements of the limitations a designer faces. Two methods are then presented to overcome those limitations. One uses form birefringence to negate phase-mismatch, and the other uses an applied electric field to increase the nonlinear constant. The second method was carried out experimentally. Chapter 3 presents the new method for calculating the response of an optical nonlinear process in a resonant cavity. The method is explained and details of the implementation are examined. This includes a brief discussion of optimization methods used. Sample results are shown for a simple case. Chapter 4 is about the design of such structures. The conditions that must be met are explained, as are the effects of cavity length and mirror

reflection coefficients. A technique for the design of mirrors that meet the requirements is explained. Chapter 5 presents the use of the new analysis method for the calculation of the output of multi-stable devices. The analysis of these devices has been approximate in the previous literature, but is made more exact here. Furthermore, the new method allows for the design and analysis of new structures that could not be done with past methods. Chapter 6 examines modulation instability. This effect has been studied extensively, but not in a resonant cavity because techniques to do so were unavailable. Finally, a summary and concluding remarks are made in Chapter 7.

2

Techniques for Enhancement of Second-Harmonic Generation

2.1 Introduction

In second-harmonic generation (SHG), two photons of equal energy are combined to produce one photon [6]. From conservation of energy, the resulting photon has twice the energy of each input photon, which corresponds to doubling the frequency of the wave, or halving the wavelength. Efficient SHG was one of the first nonlinear processes demonstrated (in 1962 [9]) after the invention of the laser, which provides a high-intensity monochromatic light source. Soon after, the efficiency of the processes was improved with the addition of a resonant cavity [7].

This chapter presents methods to improve SHG efficiency from two aspects. The following section presents an analysis of nonlinear frequency mixing in electromagnetic waves. The derivation of the coupled differential equations that model energy exchange between waves through the medium nonlinearity is demonstrated. Part of the derivation is to quantify the limiting factor of phase mismatch. Section 2.3 presents a type of

structure that I analyzed to overcome phase mismatch through the use of engineered anisotropy. The principle of operation is explained and several examples are given. Another limiting factor is the small absolute value of the nonlinear constant of most media. Section 2.4 explains a possible method of creating an artificially large nonlinear coefficient. A series of experiments I conducted to test this effect is presented.

2.2 Overview of Nonlinear Optical Frequency Conversion

2.2.1 Energy Transfer and Phase Matching

This section presents an overview of the analysis of nonlinear interactions in propagating electromagnetic waves. The flow of energy between waves of different frequencies, the place of nonlinear constants in the calculations, and the effect of phase-mismatch will be explained. The analysis method used here is that of [6], which is also used in many nonlinear optics texts (such as [2, 3]). The analysis below is for an electromagnetic wave co-propagating with its harmonic, although the techniques can be extended to multiple waves at multiple frequencies.

The analysis of nonlinear effects in propagating electromagnetic waves begins with Maxwell's dynamic equations in a source-free region:

$$\nabla \times \mathbf{E} = -\frac{\partial \mathbf{B}}{\partial t}, \tag{2.1}$$

$$\nabla \times \mathbf{H} = \frac{\partial \mathbf{D}}{\partial t}, \tag{2.2}$$

where $\mathbf{E}$ is the electric field, $\mathbf{H}$ is the magnetic field, $\mathbf{D}$ is the electric displacement and $\mathbf{B}$ is the magnetic flux density. Boldface is used here to represent vector field quantities. Interaction with the surrounding medium is through the constitutive relations

$$\mathbf{B} = \mu_0 \mathbf{H} + \mathbf{P}_{\mathrm{m}}, \tag{2.3}$$

$$\mathbf{D} = \varepsilon_0 \mathbf{E} + \mathbf{P}_{\mathrm{e}}, \tag{2.4}$$

where μ_0 is the magnetic permeability of free space, ε_0 is the electric permittivity of free space, and $\mathbf{P}_\mathrm{m}$ and $\mathbf{P}_\mathrm{e}$ are the polarizations induced in the material by the magnetic field and the electric field, respectively. The dielectrics discussed here will not be magnetic materials, so we will assume that the magnetic polarization is uniformly zero. The electric polarization in dielectrics, however, can be strong and contains the nonlinear effects. To make these effects explicit, the electric polarization is generally expanded into the power series form

$$\mathbf{P}_\mathrm{e} = \varepsilon_0 \chi^{(1)} \mathbf{E} + \varepsilon_0 \chi^{(2)} \mathbf{EE} + \varepsilon_0 \chi^{(3)} \mathbf{EEE} + \ldots, \tag{2.5}$$

in which the linear effects are grouped into the coefficient $\chi^{(1)}$, the second-order nonlinear effects are grouped into the coefficient $\chi^{(2)}$, and similarly for the higher-order coefficients.

The quantities discussed to this point have all been in the frequency domain. The field variables and constants are all functions of frequency. A time-domain analysis is also possible, but at the expense of greater complexity since the frequency-domain multiplications are replaced by superposition integrals in the time domain. Since the processes are time-invariant, the operations can be further categorized as convolution integrals. Equation 2.5, for example, takes the form of a Volterra series (a series of convolution integrals)[2]:

$$\mathcal{P}_e(t) = \varepsilon_0 \int_0^t \mathcal{E}(t-\tau)\chi^{(1)}(\tau)d\tau + \varepsilon_0 \int_0^t \int_0^t \mathcal{E}(t-\tau_1)\mathcal{E}(t-\tau_2)\chi^{(2)}(\tau_1,\tau_2)d\tau_1 d\tau_2 + \ldots. \tag{2.6}$$

The relation between the time-domain and the frequency-domain representation can be clarified by considering a monochromatic wave:

$$\mathcal{E}(t) = e^{i\omega t}. \tag{2.7}$$

Using this definition in the first integral of Equation 2.6, for example, gives

$$\int_0^t \chi^{(1)}(\tau) e^{i\omega(t-\tau)} d\tau = e^{i\omega t} \int_0^t \chi^{(1)}(\tau) e^{-i\omega\tau} d\tau = e^{i\omega t} \chi^{(1)}(\omega), \tag{2.8}$$

where $\chi^{(1)}(\omega)$ is the Fourier transform of $\chi^{(1)}(t)$ evaluated at frequency ω. The subsequent terms of Equation 2.6 can be similarly transformed, although with two-dimensional and higher Fourier transforms. For the cases considered here we will assume that the nonlinear coefficients are relatively constant over the frequency ranges of interest. So, for example, $\chi^{(2)}(\omega_1, \omega_2) = \chi^{(2)}$. For monochromatic waves Equations 2.5 and 2.6 are therefore equivalent.

Combining Equations 2.1 and 2.2, and including 2.5, produces a wave equation,

$$\nabla^2 \mathbf{E} - \mu_0 \varepsilon_0 \varepsilon_r \frac{\partial^2 \mathbf{E}}{\partial t^2} = \mu_0 \frac{\partial^2 \mathbf{P}_{\mathrm{NL}}}{\partial t^2}, \tag{2.9}$$

in which $\mathbf{P}_{\mathrm{NL}}$ denotes the nonlinear polarization, and the linear terms have been combined into the constant $\varepsilon_r = 1 + \chi^{(1)}$. This equation only includes the electric field, $\mathbf{E}$, since the magnetic field is redundant. For a propagating wave, the electric and magnetic field amplitudes are fixed together at each point by the ratio

$$\frac{\mathbf{E}}{\mathbf{H}} = \frac{n}{Z}, \tag{2.10}$$

where n is the refractive index of the medium, and Z is the the impedance of free space (approximately 376.7 Ohms). Equation 2.9 could be written using $\mathbf{H}$, although since the nonlinearity is dependent on the electric field, the present form is more convenient.

For the specific case of second-harmonic generation, we assume a field made up of two frequencies, represented as

$$\mathbf{E}(z,t) = E_1(z)e^{i\omega t} + E_2(z)e^{i2\omega t} + E_1^*(z)e^{-i\omega t} + E_2^*(z)e^{-i2\omega t}, \tag{2.11}$$

in which ω and 2ω are the two frequencies and $*$ denotes complex conjugation. The assumption has also been made that the beams are plane waves traveling along the z-axis. Substituting the expansion of Equation 2.11 into Equation 2.9 yields the two coupled differential equations

$$\frac{d^2 E_1}{dz^2} = -\left(\frac{\omega}{c}\right)^2 (\varepsilon_1 E_1 + 2\chi^{(2)} E_1^* E_2), \tag{2.12}$$

$$\frac{d^2E_2}{dz^2} = -\left(\frac{2\omega}{c}\right)^2 (\varepsilon_2 E_2 + \chi^{(2)} E_1 E_1), \tag{2.13}$$

in which the speed of light in free space, $c = \frac{1}{\sqrt{\mu_0 \epsilon_0}}$, has been used, and ε_1 and ε_2 represent the relative permittivity of the medium at frequencies ω and 2ω, respectively. The solution of these two equations as a coupled system, given the initial values of E_1 and E_2, models the energy transfer between these two waves as they propagate. These equations can model second-harmonic generation, frequency downconversion, or the transfer of energy back-and-forth between the two frequencies. The procedure demonstrated here can be applied to other nonlinear processes, such as those involving beams with three or more wavelengths, or using higher nonlinearities such as $\chi^{(3)}$. Coupled differential equations similar to Equations 2.12 and 2.13 will be the result, although including more terms. Furthermore, terms representing power loss or gain could be added to the differential equations. While Equations 2.12 and 2.13 are adequate for numerical calculation, their physical meaning can be more clearly understood through approximation.

Second-order differential equations such as Equations 2.12 and 2.13 can be simplified in some cases by considering the waves to be constant-magnitude plane waves with a slowly varying amplitude modulation. The representation of the field at ω then becomes

$$E_1(z) = A_1(z)e^{-ikz}, \tag{2.14}$$

in which k is the wavenumber, equal to $\frac{\omega n}{c}$. In the slowly-varying envelope approximation, we assume that the overall envelope of amplitude is varying much more slowly than the plane wave. For example, a one nanosecond optical pulse in glass is approximately 100 centimeters long, while optical wavelengths are on the order of 1 micrometer. The pulse therefore contains approximately 10^5 waves. The envelope function, $A(z)$, is nearly constant in the reference plane of the wave, e^{-ikz}. Using this fact to discard negligibly

small terms, Equations 2.12 and 2.13 reduce to

$$\frac{dA_1}{dz} = -i\frac{\omega\chi^{(2)}}{cn_1}A_1^* A_2 e^{i\Delta_k z}, \tag{2.15}$$

$$\frac{dA_2}{dz} = -i\frac{2\omega\chi^{(2)}}{cn_2}A_1 A_1 e^{-i\Delta_k z}, \tag{2.16}$$

where n_1 and n_2 are the refractive indices at the two frequencies, related to the relative permittivity by $n = \sqrt{\varepsilon_r}$. These equations make explicit the phase mismatch term, $\Delta_k = k_2 - 2k_1$. They also indicate how the harmonic would grow in the case of phase matching, $\Delta_k = 0$. To make this relation clearer, we can apply the non-depleted pump approximation, whereby the pump amplitude, A_1, remains constant. Then from Equation 2.16, the harmonic amplitude grows as

$$A_2(z) = CA_1^2 z, \tag{2.17}$$

where the constant terms have been accumulated into C. This predicts a linear increase in the harmonic field and a quadratic increase in the harmonic intensity, since $I_1 = \frac{1}{2}\frac{n}{Z}|E_1|^2$. This rapid increase in the harmonic field, however, will only occur in a phase-matched case.

The phase mismatch, Δ_k in Equations 2.15 and 2.16, is caused by the dispersion (frequency-dependence of the refractive index) in the medium. The effect can be approximately quantified by integrating Equation 2.16 using the non-depleted pump approximation, but this time with the phase mismatch term remaining. The resulting amplitude variation for the harmonic wave is then

$$A_2(z) = DA_1^2 e^{-i\frac{\Delta_k z}{2}} \sin\left(\frac{\Delta_k z}{2}\right), \tag{2.18}$$

where D is another collection of constant terms. This relation shows that the harmonic amplitude will not be able to grow unrestricted, but will return to zero with regular periodicity. The distance between the point where the waves are in-phase and where

they are 180 degrees out of phase is commonly referred to as the coherence length. This corresponds in Equation 2.18 to the distance from a zero to a maximum, or $\frac{\pi}{\Delta_k}$. Some sources, such as [2], define the coherence length as the distance between points where the waves are in-phase. This corresponds to the distance between zero points (or between maxima) in Equation 2.18, or $\frac{2\pi}{\Delta_k}$. By either definition, the coherence length should be as long as possible, and the output of the nonlinear medium placed at a maximum, for efficient energy transfer.

2.2.2 Techniques of Phase Matching

The direction-based method to create phase-match used in 1962 [9] is still a common technique. In this method, an anisotropic nonlinear crystal is used, in which the polarization direction of the electric field determines the refractive index seen by a wave. It may be possible to orient the crystal such that the fundamental and the harmonic, polarized perpendicular to each other, experience the same refractive index at their respective frequencies. This method is limited in its application since it can only be applied to anisotropic crystals. Some materials such as gallium arsenide have relatively high second-order nonlinear coefficients [10], but are excluded from this technique because they are isotropic. Furthermore, the nonlinear coefficient can be direction-dependent, and the crystal orientation that produces phase matching may not have the highest nonlinear coefficient.

Another method of overcoming phase-mismatch is periodic poling, in which the crystal structure is modulated [11]. As explained in Section 1.3, crystals with a nonzero second-order nonlinearity are not centro-symmetric, so the generated field has a preferred polarization direction. Flipping the crystal structure also flips the polarization of the harmonic field, which is the equivalent of a 180 degree shift. In periodic poling, the crystal structure is flipped at the point that the phase-mismatch reaches 180 degrees,

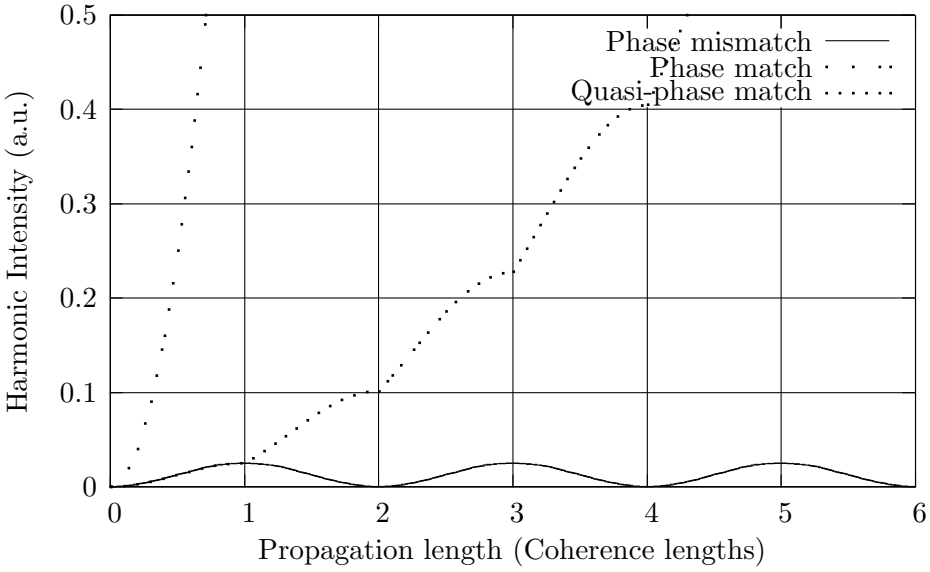

Figure 2.1: Harmonic intensity as a function of propagation length with different phase-match schemes for a fictional example case. Trends are calculated with approximate Equations 2.17 and 2.18.

thereby re-zeroing the mismatch. The harmonic field can then grow indefinitely, but note that this is not phase-match. By Equation 2.18, the harmonic amplitude growth is as a sinusoid. The crystal structure is flipped upon reaching the maximum, so rather than begin to decrease, the amplitude can continue rising. Figure 2.1 diagrams the harmonic amplitude in the crystal for the cases of phase-mismatch, phase-match, and periodic poling. In the case of periodic poling the harmonic amplitude does not grow as fast as when phase matched, but is not limited like the phase-mismatch case. For this reason, periodic poling is also called Quasi-Phase Matching. While simple in principle, fabricating such structures within tolerance is difficult [11].

2.3 Phase-Matching with Engineered Anisotropic Structures

2.3.1 Background

Consider two waves with perpendicular polarization propagating through a structure made up of two materials. The two materials alternate periodically along the wave front. If the period of the structure is much smaller than the wavelength of the waves, we can perform an approximate analysis to determine the refractive index acting on each wave.

By the boundary conditions of electromagnetic theory, the electric field polarized parallel to the periodic boundaries is continuous. We refer to this as the TE polarization, in analogy with the polarization names used in reflection and transmission. The overall permittivity for this polarization is defined by the equation $D_A = \varepsilon_{TE} E_A$, where the subscript A denotes an average across the entire structure. The average electric displacement is

$$D_A = \frac{D_1 d_1 + D_2 d_2}{d_1 + d_2}, \tag{2.19}$$

where D_1 and D_2 are the electric displacement magnitudes in materials one and two, respectively, and d_1 and d_2 are the widths of the two materials. By definition, $D_1 = \varepsilon_1 E_1$ and $D_2 = \varepsilon_2 E_2$. Using the assumption that the material period is much smaller than a wavelength, we can make the approximation that $E_1 = E_2$, then

$$\varepsilon_{TE} = \frac{\varepsilon_1 d_1 + \varepsilon_2 d_2}{d_1 + d_2}. \tag{2.20}$$

For the other polarization, called TM, the boundary condition states that the electric displacement, not the electric field, is continuous across the boundaries. We now use the equation $E_A = D_A/\varepsilon_{TM}$, to find the overall relative permittivity. Assuming the electric displacement, D, is not only continuous across the boundaries, but constant

throughout the structure, the relative permittivity is given by

$$\frac{1}{\varepsilon_{TM}} = \frac{\frac{d_1}{\varepsilon_1} + \frac{d_2}{\varepsilon_2}}{d_1 + d_2}. \tag{2.21}$$

Equations 2.20 and 2.21 show that with material choice and by adjusting the ratio of widths d_1 and d_2, a structure can be created where the refractive index at one of the polarizations and at frequency ω matches the refractive index at the perpendicular polarization and at frequency 2ω. Design parameters have been created that can tune a structure into a state of phase match for a particular process. This method was first proposed in 1975 [12], and demonstrated soon afterwards for a structure with 17 pairs of material layers [13]. Other subsequent published experiments have also been based on this phase-matching method [14, 15].

2.3.2 Rigorous Coupled Wave Analysis

When the structure feature size is not smaller than a wavelength, the approximate methods of Section 2.3.1 do not apply, necessitating the use of computational techniques. For the microstructures under consideration, the material periods will be the same order of magnitude in size as the wavelengths involved. To do the analysis, I used a technique called Rigorous Coupled Wave Analysis (RCWA).

RCWA is a computational technique applicable to electromagnetic propagation through a periodic medium that is based on periodic expansions [16, 17]. Assume wave propagation in the z-direction, and that the periodicity of the medium in the x-direction. The medium can be expressed by the Fourier series

$$\varepsilon(x) = \sum_{p=-\infty}^{\infty} \varepsilon_p e^{i\frac{2\pi}{\Lambda}px}, \tag{2.22}$$

where Λ is the period of the medium. The coefficients in Equation 2.22 are given by

$$\varepsilon_p = \frac{1}{\Lambda}\int_{\frac{-\Lambda}{2}}^{\frac{\Lambda}{2}} \varepsilon(x) e^{-i\frac{2\pi}{\Lambda}px} dx. \tag{2.23}$$

The propagating wave can also be given as a period expansion. The electric and magnetic fields are then represented as

$$\mathbf{E}(x,z) = \sum_{p=-\infty}^{\infty} \mathbf{S}_p e^{i\frac{2\pi}{\Lambda}px}, \tag{2.24}$$

$$\mathbf{H}(x,z) = \frac{1}{\eta_0} \sum_{p=-\infty}^{\infty} \mathbf{U}_p e^{i\frac{2\pi}{\Lambda}px}, \tag{2.25}$$

where the direction of the vector coefficients $\mathbf{S}_p$ and $\mathbf{U}_p$ are determined by the input wave polarization. The term η_0 in Equation 2.25 is the impedance of free space, which is included so that $\mathbf{S}_p$ and $\mathbf{U}_p$ will have consistent units. Unlike Equation 2.22, the coefficients of Equations 2.24 and 2.25 are unknown; they are the quantities to be solved.

To solve for the fields within the medium, the series of Equations 2.22, 2.24 and 2.25 are substituted into Maxwell's equations, resulting in one matrix state equation to solve. While the series have been shown as extending in terms from $-\infty$ to ∞, a practical implementation will truncate the series to $-M$ to M. Each series then has $2M+1$ terms, and the final matrix will be $2(2M+1)$ by $2(2M+1)$.

A straightforward implementation of the algorithm as it is described here will be ill-conditioned. This is due to the number of orders used to represent the series. Only the first few terms around $p = 0$ in Equations 2.24 and 2.25 represent propagating waves, which have complex exponentials. The other terms are evanescent waves with exponentially increasing or decreasing magnitude, with the size of the exponentials increasing with the number of terms. Ideally, the large, positive exponentials are paired with very small coefficients during the solution. In practice, however, these terms can be hundreds of orders of magnitude larger than the other terms, and accuracy is lost. The method of [18, 19] was used to overcome this difficulty. In this method, the matrix set-up is the same, although the matrix problem is then partitioned into smaller matrix equations, in which terms of similar magnitude are grouped.

My contribution was to rewrite this field-solver program for anisotropic materials, and then to create designs for efficient SHG. In the anisotropic case, the relative permittivity ε becomes a 3-by-3 matrix, with each element represented by a Fourier series. This significantly increased the size and complexity of the associated matrix equations. The design cases were built around using lithium niobate ($LiNbO_3$) as the nonlinear material. Lithium niobate is an anisotropic material with a relatively high nonlinear coefficient [10] that is widely used in the electronics industry. Several designs were simulated [20], although not fabricated due to the difficulty in creating satisfactory gratings in lithium niobate.

2.3.3 Designs Based on Lithium Niobate

The first design, shown in Figure 2.2, uses fluid with lithium niobate to create the periodic structure. Conversion in this case is from 1.5 micrometers to 0.75 micrometers. Since the period is larger than the wavelength of the beams inside the structure, the RCWA method is needed for calculation. The calculated refractive indices inside the structure for the two frequencies are shown in Figure 2.3 as a function of lithium niobate duty cycle. For fluid with a relative permittivity of 3.9, the indices match when 70% of each period is made up of lithium niobate. The point of phase matching varies with the permittivity of the filler, as shown in Figure 2.4. This may be useful if there is variation in the fabricated duty cycle of the lithium niobate. If the duty cycle differs from the designed value, the filler could be reformulated to change its permittivity.

A design using solid fillers is shown in Figure 2.5. No single material was found with dispersion properties that could produce phase-matching. Two materials were therefore used together. The calculated coherence length, plotted as a function of lithium niobate duty cycle in Figure 2.6, shows that the phase-matching point occurs when lithium niobate makes up 75% of each period.

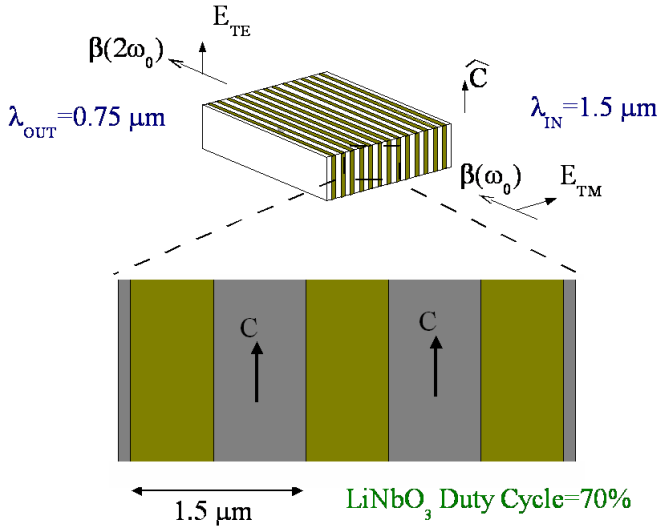

Figure 2.2: Structure for phase-matched SHG using lithium niobate and oil; the main crystal axis is shown by the vector C.

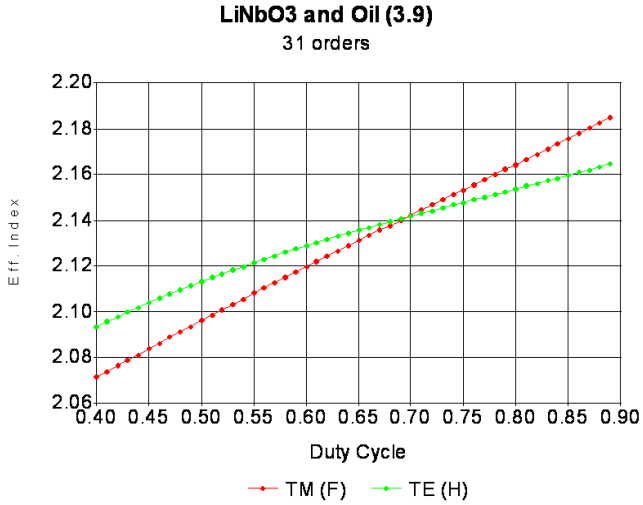

Figure 2.3: Refractive indices in the structure of Figure 2.2 for the TM and TE polarizations for waves of wavelength 1.5 and 0.75 micrometers, respectively. The relative permittivity of the filler oil is 3.9. Each point represents an RCWA run.

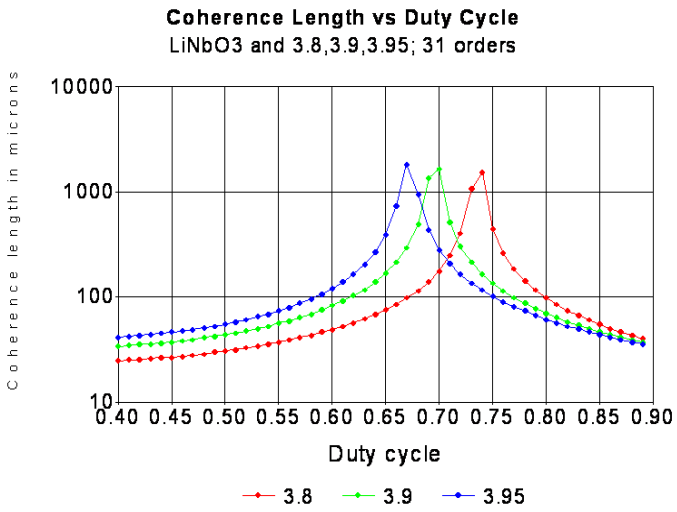

Figure 2.4: Coherence length as a function of lithium niobate duty cycle for several filler permittivities. The structure is as shown in Figure 2.2.

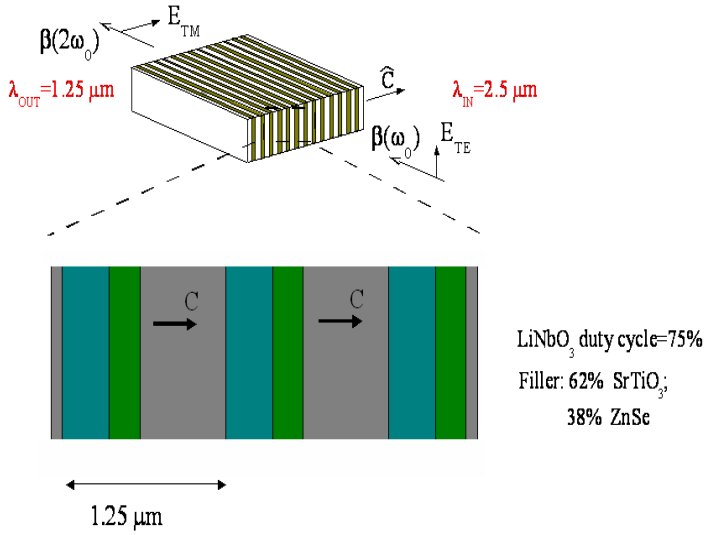

Figure 2.5: Structure for phase-matched SHG using lithium niobate and solid filler materials; the main crystal axis is shown by the vector C.

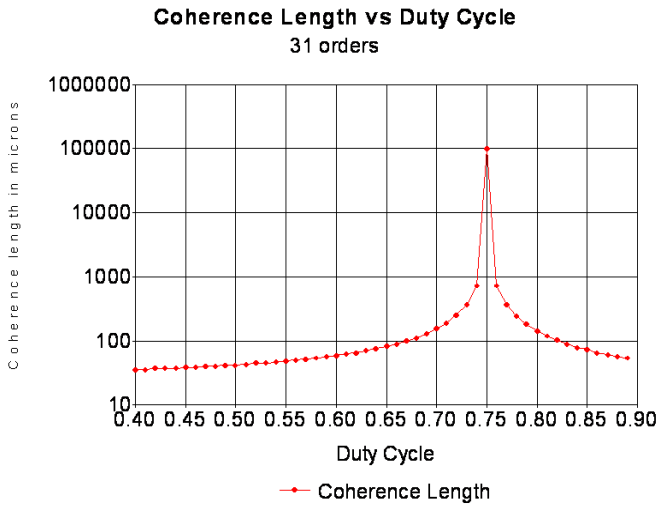

Figure 2.6: Coherence length as a function of lithium niobate duty cycle for the structure shown in Figure 2.5.

An alternative scheme for using solid filler is to alternate the materials with lithium niobate, as shown in Figure 2.7. In this case there are four widths that can be varied in each period. The plot of coherence length in Figure 2.8 shows that the phase-matching point is where lithium niobate makes up approximately 54% of each period.

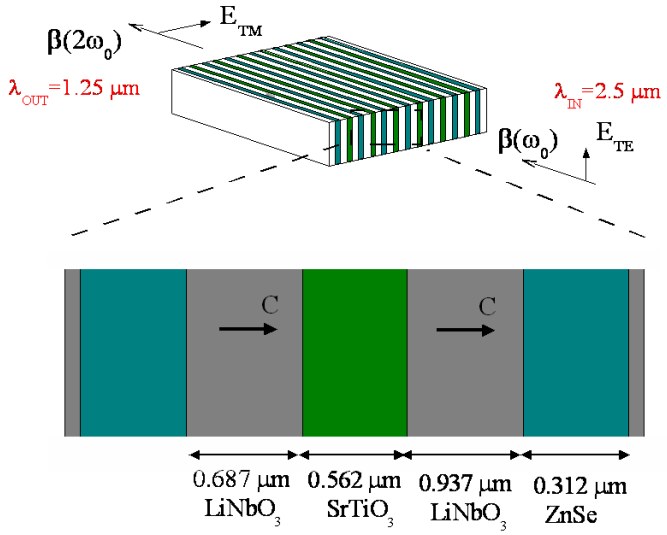

Figure 2.7: Structure for phase-matched SHG using lithium niobate and alternating solid filler materials; the main crystal axis is shown by the vector C.

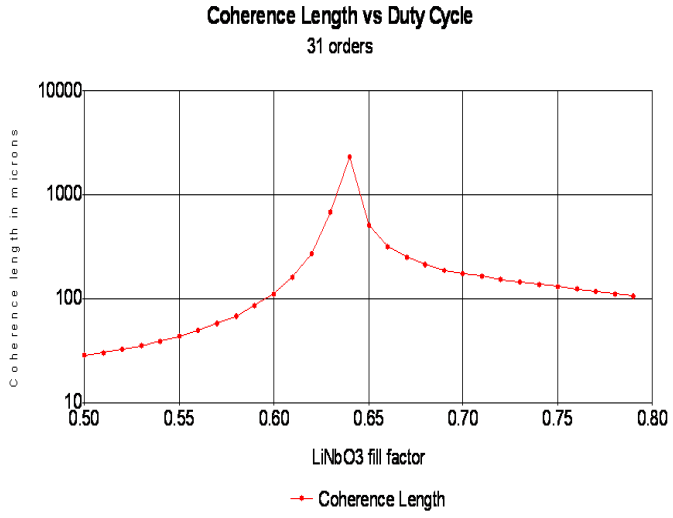

Figure 2.8: Coherence length as a function of lithium niobate duty cycle for the structure shown in Figure 2.7.

2.4 Creation of Artificial Second-Order Nonlinearity by Poling a Third-Order Nonlinear Material

This section examines an experiment I conducted to create an artificial second-order nonlinear coefficient in a material lacking one. To understand why a material may be lacking a second-order nonlinear coefficient, and how a third-order coefficient can be made into a second-order coefficient, we can examine the induced polarization in the material. This polarization can be written as a power series,

$$\mathbf{P}_{\mathrm{e}} = \varepsilon_0 \chi^{(1)} \mathbf{E} + \varepsilon_0 \chi^{(2)} \mathbf{EE} + \varepsilon_0 \chi^{(3)} \mathbf{EEE} + \ldots, \tag{2.26}$$

where the χ terms are the coefficients of first, second and third orders. A physical limitation to consider is that the second-order nonlinear coefficient, $\chi^{(2)}$, is zero in a centro-symmetric material. Consider a centro-symmetric material in which the electric field is aligned with the z-axis. Then the nonlinear polarization, $\mathbf{P}^{(2)} = \varepsilon_0 \chi^{(2)} \mathbf{EE}$, is also polarized in the positive-z direction. Now arbitrarily switch the z-axis by 180 degrees. The electric field magnitude now has a negative value, although since it is squared, the nonlinear polarization is still positive. The direction defined as positive, however, is now directly opposite to the previous case. Expecting the physical quantities to be the same in any arbitrarily declared axis-orientation, the two nonlinear polarizations must be equal, so $\mathbf{P}^{(2)} = -\mathbf{P}^{(2)}$, which is true only if $\mathbf{P}^{(2)} = 0$. A physical explanation is that with no preferred direction of second-order nonlinear polarization, one atom or set of atoms will produce a field polarized in one direction, and the next atoms may produce a field in the opposite direction, leading to cancelation. Materials with a second-order nonlinearity therefore comprise a subset of nonlinear materials. All nonlinear materials will have a third-order nonlinear coefficient, although that coefficient may be small.

The application of a constant electric field can create a second-order nonlinear

coefficient in a centro-symmetric material. In such a case, the nonlinear polarization takes the form

$$\mathbf{P}_{NL} = \varepsilon_0 \left(\chi^{(3)}\mathbf{E}_0\right)\mathbf{EE}, \tag{2.27}$$

with $\mathbf{E}_0$ being the applied constant electric field. Parenthesis have been placed in Equation 2.27 to highlight the term that becomes the effective second-order nonlinear coefficient,

$$\chi^{(2)}_{eff} = \chi^{(3)}\mathbf{E}_0. \tag{2.28}$$

Physically, the constant electric field distorts the atomic structure and breaks the centosymmetry [21].

This effect has been used to create SHG in PLZT, a centro-symmetric material. PLZT, $Pb_{1-x}La_x(Zr_yTi_{1-y})_{1-x/4}O_3$, is a material widely used in the electronics industry in applications such as digital displays. This material has the advantages of being transparent for the visible light spectrum, a fast response time, and a wide range of operating temperatures [22]. Reflected SHG was created using PLZT in [23]. In that work, electrodes were placed on the PLZT surface, with a gap of 60 micrometers between them. A beam of 1.064 micrometer wavelength was directed at the space between the electrodes, and the reflection examined for the harmonic. The experiment I conducted used transmission through the PLZT sample, rather than reflection from its surface. During reflection, the field penetrates the surface only a few nanometers, leading to a weak nonlinear output. Transmission through the bulk of the crystal has the potential to yield a larger output.

2.4.1 Experimental Setup

The experiment was designed in a straightforward manner of source-device-detector. A tunable, high-power, pulsed laser was used for the light source. The beam

was passed through an attenuator and a polarizer, then focused with a lens into a point at the sample. After the sample was another lens to collect the diverging light, and a filter to block the infra-red input beam. A silicon detector was used, which normally would not detect radiation with wavelengths larger than approximately one micrometer, which includes the input wave. The input beam had a high enough intensity, however, to create a response in the detector. The infra-red filter blocked this effect by attenuating the remaining input beam leaving the sample. The signal from the silicon detector was sent to a lock-in amplifier that was synchronized with the pulsed laser source. Only a signal at the frequency of the source (1 kHz) would be displayed by the lock-in amplifier. This adds immunity to ambient light sources such as displays and room lights.

A sample of PLZT approximately 1 mm thick with metallization on the broad-sides was used. The PLZT composition was 9/65/35 (ratio of La/Zr/Ti), which is similar to that used in [23]. The propagation distance was approximately 3 mm. Electrodes were attached to the metallic sides in order to apply a DC voltage to create the static electric field. The sample was also positioned on a temperature controlled surface to measure temperature-dependent effects.

2.4.2 Experimental Results

Second-harmonic generation was detected with the application of a voltage to the sample. The input waves had a wavelength of 1300 nm, well out of the visible range. Upon applying a voltage, the harmonic at 650 nm would clearly appear as a red spot, and would grow brighter as the voltage was increased. Sparking would occur at approximately 600 V applied voltage, so the measurements were taken below that level. The refractive index as a function of frequency for this sample is unknown.

The variation of the SHG power detected with the applied voltage is shown in Figure 2.9. The increase in SHG power with the applied voltage is as expected from

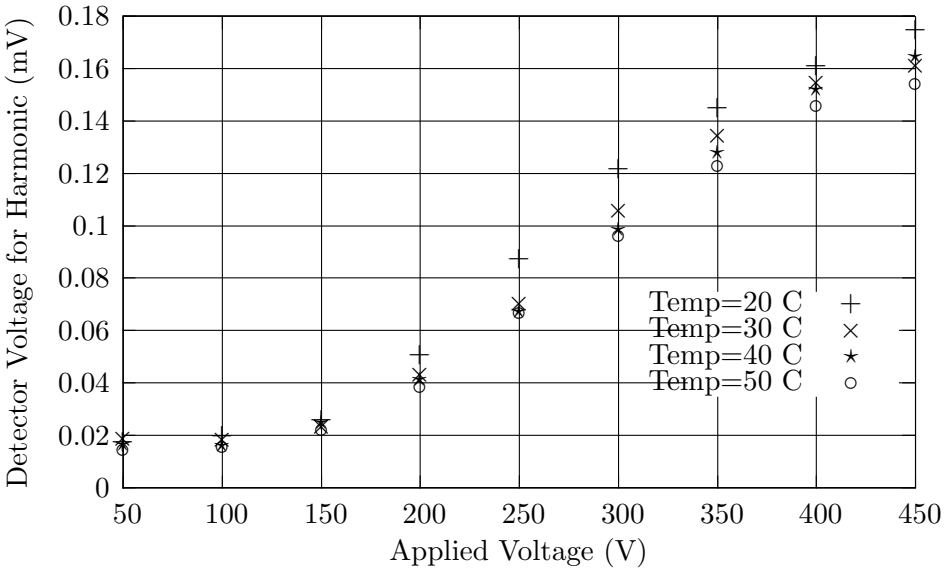

Figure 2.9: Detected SHG vs applied voltage, for different temperatures. The input wavelength is 1300nm.

Equation 2.27. Different temperature points are included, showing a small increase in SHG power as the temperature of the sample is lowered. From this limited data set, the origin of this difference is not known. The lower temperature may be changing the refractive index of the sample in a way to improve phase matching.

The effect of input frequency is shown in Figure 2.10. While the source frequency was adjustable, the power would vary significantly for different frequencies. The data in Figure 2.10 have therefore been normalized for each input wavelength. The highest conversion occurs at 1330 nm.

The final plot of Figure 2.11 shows the dependence of the output SHG on the input wave power. In this case, a variable attenuator was used to create the variation in input beam power. The wavelength and temperatures were held constant at 1300 nm and 30 C, respectively, and the input power was measured with a detector that gives time averaged power. Figure 2.11 therefore shows power in milliwatts. Since the source output is actually in .1 psec pulses, the peak power can be in the gigawatts. The plot

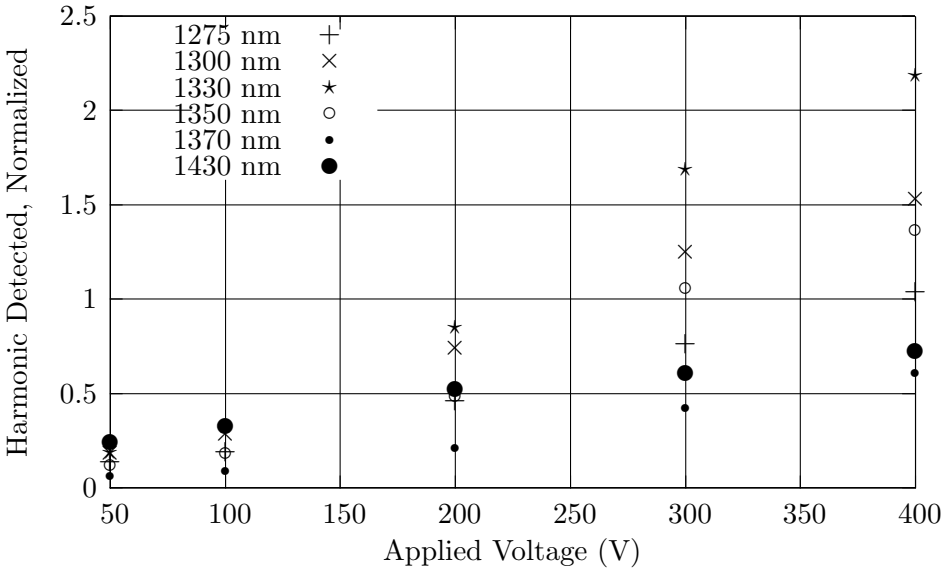

Figure 2.10: Detected SHG vs applied voltage, for different wavelengths. The temperature is 30 C. The data have been normalized to account for variations in source power with wavelength.

shows a linear increase in SHG power with input power, which is expected from Equation 2.27.

2.5 Summary

Two methods for the enhancement of optical second-harmonic generation have been analyzed and presented here. The purpose of these methods is to overcome two limiting factors in nonlinear optical processes: (1) the phase matching problem, and (2) the small nonlinear coefficients. The first method uses a periodic structure to create anisotropy that is specifically designed to create a phase match. The designer has some freedom in choosing materials and the direction of propagation. The case of lithium niobate was presented, with several designs shown that meet the phase matching criteria. The analysis required numerical simulation using RCWA in a custom-written program. The second method is an experimental investigation into the creation of an artificial

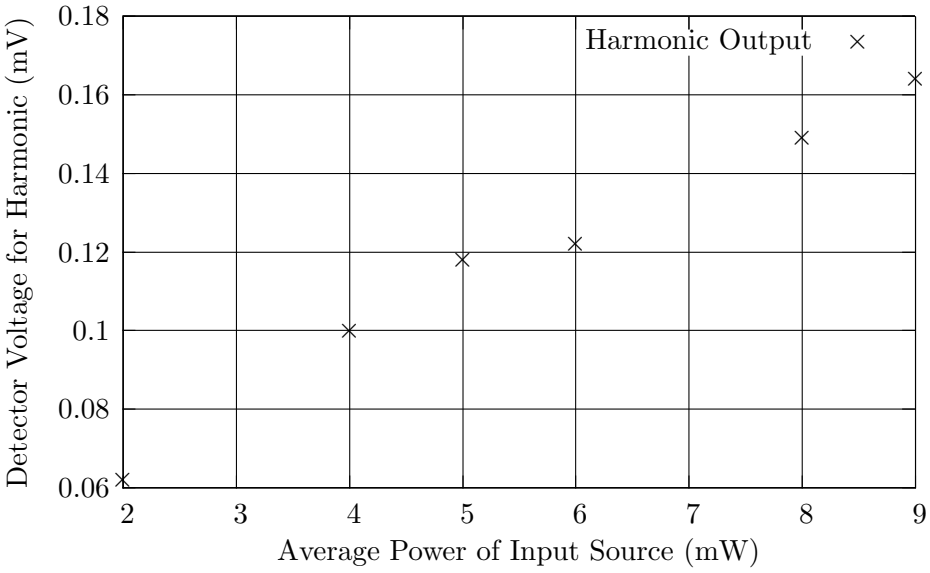

Figure 2.11: Detected SHG vs Input Power. The input wavelength is 1300nm; temperature 30 C; 350 V applied voltage.

second-order nonlinearity in a third-order nonlinear material. PLZT was used in this experiment, with electrodes creating a constant electric field through an applied voltage. Second-harmonic light was produced, and was shown to be voltage-dependent. While the SHG power was not high, this setup could be used to create a modulated SHG beam, with the voltage providing the modulation.

3

Optimization-Based Analysis of Nonlinear Optical Processes in Resonant Structures

3.1 Introduction

Resonant cavities are a commonly used way to enhance the relatively weak nonlinear optical effects. Such structures are typically constructed by two mirrors facing each other, with the volume between the mirrors making up the cavity. At resonance, the cavity creates a significant increase in the nonlinear output. An overview of some of the relevant properties of resonant cavities is provided in Appendix I. Second-harmonic generation (SHG) in a cavity was described in 1962 [6] and measured experimentally soon after [7].

The analysis methods used have been approximate and not generally applicable to all nonlinear processes. Early papers in the field used an analytically derived multiplier, typically related to the cavity finesse, to approximate the nonlinear conversion

[7, 24]. A more sophisticated method based on optical transfer matrices was later developed [8, 25, 26]. In this method, the field distribution of the input beam inside the cavity is first calculated as if the cavity material is linear. That field is then used to calculate a nonlinear polarization for each point. Finally, the output from the cavity is found by assuming the nonlinear polarization to be a distributed source. This method has the advantage that it can model a cavity made up of any number of layers. It works well for the cases of second or third harmonic generation, where clear input and output waves are defined, and the transfer of energy is from the input beam to the output beam. For processes that transfer energy between multiple beams, however, this method may not be applicable. This method is also not applicable to cases where the nonlinear effects alter the initial linear solution. An example is the Kerr effect, in which the refractive index is changed by the light intensity.

A new method for the analysis of nonlinear processes inside resonant cavities has been developed [27] and is presented here. This method is general since it can be applied to any nonlinear optical processes. All of the nonlinear and cavity effects are simultaneously satisfied to give the steady-state field values for all of the frequencies involved inside and outside the cavity.

3.2 Representation of Nonlinear Electromagnetic Processes with Differential Equations

The reduction of Maxwell's equations of electromagnetics to coupled differential equations was demonstrated in Section 2.2. Using the specific example of SHG, the complex field amplitude at the fundamental frequency ω, E_1, and the amplitude at the harmonic frequency 2ω, E_2, were included in Maxwell's equations along with the definition of electric displacement that was expanded to include the second-order nonlinear

term:

$$D = \varepsilon_0 \varepsilon_r E + \varepsilon_0 \chi^{(2)} EE. \tag{3.1}$$

The equations of amplitude transfer are

$$\frac{d^2 E_1}{dz^2} = -\left(\frac{\omega}{c_0}\right)^2 (\varepsilon_1 E_1 + 2\chi^{(2)} E_1^* E_2), \tag{3.2}$$

$$\frac{d^2 E_2}{dz^2} = -\left(\frac{2\omega}{c_0}\right)^2 (\varepsilon_2 E_2 + \chi^{(2)} E_1 E_1), \tag{3.3}$$

where ε_1 and ε_2 are the relative permittivities at the fundamental and the harmonic, respectively. These equations are sufficient for numerical calculation of SHG over some propagation length. As shown in Section 2.2, these equations can be significantly simplified by use of the slowly varying envelope approximation, in which the field amplitudes are represented as plane waves with amplitude modulation functions:

$$E(z) = A(z) e^{-ikz}, \tag{3.4}$$

in which k is the wavenumber. If the envelope function $A(z)$ varies slowly relative to the plane waves, then some small terms can be discarded and Equations 3.2 and 3.3 simplify to

$$\frac{dA_1}{dz} = -i \frac{\omega \chi^{(2)}}{c_0 n_1} A_1^* A_2 e^{i\Delta_k z}, \tag{3.5}$$

$$\frac{dA_2}{dz} = -i \frac{2\omega \chi^{(2)}}{c_0 n_2} A_1 A_1 e^{-i\Delta_k z}, \tag{3.6}$$

where $\Delta_k = k_2 - 2k_1$. This form of the differential equations can significantly decrease the computational complexity of finding the solution.

As a second example we can consider the case of a parametric process. This involves three frequencies, such that $\omega_1 = \omega_2 + \omega_3$. The beams are called the pump, signal and idler, although which frequency is assigned which name varies with the application. Typically, the pump and idler beams are input in the the nonlinear crystal in order to produce the signal beam. In other cases, only the pump is input into the nonlinear

crystal, and the idler builds spontaneously. The output is then the signal beam, with some energy unavoidably lost to the idler. Using the same procedure as was done for SHG, the coupled differential equations representing this process are

$$\frac{d^2E_1}{dz^2} = -\left(\frac{\omega_1}{c_0}\right)^2(\varepsilon_1 E_1 + 2\chi^{(2)}E_2E_3), \tag{3.7}$$

$$\frac{d^2E_2}{dz^2} = -\left(\frac{\omega_2}{c_0}\right)^2(\varepsilon_2 E_2 + \chi^{(2)}E_1^*E_3), \tag{3.8}$$

$$\frac{d^2E_3}{dz^2} = -\left(\frac{\omega_3}{c_0}\right)^2(\varepsilon_3 E_3 + \chi^{(2)}E_1^*E_2). \tag{3.9}$$

In the simplified form obtained by using the slowly varying envelope approximation, these equations are

$$\frac{dA_1}{dz} = -i\frac{\omega_1\chi^{(2)}}{c_0n_1}A_2A_3e^{i\Delta_k z}, \tag{3.10}$$

$$\frac{dA_2}{dz} = -i\frac{\omega_2\chi^{(2)}}{c_0n_2}A_1^*A_3e^{-i\Delta_k z}, \tag{3.11}$$

$$\frac{dA_3}{dz} = -i\frac{\omega_3\chi^{(2)}}{c_0n_3}A_1^*A_2e^{-i\Delta_k z}, \tag{3.12}$$

where $\Delta_k = k_1 - k_2 - k_3$. Other nonlinear processes could also be described through similar systems of coupled differential equations. These equations, however, only apply to co-propagating beams in an infinite medium. The effects of multiple interfering waves, as in a resonant structure, have not yet been included.

3.3 Optimization-Based Analysis Method

This analysis is based on the consideration of what conditions must be satisfied for a set of field values to be correct. It is assumed that all transients have dissipated and inside the cavity for each frequency there is one overall right-traveling wave and one overall left-traveling wave. The case of a simple cavity is shown in Figure 3.1. The fields on each side of the cavity are represented by the vectors $\mathbf{E_1}$ and $\mathbf{E_3}$. The fields can be translated across the cavity boundary from the inside to the outside using matrix $\mathbf{M}$.

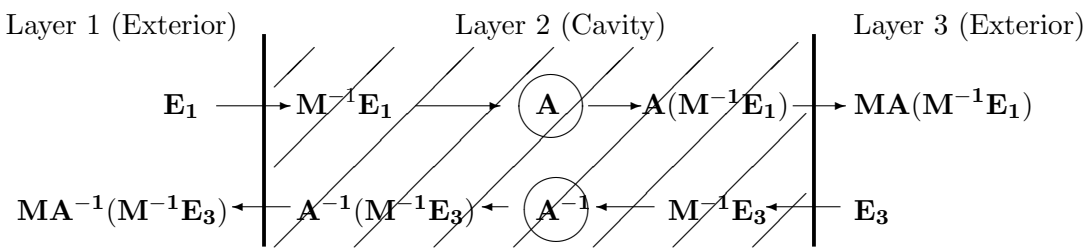

Figure 3.1: Field analysis of a single cavity. Analysis from left-to-right or right-to-left will produce self-consistent results for a correct set of vectors.

The field vector $\mathbf{E_1}$ is translated across the mirror into the cavity, and then propagated across the cavity using operator $\mathbf{A}$. For the linear case, $\mathbf{A}$ is a phase-transfer matrix. In the nonlinear case, $\mathbf{A}$ will be a set of differential equations. The resulting vector is then translated across the mirror on the other side of the cavity and compared to $\mathbf{E_3}$. The vector $\mathbf{E_3}$ is similarly translated through the cavity and the result compared with $\mathbf{E_1}$. For a self-consistent set of vectors $\mathbf{E_1}$ and $\mathbf{E_3}$, translation through the cavity of each vector will yield the other vector. Then all of the boundary conditions as well as the nonlinear differential equations are satisfied. If the vectors do not match after translation through the cavity, then an error term can be defined and the vectors adjusted to minimize the error.

This method is conceptually similar to that used by harmonic balance solvers in nonlinear circuit design. In that method current values are assumed for all the circuit branches, and then the resulting voltages found. For the linear elements, the voltages are found using frequency domain techniques, while time-domain methods may be used for the nonlinear elements. When all the voltages that are directly connected match, then the set of currents is correct. Optimization methods are used to iterate the currents in order to find minimize the voltage differences and find the correct values. This method has yielded significant improvements in simulation time and accuracy over transient-

analysis methods [28].

In nonlinear optics, this method has aspects that make it preferable to a time-domain analysis method. By working in the frequency domain, the nonlinear effects can be modeled algebraically, rather than with convolution integrals that would be required for a time-domain analysis, as given by Equation 2.6. A time-domain solution solves for all frequency components, while a frequency-domain solution focuses on a small number of frequencies. In the cases described here, the inputs are assumed to be a finite number of monochromatic waves, and the possible output waves are also a set of waves at known frequencies. A general time-domain solution is therefore inefficient. A time-domain analysis of a resonant cavity also has the disadvantage of a long run time as the transients decay. For a resonator with high-reflectivity mirrors, the simulation may have to be run for a time interval equivalent to hundreds of passes through the cavity. Besides a long run-time, this can reduce accuracy by allowing small errors to accumulate. Further complicating a time-domain analysis is the interference between reflected waves in the cavity. All of the waves contribute to the nonlinearity and must therefore be included. Once steady-state is reached, however, the fields inside the cavity combine to form one single wave traveling in each direction for each wave. For applications in which the transient response is required, a time-domain simulation may be unavoidable. For a microcavity, however, the transient may be over in less than a nanosecond. For these cases the method of this chapter is an efficient solution technique.

3.3.1 Application to Second-Harmonic Generation

As an example, the analysis method is demonstrated here for the case of second-harmonic generation. We assume a known incident wave of frequency ω, and wish to find the transmitted and reflected waves for both ω and 2ω. This gives four complex unknowns, or eight total unknowns considering real and imaginary or magnitude and

angle. The cavity properties, including the length, refractive index at ω and 2ω and mirror reflection coefficients are assumed to be known. The problem is diagramed in Figure 3.2. The vectors $\mathbf{E_1}$ and $\mathbf{E_3}$ have each been divided into two vectors, one for each frequency. The first component of each vector is the complex magnitude of the right-traveling wave, and the second component is the complex magnitude of the left-traveling wave. On the left side of the cavity, immediately outside the mirrors, are vectors $\begin{bmatrix} A_+^\omega \\ A_-^\omega \end{bmatrix}$ and $\begin{bmatrix} 0 \\ A_-^{2\omega} \end{bmatrix}$, representing the incident and reflected wave at ω and the reflected wave at 2ω. On the immediate right side of the cavity are the vectors $\begin{bmatrix} B_+^\omega \\ 0 \end{bmatrix}$ and $\begin{bmatrix} B_+^{2\omega} \\ 0 \end{bmatrix}$, representing the transmitted waves at ω and 2ω. Of the values listed, only the incident wave magnitude, A_+^ω, is known in advance.

Once an initial value has been assumed for all of the unknowns, the first step in the analysis is to translate the external field values across the mirrors into the cavity. This can be done using optical transfer matrices. From the electromagnetic boundary conditions, the tangential electric field is the same on both sides of the boundary, as is the tangential magnetic field. These conditions can be converted into a matrix equation. For example, the external field vector for the wave at ω on the left side of the cavity can be translated across the mirror to find the internal field values by

$$\begin{bmatrix} A_+^\omega \\ A_-^\omega \end{bmatrix} = \frac{1}{\tau} \begin{bmatrix} 1 & \rho \\ \rho & 1 \end{bmatrix} \begin{bmatrix} \widetilde{A_+^\omega} \\ \widetilde{A_-^\omega} \end{bmatrix}, \tag{3.13}$$

with ρ and τ representing the reflection and transmission coefficients, respectively, of the mirrors. A tilde is used to denote values inside the cavity. For propagation from a medium of refractive index n_1 to a medium of refractive index n_2, the reflection and

transmission coefficients are given by

$$\rho = \frac{n_1 - n_2}{n_1 + n_2}, \quad \tau = \frac{2n_1}{n_1 + n_2}. \tag{3.14}$$

These mirror coefficients can be made complex to model some mirrors, and the coefficients can be recalculated at each frequency to model dispersion.

Once the field vectors have been translated into the cavity, the next step is to propagate the appropriate values across the cavity using the coupled differential equations. In this case, $\widetilde{A_+^{\omega}}$ and $\widetilde{A_+^{2\omega}}$ can be propagated from the left side of the cavity to the right side using Equations 3.2 and 3.3, or using Equations 3.5 and 3.6. The resulting fields are then compared to $\widetilde{B_+^{\omega}}$ and $\widetilde{B_+^{2\omega}}$, yielding a residual term consisting of the square of the difference. Similarly, $\widetilde{B_-^{\omega}}$ and $\widetilde{B_-^{2\omega}}$ are propagated from right to left across the cavity, and then compared to $\widetilde{A_-^{\omega}}$ and $\widetilde{A_-^{2\omega}}$. The differences are added to the residual.

The starting values for the external field vectors are then adjusted, with the exception of A_+^{ω}, to reduce the residual. Once the residual has been made satisfactorily small, then the field values satisfy all of the relevant boundary conditions and the nonlinear equations. The stopping point at which the residual is sufficiently small varies with applications. Generally, the residual target should be at least an order of magnitude smaller than the smallest resulting field value.

For this case, the effects of counter-propagating beams on each other have been left out. This allowed the separation of the propagation step into left-traveling and right-traveling equations, which are solved independently. In second-harmonic generation, the counter-propagating waves are always phase mismatched, so no energy transfer can build up. For other nonlinear processes, such as the Kerr effect, the total field, which is the sum of the left- and right-traveling waves, must be found at each point to use in the differential equations.

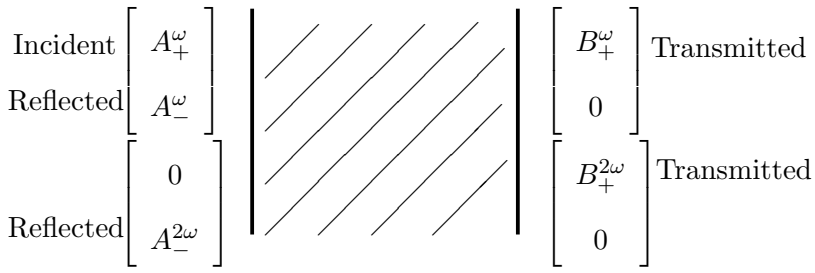

Figure 3.2: Variables in the case of second-harmonic generation in a cavity.

3.3.2 Non-plane Wave Application

The preceding has assumed plane-wave solutions to the wave equation, although other configurations are possible. In a waveguide, for example, the electric and magnetic fields in a cross-section are in non-uniform distributions called modes. Each mode propagates along the waveguide at its associated wave speed. The equations of this chapter can therefore be applied to waveguide modes as well as to plane waves. In the case of plane waves, the complex amplitude represents the electric field at every point on the wave front. For a waveguide mode, the complex amplitude denotes the amplitude of the field distribution in the cross-section. Since the electric field is non-uniform, the amplitude could represent the peak or the RMS of the field magnitude within the mode. Besides the significance of the mode amplitude, there are other factors to consider.

When considering waveguide propagation, the extent of mode overlap can affect the efficiency of the nonlinear interaction. In the case of uniform plane waves, the waves are all assumed to overlap completely. For a waveguide, in contrast, two modes may reach peak magnitudes at different parts of the cross-section, so that there is little overlap. Since the field distribution of the modes is constant with propagation, it is possible to quantify the overlap with multiplicative factors. For two mode distributions, an overlap

factor, C_M, can be defined as

$$C_M = \frac{\int\int E_1(x,y)E_2(x,y)dxdy}{\int\int E_1(x,y)dxdy \int\int E_2(x,y)dxdy}, \tag{3.15}$$

where the cross-section is in the $x-y$ plane and the integrations are carried out over the entire plane. This factor modifies the nonlinear coefficient used in the differential equations.

While in the plane wave case there is one wave for each frequency, a waveguide can contain multiple modes at each frequency. In the absence of a perturbation in the waveguide cross-section, there is no energy transfer between modes at one frequency. The nonlinearity, however, can couple any combination of modes at different frequencies. The modes travel at different speeds, so each combination will have its own phase mismatch, and the coupling factor defined in Equation 3.15 will also determine which combination of modes is significant. As an example, consider SHG in a waveguide with one fundamental mode, A_1, and two harmonic modes, B_1 and B_2. The set of differential equations modeling the coupling between the three modes is

$$\frac{dA_1}{dz} = -i\frac{\omega\chi^{(2)}}{c_0 n}\left(C_{11}A_1^* B_1 e^{i\Delta_{11}z} + C_{12}A_1^* B_2 e^{i\Delta_{12}z}\right), \tag{3.16}$$

$$\frac{dB_1}{dz} = -i\frac{2\omega\chi^{(2)}}{c_0 n}C_{11}A_1 A_1 e^{-i\Delta_{11}z}, \tag{3.17}$$

$$\frac{dB_2}{dz} = -i\frac{2\omega\chi^{(2)}}{c_0 n}C_{12}A_1 A_1 e^{-i\Delta_{12}z}, \tag{3.18}$$

where C_{11} and C_{12} are the overlap factors between the fundamental mode and each harmonic mode, and Δ_{11} and Δ_{12} are the phase mismatch terms defined similarly. Other than these modifications to the propagation equations, the solution can proceed as for plane waves.

3.3.3 Optimization Methods

There are several algorithms that can be used to adjust the solution vectors in order to minimize the residual [29, 30]. The optimization algorithms differ in computational complexity and in their efficiency when applied to a particular residual surface. In the cases dealt with here, the residual surface is continuous and derivatives exist at every point, which allows for the use of efficient optimizers. The derivative of the residual surface with respect to each of the unknowns is not, however, analytically determined. The derivatives are estimated by sampling the residual function at different points.

While optimization functions are available that can be inserted into a program as black boxes, two simple optimization algorithms are explained here. These methods were used for early versions of the programs that generated the results presented here, and their explanation offers some insight into optimization. For problems with more than a few unknowns, or for which each call to the residual function is computationally expensive, an efficient optimization library should be used instead.

In the steepest descent method, the search in the variable space is done along the gradient. The algorithm can be summarized in these steps:

1. For the point $\mathbf{P}$, find the gradient vector $\mathbf{V}$
2. Search along the line defined by $-\mathbf{V}$ for the point with the lowest residual, which becomes the new point $\mathbf{P}$.
3. The steps are repeated until a point is found with an adequately low residual.

For each step the new gradient vector will be perpendicular to the previous one, so that

$$\mathbf{V_2^T V}_1 = 0, \tag{3.19}$$

where a superscript T denotes transpose.

This method works well for circular bowl-shaped residual surfaces. For a perfectly circular bowl-shaped surface, the direction of maximum gradient would point directly to the center point with the lowest residual. When the surface is not circular, however, the gradient line will miss the lowest residual point. This leads to a zig-zag pattern as the test point approaches the optimal point. For such cases, the conjugate gradient method can speed convergence.

In the conjugate gradient method, the direction searched is not the gradient, but rather the conjugate gradient. Two vectors, $\mathbf{V}_1$ and $\mathbf{V}_2$ are conjugate with respect to matrix $\mathbf{A}$ if they satisfy the condition

$$\mathbf{V}_2^T \mathbf{A} \mathbf{V}_1 = 0. \tag{3.20}$$

Comparing this relation with Equation 3.19 shows the difference between the steepest descent method and the conjugate gradient method. Once a vector direction has been searched for a minimum, the next search vector is not perpendicular to the first vector, but conjugate to it. The inclusion of $\mathbf{A}$ in Equation 3.20 introduces information about the residual surface into the selection of new search vectors. For a case in which the residual surface is a distortion of the simple circular bowl shape, the conjugate gradients point to the minimum at the center. In the cases examined here, however, the matrix $\mathbf{A}$ is not known in advance, necessitating the use of an algorithm that approximates the conjugate gradient method.

The programs I wrote made use of the nonlinear conjugate gradient method, which follows the form of the conjugate gradient method, but without any prior knowledge of the residual surface. Any point can be placed into the computational method of Section 3.3 to find the associated residual, although the number of points calculated should be kept to a minimum to reduce computation time. Once a point is found, the residual of neighboring points are evaluated to determine the approximate gradient. This

must be done along each axis to fill all the components of the gradient vector. For a case with eight unknowns, for example, at least eight neighboring points must be evaluated to construct the gradient. In the steepest descent method, once a point and its gradient are found, a search is then made along that gradient for a new minimum point. In the nonlinear conjugate gradient method, the new search vector is modified by information from the previous search direction, in order to approximate Equation 3.20.

The algorithm I used to implement the conjugate gradient method is as follows:

1. For the point **P**, find the gradient vector **V**
2. Search along the line defined by $-\mathbf{V}$ for the point with the lowest residual, which becomes the new point **P**.
3. From point **P**, calculate the new gradient **VT**.
4. Rather than search in the direction **VT**, search along direction $\mathbf{V2} = \mathbf{VT} + \frac{\|\mathbf{VT}\|^2}{\|\mathbf{V}\|^2}\mathbf{V}$ for the new optimal point **P2**.
5. Set **P**=**P2** and **V**=**V2**, and repeat from step 3.

The gradient revision of step 4 is known as the Fletcher-Reeves formula [30], with other possible formulas given in the literature. If this step is skipped, the algorithm becomes the steepest descent method.

3.3.4 Example Results

As an example of an application in which this calculation technique could be used, we consider second-harmonic generation in a singly-resonant microcavity. The cavity is assumed to consist of gallium arsenide (GaAs), for which dispersion curves are available [31]. The nonlinear coefficient of GaAs is 100 pm/V, which is relatively high when compared with the second-order nonlinear coefficients of other materials [10].

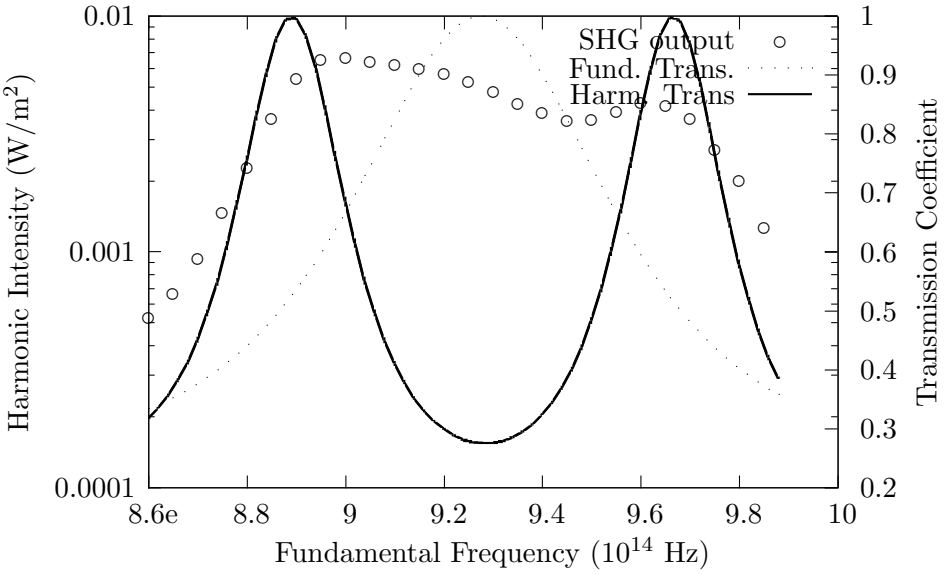

Figure 3.3: Calculated harmonic intensity for a 1.5 micrometer cavity of GaAs. The pump intensity is 10 MW/m^2.

Furthermore, GaAs has low loss due to absorption for energy with a wavelength larger than approximately 0.9 micrometers [32]. We assume first a single crystal of GaAs that has been cut at both ends to create flat ends. The refractive index of GaAs is approximately 3.3, so by Equation 3.14 the reflection coefficient is approximately 0.5. Since this reflection coefficient is low, a large improvement in conversion efficiency is not expected. Furthermore, due to dispersion, the cavity will reach resonance at different points for the fundamental and the harmonic wave. Figure 3.3 shows the SHG generated by this cavity using the calculation methods of this chapter. The cavity length was set to 1.5 micrometers, which is the coherence length for this process and this material, so phase-mismatch does not diminish the output. We see that the output roughly follows the resonance points of the fundamental and harmonic. The resonance points are not collocated, however, so the harmonic amplitude does not reach a high peak.

More SHG efficiency can be obtained from this microcavity by using engineered mirrors. As will be described in Chapter 4, multiple layers of dielectrics can be placed on

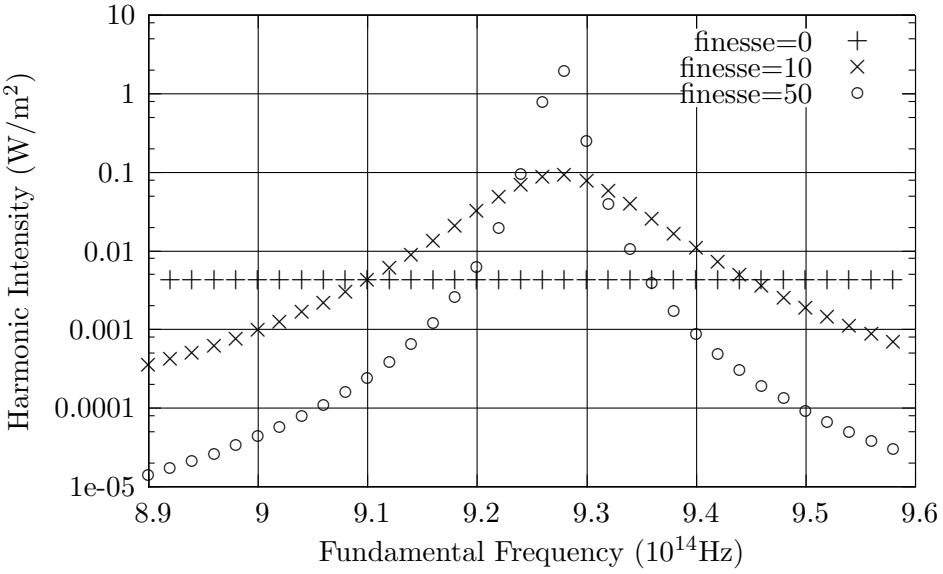

Figure 3.4: Calculated harmonic intensity for a 1.5 micrometer cavity of GaAs resonant for the pump wave, for different values of cavity finesse at the pump frequency.

a surface to form a mirror. By designing the layer thicknesses, it is possible to create a mirror that meets reflection coefficient goals at set frequencies. Figures 3.4 and 3.5 and show the results of using a singly-resonant set of mirrors with the nonlinear cavity. The mirrors are set to have a real reflection coefficient at the fundamental frequency, and no reflection at the harmonic frequency. The resonance offers a much higher SHG output than the case shown in Figure 3.3.

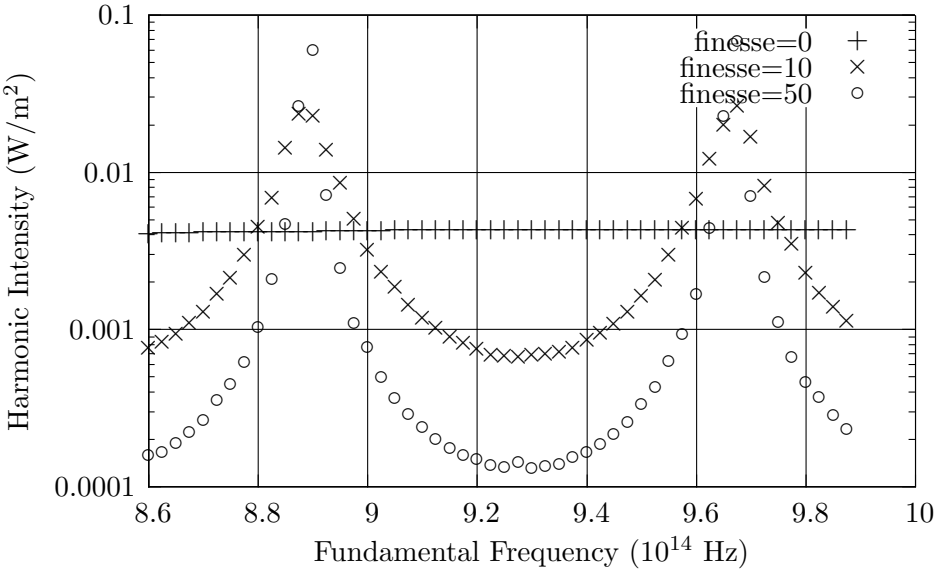

Figure 3.5: Calculated harmonic intensity for a 1.5 micrometer cavity of GaAs resonant for the harmonic wave, for different values of cavity finesse at the pump frequency.

3.3.5 Multiple Coupled Cavities

The general optimization-based analysis method can be extended to model multi-layered cavities. A three-layer cavity is shown in Figure 3.6, along with the variables that define the solution. Each boundary adds two more vectors (four complex unknowns). The center cavity, consisting of GaAs, was set to a length of 3 micrometers, which is the coherence length of this process in this material. The two outer cavities consist of $Ga_{0.6}Al_{0.4}As$, and their lengths are varied together. At the two ends are placed non-dispersive mirrors with reflection coefficients of 0.9. The pump beam has a wavelength of 2 micrometers and an intensity of 10 MW/m^2. The plot of harmonic intensity as a function of the outer cavity lengths is shown in Figure 3.7. The peaks corresponding to cavity resonances are clearly visible.

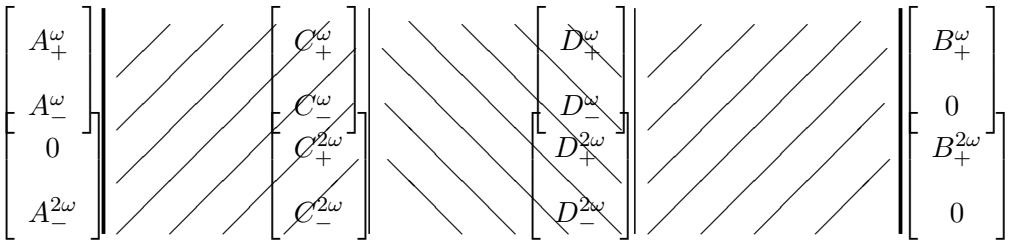

Figure 3.6: Variables in the case of second-harmonic generation in a set of three coupled cavities.

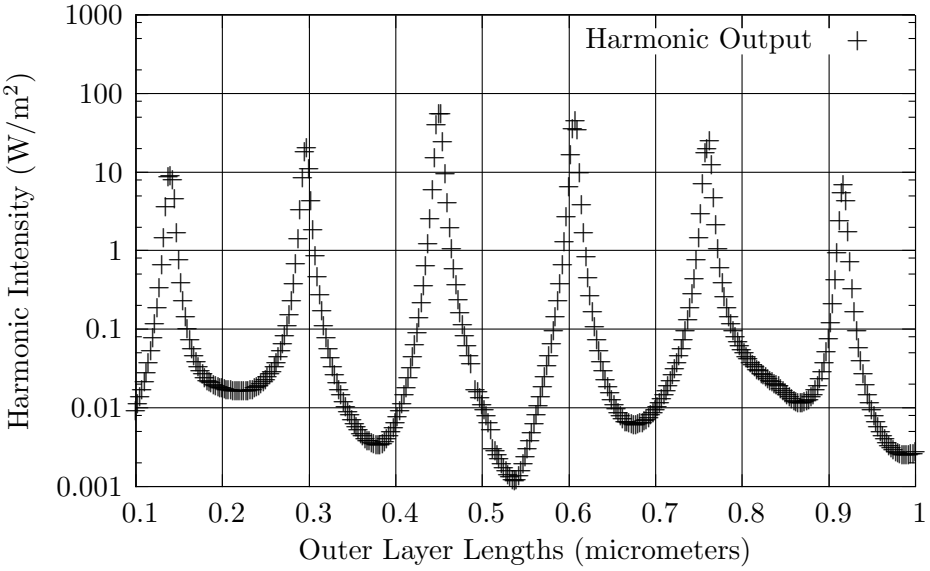

Figure 3.7: Calculated harmonic intensity for the three-cavity structure. The middle cavity length is held constant, while the two outer cavity lengths are varied together.

3.4 Summary

This chapter introduced a new technique for calculating the fields associated with nonlinear optical processes in resonant cavities. Included in the results are the output fields as well as the internal fields within the resonator. The basis of this technique is that possible field values are tested until a set of valid field amplitudes is found. The testing process can include boundary conditions, nonlinear propagation equations, loss, gain, and any other conditions that the fields must satisfy. This technique is therefore more general than previous calculation methods. Any number of frequencies and cavities can be included for solving. Furthermore, the calculation method presented here solves directly for the steady-state, so that the transient solution and the added complexity of a time-domain solver is avoided.

To demonstrate the application of this technique, the full procedure for SHG in a single dielectric cavity was described. The fields are translated across the cavity boundaries using a transfer matrix, and are propagated across the cavity using coupled differential equations. A residual error term is created from the results of the calculations, and then the fields are adjusted to lower the error. Sample calculations were presented for the sample case, although the method is capable of solving for much more complicated situations.

Another class of resonator for which the technique was demonstrated was those made up of multiple cavities. While the number of unknowns rises, the procedure is the same as for the single-cavity resonator. Each interface is represented by a transfer matrix and the propagation across each cavity is computed using coupled differential equations. The generality and versatility of this method allows it to be applied to situations in which there is no other adequate calculation technique. In Chapters 5 and 6 this method is used to draw new conclusions for certain classes of nonlinear optical resonators.

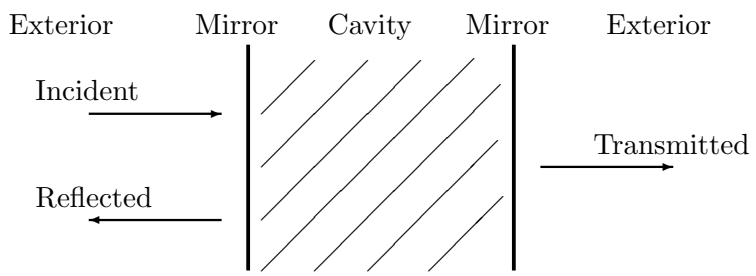

Figure 3.8: Schematic representation of a one-dimensional resonant cavity.

3.5 Acknowledgments

Portions of this chapter have been adapted from G. Klemens and Y. Fainman, "Optimization-based calculation of optical nonlinear processes in a micro-resonator", *Optics Express*, Vol. 14, No. 21, pg. 9864–9872 (2006) and G. Klemens and Y. Fainman, "Exact optimization-based analysis method applied to nonlinear processes in a multi-cavity micro-resonator", *2007 Conference on Lasers and Electro-Optics*.

3.6 Appendix: Overview of Resonant Cavity Properties

3.6.1 Definition and Operation

A one-dimensional optical resonant cavity consists of a dielectric material with mirrors placed at each end, facing each other. A schematic of such a structure is shown in Figure 3.8.

An analysis of this structure shows that resonance is achieved when the cavity length is equal to an integer multiple of half-wavelengths [33]. At resonance, the reflected waves inside the cavity are in phase and add constructively, causing the internal field strength to be higher than the incident wave. Furthermore, the reflected field is canceled through destructive interference and the transmitted field approaches the incident wave

in magnitude. Off resonance, destructive interference between the reflected internal waves causes the internal field magnitude to be less than that of the incident wave, the transmitted field magnitude approaches zero and the incident energy is all reflected. This structure, therefore, acts as a filter allowing waves of some frequencies to pass and reflecting waves of all other frequencies.

3.6.2 Quantitative Description of Resonant Cavity Performance

Several interrelated figures of merit exist describing cavity performance; the one used here is the finesse. Defined as the ratio of the distance between passbands to the width of the passbands, the finesse is given by the formula [33]

$$\mathcal{F} = \frac{\pi r}{1 - r^2}, \tag{3.21}$$

with r being the field reflection coefficient of the mirrors.

Another quantity of interest in characterizing resonant cavities is the cavity lifetime. This is defined as the time taken for the internal field magnitude to reach e^{-1} of its initial value if the incident field were shut off. We can consider the cavity lifetime to be the mean time that a photon that enters the cavity spends within it before exiting. For a cavity of length L and internal refractive index n, the cavity lifetime can be shown to be related to finesse by the formula [34]

$$t_c = \frac{nL}{\pi c}\mathcal{F}. \tag{3.22}$$

Since the time taken for a wave to cross the cavity is $\frac{nL}{c}$, Equation 3.22 shows that the finesse corresponds approximately to the number of times a photon will cross the cavity. Equivalently, the finesse is the approximate number of beams in the cavity.

A related figure of merit is the cavity Q, which is a measure of the energy loss from the cavity. The Q is defined as $\frac{\omega U}{P}$, where U is the energy stored in the cavity

and P is the rate of energy loss. For radiofrequency resonant circuits, the Q is typically in the range of 10-30, while for optical cavities, the Q can be in the thousands due to the inclusion of ω in the definition. Besides a measure of loss, the Q can also be shown to be given by $\frac{\omega_0}{\Delta\omega}$, with ω_0 a resonance frequency and $\Delta\omega$ being half the width of the passband. A high Q, therefore, indicates a small passband. For the resonant cavity the Q can be shown to be given by [34]

$$Q = \omega t_c, \tag{3.23}$$

which can be related to finesse by Equation 3.22. The longer photons stay within the cavity, indicating low loss, the more interfering beams will be in the cavity. Frequencies that are off-resonance are therefore more attenuated, while on-resonance frequencies will be increased.

3.6.3 Cavity Bandwidth

The filtering effect of the resonant cavity limits the modulation bandwidth that can pass. The maximum bitrate can be derived in two ways. In the time domain, one pulse should have left the cavity before the next pulse enters,

$$\text{bitrate} = \frac{1}{2t_c}. \tag{3.24}$$

Using the definition of t_c, the bitrate is related to the finesse by

$$\text{bitrate} = \frac{\pi c}{2nL\mathcal{F}}. \tag{3.25}$$

In the frequency domain, there must be enough bandwidth in the passband around the carrier frequency, ω, to allow the modulation,

$$\text{bitrate} = \frac{\omega}{2Q}. \tag{3.26}$$

This equation can be converted into Equation 3.25 using the definitions given earlier.

The common result of Equation 3.25 shows that a microcavity will allow for higher modulation speeds than a longer cavity. As an example, a typical laser diode is built around a cavity that is approximately one millimeter long. Assuming a refractive index of 3.2 and a finesse of 100, the maximum bitrate of Equation 3.25 is 1.4 Gbps (bits-per-second). A similar cavity that is 10 micrometers long (.01 mm), however, allows modulation up to 140 Gbps. This shows the advantage of microcavities for high-speed communications applications.

3.7 Appendix II: Pseudo-code Implementation of SHG Solver

This section presents a more detailed implementation of the SHG solver than what was outlined in Section 3.3. The programs were written in C++, using the GNU Scientific Library for many of the mathematical functions. The program is presented here in pseudo-code for readability and generality. For clarity, some lengthy portions of code have been reduced to one statement, while other portions are written out in more detail. The program becomes longer if three or more waves are involved, although the overall outline remains the same. The conjugate gradient method is used to perform the optimization. If an externally-written optimization function is used, then the MAIN function would call the optimization function to find the fields, with the RESIDUAL_CALC function supplied.

```
MAIN function:
   declare parameters:
      WAVELENGTH:  fundamental wavelength
      PIN:  input power of fundamental wave
      LENGTH:  cavity length
      INDEX_F:  refractive index at fundamental
      INDEX_H:  refractive index at harmonic
      NL:  nonlinear coefficient
      RHO_F, TAU_F:  reflection and transmission coefficients,
           fundamental, can be complex
      RHO_H, TAU_H:  reflection and transmission coefficients,
```

```
        harmonic, can be complex
   GOAL:  maximum residual at which the optimization ends

calculated parameters:
  M_F:  the interface transfer matrix from RHO_F, TAU_F
  M_H:  the interface transfer matrix from RHO_H, TAU_H
  The matrix inverses of these matrices are also assembled.

main body:
   declare FIELD: complex vector containing field magnitudes
     FIELD[1]:  incident fundamental field from left, found from
          PIN and held constant throughout the program
     FIELD[2]:  fundamental field emerging from the left boundary
          (reflected field)
     FIELD[3]:  fundamental field emerging from the right boundary
          (transmitted field)
     FIELD[4]:  harmonic field emerging from the left boundary
     FIELD[5]:  harmonic field emerging from the right boundary

 optimization loop:
         (loop until RESIDUAL < GOAL, or a set number of iterations)
     find RESIDUAL for point FIELD, function listed below
     find GRAD: complex vector that is the gradient at point FIELD,
         found with function listed below

     conjugate gradient loop:
         % the number of iteration is
         % typically approximately the dimension of FIELD, set to 1
         % iteration and comment out a few lines below to reduce to
         % the method of steepest descent
        search a line from point FIELD in the direction of GRAD for
           a new minimum residual point, update FIELD
        find new GRAD from point FIELD
        calculate GRAD=GRAD+ (|GRAD|/|previous GRAD|)^2 *
           (previous GRAD)
     end conjugate gradient loop

     find RESIDUAL for FIELD
     if (RESIDUAL = RESIDUAL before conj. grad. loop):
        adjust constants used in gradient and linesearch
        functions
         % using adjustable constants decreases run time;
         % the constants are set for a coarse search at first,
         % and then set to a finer search as needed;
         % this also keeps the program general,
         % since different case parameters are best solved with
```

```
            % different sets of function constants
    end optimization loop

    output FIELD and RESIDUAL
            % FIELD[4] and FIELD[5] are the output harmonic field
end MAIN function


RESIDUAL_CALC function:
    take in point FIELD and parameters describing cavity

    % translate field on outside of cavity into interior
    multiply vector (FIELD[1];FIELD[3]) by inverse of M_F
        -->get PUMP_LEFT_+ and PUMP_LEFT_-
    multiply vector (0;FIELD[4]) by inverse of M_H
        -->get HARM_LEFT_+ and HARM_LEFT_-
    multiply vector (FIELD[2];0) by inverse of M_F
        -->get PUMP_RIGHT_+ and PUMP_RIGHT_-
    multiply vector (FIELD[5];0) by inverse of M_H
        -->get HARM_RIGHT_+ and HARM_RIGHT_-

    use Runge-Kutta or similar solver to propagate PUMP_LEFT_+ and
        HARM_LEFT_+ from the left cavity boundary to the right cavity
        boundary; uses coupled differential equations
            -->get PUMP_L_TO_R and HARM_L_TO_R
    multiply PUMP_L_TO_R by exp(-i*2*pi*INDEX_F*LENGTH/WAVELENGTH)
    multiply HARM_L_TO_R by exp(-i*4*pi*INDEX_H*LENGTH/WAVELENGTH)
        %this assumes the envelope-form of the differential
        % equations are used,
        %so the phase shift is handled separately
    RESIDUAL=(real(PUMP_RIGHT_+)-real(PUMP_L_TO_R))^2 +
             (imag(PUMP_RIGHT_+)-imag(PUMP_L_TO_R))^2 +
             (real(HARM_RIGHT_+)-real(HARM_L_TO_R))^2 +
             (imag(HARM_RIGHT_+)-imag(HARM_L_TO_R))^2

    use solver to propagate PUMP_RIGHT_- and HARM_RIGHT_- from
         the right cavity boundary to the left cavity boundary
            -->get PUMP_R_TO_L and HARM_R_TO_L
    multiply PUMP_R_TO_K by exp(-i*2*pi*INDEX_F*LENGTH/WAVELENGTH)
    multiply HARM_R_TO_L by exp(-i*4*pi*INDEX_H*LENGTH/WAVELENGTH)
    RESIDUAL=RESIDUAL+(real(PUMP_LEFT_-)-real(PUMP_R_TO_L))^2 +
             (imag(PUMP_LEFT_-)-imag(PUMP_R_TO_L))^2 +
             (real(HARM_LEFT_-)-real(HARM_R_TO_L))^2 +
             (imag(HARM_LEFT_-)-imag(HARM_R_TO_L))^2
    return RESIDUAL
end RESIDUAL_CALC function
```

```
GRAD_CALC function:
    take in point FIELD and the corresponding RESIDUAL
    GRAD[1]=0   %input remains constant
    % simple two-point derivative
    real(GRAD[2])=(RESIDUAL_CALC(FIELD[2]+DX)-RESIDUAL)/DX
    imag(GRAD[2])=(RESIDUAL_CALC(FIELD[2]+i*DX)-RESIDUAL)/DX
    similarly find GRAD[3], GRAD[4], GRAD[5]
    return GRAD
end GRAD_CALC function


LINESEARCH function:
    take in point FIELD and direction GRAD
        % there are many possible search algorithms, a simple
        % point-by-point search is presented here
    find the residuals of equally-spaced points along the line
        of GRAD from point FIELD
        --> fill vector POINTS with the residuals
    compare each entry in FIELD with its two neighbors to find
        points with less residual than their neighbors
        --> get minima
    find the residuals of points along line GRAD around each minima,
        with close spacing between points
    get overall minimum
end LINESEARCH function
```

4

Engineered Microstructures for Nonlinear Optical Processes

4.1 Introduction

Resonant cavities have long been used to increase the efficiency of nonlinear processes, particularly second-harmonic generation (SHG) [7]. In a typical setup, the cavity is set to resonate for the fundamental wavelength, thereby raising the field strength in the nonlinear medium, or for the harmonic wavelength, which increases conversion efficiency with multiple passes through the cavity. Due to dispersion, however, a cavity that resonates at one wavelength will not resonate at a multiple wavelength. Improvements in microfabrication technology have recently allowed for the creation of photonic-crystal mirrors with engineered dispersion [35]. With these mirrors, it is possible to design cavities that resonate at multiple wavelengths, making doubly-resonant cavities possible. Several designs and analyses have been presented showing the enhancement of SHG in a crystal of gallium arsenide (GaAs) with doubly-resonant cavities [36, 37, 38], and similarly for third-harmonic generation [26]. The doubly-resonant cavity has also been

applied to the case of parametric oscillation in GaAs involving three frequencies [39], leaving one non-resonant wavelength. Parametric oscillation in three coupled cavities, with each cavity set to resonate for one of the frequencies, has been experimentally demonstrated [40]. Since the resonant cavities were not co-located, the enhancement of the nonlinear output was not maximized. Presented here is the first analysis and design of a triply-resonant cavity, and concurrently the first general examination of the design methods and conditions for nonlinear resonant cavities with designed dispersive mirrors [41]. The first part of this chapter is an explanation of the conditions that must be satisfied by a resonant cavity design, applicable to any number of waves and any type of nonlinearity (second-order, third-order, etc.). Then the design methods are applied to a nonlinear process involving three waves in a triply-resonant cavity. Finally, the chapter appendix explains the method that was used to design the dispersive mirrors.

4.2 General Analysis of Dispersive Resonant Cavities for Efficient Nonlinear Wave Mixing

The resonant cavity design methods discussed in the introduction have not made use of recent advancements in the design of dispersive dielectric mirrors with arbitrary reflection coefficients. A general configuration of such a structure is shown in Figure 4.1. Two dielectric mirrors are used to control the resonances of the cavity, allowing operation at set multiple optical frequencies. Wave mixing occurs in the nonlinear material placed between the two mirrors. For efficient nonlinear wave interaction, two conditions must be simultaneously satisfied: (i) conservation of momentum, and (ii) conservation of energy. When the nonlinear conversion is performed in a cavity, the cavity parameters must be designed so that the cavity is either transparent or resonant, since an off-resonance cavity would contain little or no energy. We consider here cavities that

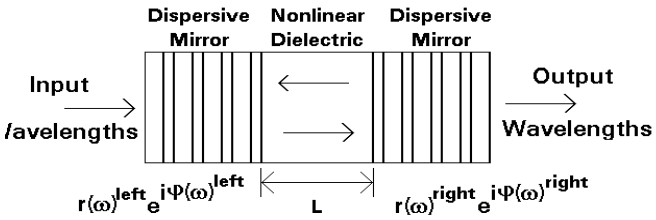

Figure 4.1: Diagram of a multiply-resonant cavity used for nonlinear wavelength conversion.

are designed to resonate at all the relevant frequencies of the nonlinear process, which adds another design condition: (iii) cavity resonance requirements.

Consider a process involving P frequencies, as discussed in Section 3.2, the differential equation describing the evolution of the complex envelope of each wave q, with $q = 1 \ldots P$, is

$$\frac{dA_q(z)}{dz} = -i\frac{\omega_q \chi_{eff}}{cn_q} \prod_{p \neq q}^{P} A_p(z) \exp\left(i\Delta k\ z\right) \exp\left(i\Delta\omega t\right), \tag{4.1}$$

where A_p are the complex envelopes, ω_q are the frequencies, χ_{eff} is the effective nonlinear coefficient, c is the speed of light, n_q are the refraction coefficients, Δk is the phase-mismatch term and $\Delta\omega$ is the frequency mismatch term. We assume nondegenerate wave mixing here, although the analysis still applies in the degenerate case with two or more waves having the same frequency. We define the phase-mismatch by

$$\Delta k = \sum_{r}^{R} k_r - \sum_{s}^{S} k_s, \tag{4.2}$$

where the first summation is made over the wavenumbers of the R input photons in the process, and the second summation is made over the wavenumbers of the S output photons, with $S + R = P$. The wavenumber at frequency ω_q in a medium of refractive index n_q is defined as $k_q = \frac{\omega_q n_q}{c}$. Some of the complex envelopes may be conjugated in Equation 4.1, depending on the specific process. We define the frequency mismatch

term as

$$\Delta\omega = \sum_{r}^{R} \omega_r - \sum_{s}^{S} \omega_s, \tag{4.3}$$

where ω_r are the frequencies of the input photons and ω_s are the frequencies of the output photons. The slowly varying envelope approximation has been applied, which assumes that the envelope functions A_q vary slowly on the scale of the optical wavelengths.

4.2.1 Energy Conservation

Conservation of energy determines the frequencies involved in the nonlinear wave mixing. The condition $\Delta\omega$=0 applies to every nonlinear process at every point in the cavity. Unlike phase-matching, this condition can not be compensated by the mirrors. All nonlinear processes always meet the condition of conservation of energy.

4.2.2 Phase Matching

Conservation of momentum is equivalent to satisfying the phase matching condition. When $\Delta k = 0$, phase match is achieved and the conversion can continue until the input beams are fully depleted. When $\Delta k \neq 0$, the photons generated along the propagation direction will cancel the output signal energy, coupling it back to the input fields. For example, in a three-wave mixing process, the output power will follow a $\sin^2(x)$ curve [6], with the distance between the point where the waves are in phase to where they are 180 degrees out-of-phase defined as the coherence length, L_c. The distance between in-phase points is two coherence lengths. The designs shown here use the phase of the reflection of the cavity mirrors to compensate for the phase-mismatch at multiple frequencies. The phase compensation condition is expressed as

$$2\Delta kL + \sum_{p}^{P} \left(\varphi_p^{(left)} + \varphi_p^{(right)}\right) = 2\pi a^{(1)}, \tag{4.4}$$

where L is the cavity length, $a^{(1)}$ is an integer, and $\varphi_p^{(left)}$ and $\varphi_p^{(right)}$ are the mirror phases at the left and right side of the cavity, respectively, at frequency p. The complex mirror reflection coefficient is

$$r(\omega) = |r(\omega)| \exp\left(i\varphi(\omega)\right). \tag{4.5}$$

When Equation 4.4 is satisfied, the reflection coefficients of the mirrors will reset the phase-mismatch between the waves to zero, thereby allowing the output wave to continue growing.

4.2.3 Cavity Resonance Condition

The cavity design must also satisfy the resonance condition at each frequency, leading to the expression

$$2k_pL - \varphi_p^{left} - \varphi_p^{right} = 2\pi a^{(2)}, \tag{4.6}$$

where $a^{(2)}$ is an integer, and p varies through all the frequencies involved. If Equation 4.6 is not satisfied for a given frequency, destructive interference will minimize the field strength in the cavity. In applications such as [7], the mirrors at some frequencies have negligible reflection coefficients to allow those fields to pass through the cavity, thereby bypassing the resonance condition. The added flexibility of dispersive dielectric mirrors can be used to satisfy the resonance condition at all the frequencies involved in the nonlinear wave mixing process. Equation 4.6 applied to each frequency, along with Equation 4.4 can be solved to find values for the mirror reflection phases.

For efficient nonlinear wave mixing processes in a dispersive resonant cavity, these three conditions must be satisfied simultaneously. The following examines the degrees of freedom in the design parameters of dispersive resonant cavities to meet these conditions and to optimize the output efficiency.

4.3 Parameters in the Design of Dispersive Resonant Cavities

There are two degrees of freedom available in the design of dispersive resonant cavities for nonlinear wave mixing: (i) cavity length, and (ii) amplitude and phase of the mirror reflection coefficients. The mirror reflection coefficients are used to set the resonance condition, determining the cavity finesse at each frequency. The cavity length can be optimized to satisfy the phase matching condition and maximize output power. The importance of these parameters, as well as their optimal values, can be determined by considering Equation 4.1.

The cavity length significantly affects the output signal efficiency, and any length beyond the optimal value either has no effect or decreases conversion efficiency, depending on the exact length used. A solution of coupled-wave equations based on Equation 4.1 shows that the power in the signal beam follows a $\sin^2(x)$ relation as the beams propagate through a crystal [6], with the zero points two coherence lengths apart. A pulse at the output wavelength passes approximately $\mathcal{F}$ times through the cavity, leading to an approximation for output power of the form

$$P_{out} = C\mathcal{F}\sin^2\left(\frac{\pi}{2L_c}L\right), \tag{4.7}$$

where L_c is the coherence length and C is a constant dependent on the nonlinear coefficient of the cavity dielectric, the input field magnitudes within the cavity, and the transmission of the mirrors. From this equation we deduce that a cavity length of two coherence lengths will yield no output power, since the converted power will have all reverted back to the input waves. Furthermore, Equation 4.7 is periodic, so any cavity length beyond two coherence lengths is redundant. The maximum output power occurs when $L = L_c$. For SHG, this is the point at which the fundamental and the harmonic

fields are 180 degrees apart in phase, and the direction of net energy flow is about to switch from upconversion to downconversion [11].

4.4 Case Study: Downconversion in a Triply-Resonant GaAs Dispersive Resonant Cavity

As an example, this section presents a Dispersive Resonant Cavity (DRC) for efficient wavelength conversion in GaAs. The pump, signal and idler frequencies corresponding to wavelengths of 1.55, 3.8 and 2.617 micrometers (μm), respectively, are used. The refractive indices at these frequencies are 3.3989, 3.3263 and 3.3427, respectively [31]. The pump wavelength of 1.55 micrometers is widely available as a laser source, and the idler wavelength of 2.617 micrometers can be provided by some variable sources. The signal wavelength of 3.8 micrometers, however, is not commonly available in laser sources.

The conclusions of Section 4.3 can be numerically demonstrated for the example case. One design parameter available for optimization is cavity length. Unlike the domain inversions of Quasi-Phase Matching (QPM), which can only produce a phase shift of 180 degrees, the mirrors of a DRC can be designed to produce a wide range of phase shifts. Cavities of arbitrary lengths can therefore be used. Upon consideration of the physical mechanisms of wavelength conversion along with the effects of the resonant cavity, conclusions can be drawn concerning optimal cavity length. As described in Section 4.2, the intensity of the generated signal wave follows a $\sin^2(x)$ curve, with the distance from a zero to a maximum being the coherence length. Upon reaching a maximum, the signal intensity returns to zero after another coherence length. Any cavity length beyond a coherence length is therefore not useful. For cavity lengths smaller than the coherence length there is no reconversion depleting the signal beam.

The conversion approaches the phase matched case as the cavity becomes smaller (i.e., $\sin(x)$ approaches x); however, the effective cavity length of $\mathcal{F}L$ approaches zero, leading to less conversion. For a cavity length that is very small with respect to the coherence length, the rate of nonlinear conversion would be high, but the finesse must also be high in order to have enough effective interaction length for efficient conversion. The estimated conversion efficiency as a function of cavity length for the example case is shown in Figure 4.2. The optimal cavity length is at $L = L_c$, which is similar to quasi-phase matching. This conclusion applies independently of the cavity finesses. The DRC has advantages, however, over QPM. While the signal beam reflecting within the cavity is similar to propagation across multiple poled domains, the beams are all collocated in one domain which increases the field magnitude, further increasing conversion efficiency. Furthermore, since only one cavity length must be fabricated for the DRC, the tolerances involved in creating dozens or hundreds of adjacent inverted domains is avoided.

The advantage of designing a multiply-resonant structure is shown in Figure 4.3. The output conversion efficiency as a function of input power is shown for cases of singly, doubly and triply resonant structures. Each additional resonance increases the efficiency by approximately an order of magnitude, demonstrating the advantage of a multiply-resonant structure over a structure without resonances at each relevant frequency.

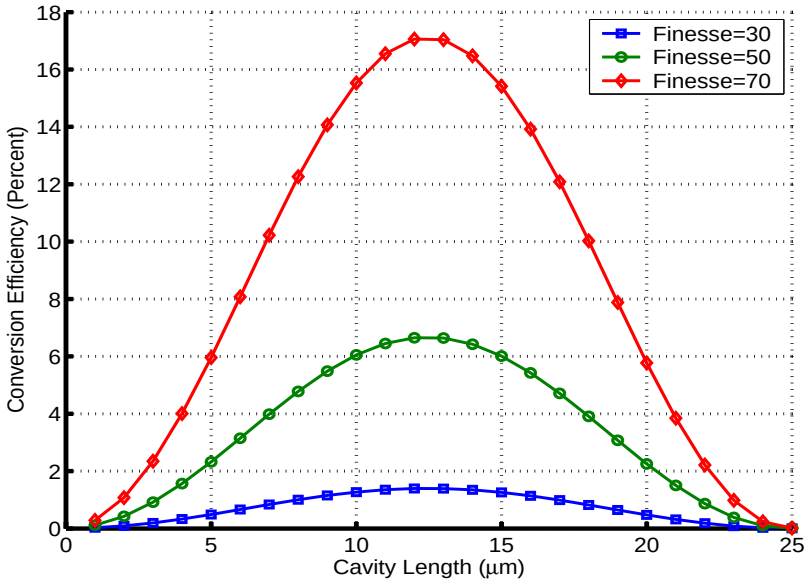

Figure 4.2: The calculated conversion efficiency as a function of cavity length for a dispersive resonant cavity for the three-wave process. The cavity finesse is held constant at 30, 50 and 70, and the input field intensities are 0.5 $W/\mu m^2$.

4.5 Design Parameters: Asymmetric Mirrors

The examples to this point have assumed the same mirrors on both sides of the cavity, but different mirrors can be used. This section examines the effects of asymmetric mirrors using the simple example of SHG in a resonant cavity from Section 3.3.4. The analysis will show that using symmetric mirrors generally yields the highest output. First the linear behavior of an asymmetric resonator is explained, and then its effects on nonlinear processes are demonstrated.

4.5.1 Analysis of Asymmetric Linear Resonators

The transmission and reflection characteristics of a resonant cavity with only linear response can be derived by summing the reflected waves. This technique could not be used in the nonlinear case since the effects of the many waves could not be separated. For dielectric exhibiting only linear effects, however, the reflected waves

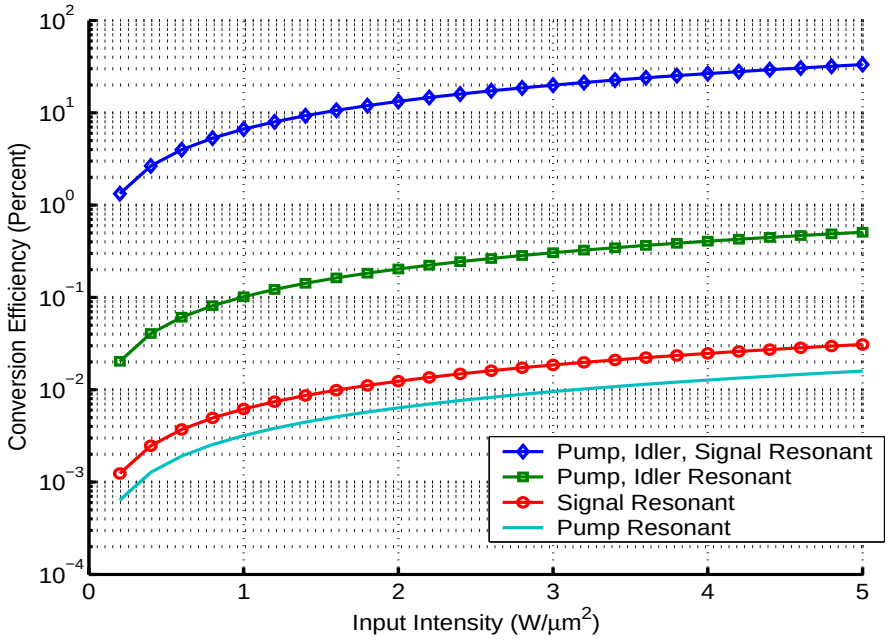

Figure 4.3: The calculated conversion efficiency as a function of input power for the three-wave process. Ideal phase compensating mirrors were assumed, and the cavity length was held constant at 12 μm. Shown are curves for cases where (i) the pump, (ii) the signal, (iii) the pump and idler, and (iv) the pump, idler, and the signal are resonant. For the resonant beams, the finesse was set to 50, and was set to 0 for the non-resonant beams.

within the cavity can be calculated independently of each other and then summed to find the total fields. For this analysis method, a single dielectric of length L and index n is assumed. The phase change in propagating a wave of wavelength λ across the cavity is therefore $\phi = \frac{2\pi n}{\lambda} L$. On the left of the dielectric is a mirror with reflection and transmission coefficients of r_1 and t_1, and on the right is a mirror with coefficients r_2 and t_2.

The analysis begins by assuming a wave of amplitude 1.0 approaching the cavity from the left. There is a reflected wave of magnitude $-r_1$ and a transmitted wave of magnitude t_1. The wave transmitted into the cavity propagates across to the right mirror, at which the amplitude is $t_1 e^{-i\phi}$. Some of this amplitude, $t_1 t_2 e^{-i\phi}$, is transmitted across the right mirror and some, $t_1 r_2 e^{-i\phi}$, is reflected back. The reflected wave crosses the the cavity from right to left where some is transmitted across the left mirror and some is reflected. This procedure extends indefinitely to produce an infinite series of waves. The summation of the waves emerging from the left mirror is the reflection of the cavity, r, and the summation of waves transmitted across the right mirror is the cavity transmission, t. These series are

$$r = -r_1 + t_1^2 r_2 e^{-i2\phi} \sum_{n=0}^{\infty} r_1^n e^{-i2\phi n}, \tag{4.8}$$

$$t = t_1 t_2 e^{-i\phi} \sum_{n=0}^{\infty} r_1^n r_2^n e^{-i2\phi n}. \tag{4.9}$$

These series can be seen to converge by applying convergence tests. For example, the ratio test states that a series will converge if $\lim_{n\to\infty} \left| \frac{a_{n+1}}{a_n} \right| < 1$, with a_n being the terms of the series. By this test the series of Equations 4.8 and 4.9 are convergent since both r_1 and r_2 are less than one and this analysis assumes no gain. The two series sum to

$$r = -r_1 + \frac{t_1^2 r_2 e^{-i2\phi}}{1 - r_1 r_2 e^{-i2\phi}}, \tag{4.10}$$

$$t = \frac{t_1 t_2 e^{-i\phi}}{1 - r_1 r_2 e^{-i2\phi}}. \tag{4.11}$$

If the phase advance in propagating across the cavity is a multiple of π, meaning the cavity length is a multiple of half-wavelengths, resonance is reached and the relations become

$$r = -r_1 + \frac{t_1^2 r_2}{1 - r_1 r_2}, \tag{4.12}$$

$$t = \pm \frac{t_1 t_2}{1 - r_1 r_2}. \tag{4.13}$$

For the case of symmetric mirrors, $r_2 = r_1$ and $t_2 = t_1$, we can use the relation $t_1^2 = 1 - r_1^2$ to find that $r = 0$ and $t = \pm 1$. When the mirrors are asymmetric, however, the transmission at resonance will be less than 1.0. In this linear analysis, the order of the mirrors does not affect the results. Placing the higher-reflectivity at the left or the right will give the same overall reflection and transmission coefficients. The field strength within the cavity is different for the two cases, but has no effect in a linear analysis. The internal field strength has a significant influence on nonlinear processes, as is shown in the following section.

4.5.2 Nonlinear Processes in an Asymmetric Resonant Cavity

The lack of a general, accurate analytical method of calculating nonlinear effects in a resonant cavity necessitated the creation of the computational method of Chapter 3; therefore, simple representative example cases will be calculated here and general conclusions drawn from the results. The example used is SHG in a singly resonant cavity as presented in Section 3.3.4. The cavity consists of a 1.5 micrometer length of GaAs and mirrors that are reflective for a wavelength of 2.0 micrometers and have low reflection coefficients for wavelengths around the harmonic at 1.0 micrometers.

Figure 4.4 plots calculated SHG output as a function of fundamental frequency for different values of left and right mirror reflectivities. Included are points for the symmetric cases of both mirrors set to r=0.97 (cavity finesse of 50) and r=0.90 (cavity

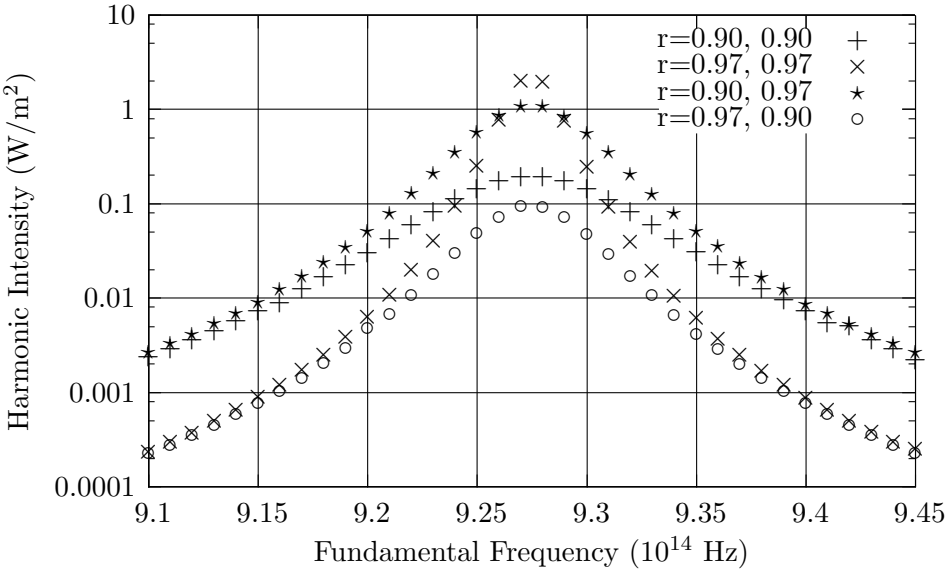

Figure 4.4: SHG output of a singly-resonant cavity with different values of left and right mirror reflection coefficients.

finesse of 15). The plots show that for high SHG output at the resonance point, the higher-reflection mirror should be placed on the right side, opposite to the incoming beam. Since the optimization-based calculation method yields the full field solution, we can examine the fields inside and around the cavity.

The electric field amplitudes of the fundamental frequency wave for the asymmetric cases are shown in Figure 4.5. While the reflected and transmitted field on either side of the cavity are the same for the two cases, the internal fields vary significantly. Placing the higher reflectivity mirror in the left position creates a lower internal field. In a symmetric cavity the reflected beam is canceled by backward-propagating waves. When the first mirror has higher reflection, however, the amplitude of the reflected beam is too high to be fully compensated, leading to a nonzero reflection from the cavity at resonance. The reflected beam that is left after cancelation does not enter the cavity and does not contribute to the internal fields. When the second mirror, on the right of the cavity, has higher reflectivity, the surplus reflected waves are within the cavity.

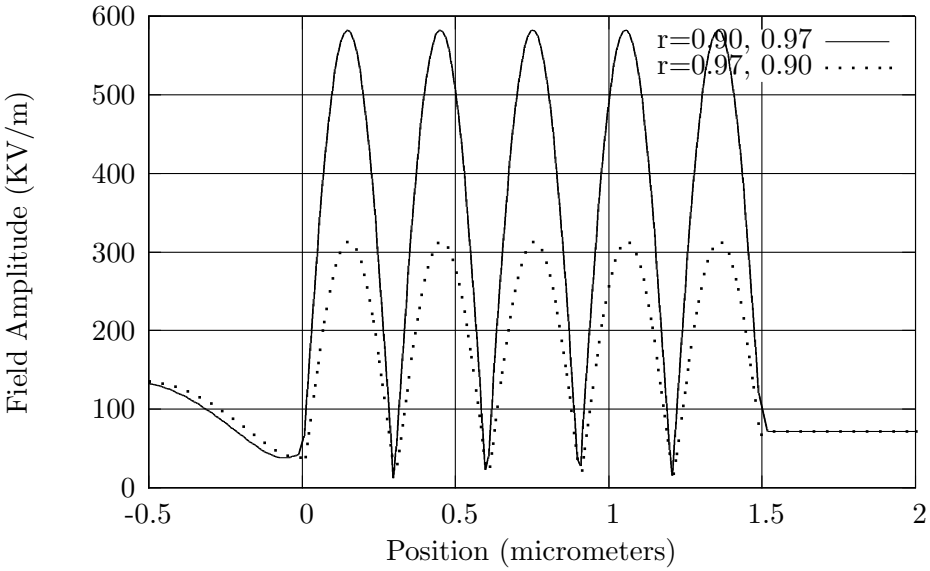

Figure 4.5: Calculated field at the fundamental frequency for the asymmetric mirror cases.

For nonlinear processes in asymmetric resonant cavities, therefore, the lower reflectivity mirrors should be placed early in the structure to allow the incoming beam to enter the cavity.

4.5.3 Half-Cavity with Mirror

Another useful configuration makes use of a broadband mirror with total reflection. This configuration for SHG in a single cavity is shown in Figure 4.6. This is an asymmetric mirror configuration with the high-reflectivity mirror placed at the far end of the incoming beam. Unlike the previous cases, the nonlinear output is only found in the reflected beam, since there is no transmitted beam. The internal field is also expected to reach higher values than the case of two partially-reflective mirrors, which can be understood by considering the cavity lifetime. With a high-reflectivity mirror on one side of the cavity, half of the cavity loss is eliminated (loss due to nonlinear conversion or other mechanisms is not considered in this approximate analysis). The cavity lifetime,

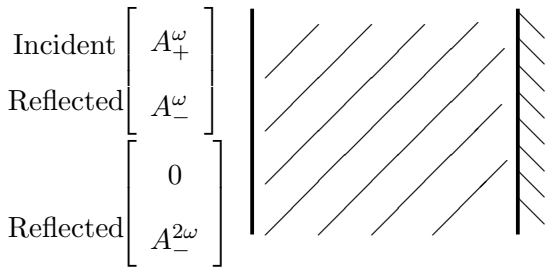

Figure 4.6: A resonant cavity with a broadband, high-reflectivity mirror on one side.

the time after which a group of photons that had entered the cavity takes to reach e^{-1} of their original number, is approximately doubled. With a higher cavity lifetime, the fields within the cavity are also higher, increasing the nonlinear effect.

The implementation of the optimization-based analysis method for this type of structure can follow two separate tracks. In one, the variables as shown in Figure 4.6 are used. The fields to the left of the cavity are translated across the interface into the cavity, and then propagated to the mirror using coupled differential equations. The fields are then reflected at the mirror and then propagated back to the left mirror. At the left side of the cavity the starting values must match the ending values, or else an error residual can be calculated. The second implementation is to use the all the variables on the left and right side of the cavity, as shown in Figure 3.2. The reflection coefficient for the mirror on the right is then set to a high value, such as $r = 0.999$, for both the fundamental and the harmonic frequencies.

Plots of converted SHG output are shown in Figure 4.7 for the asymmetric case with a broadband mirror placed on one side of the cavity. The SHG output is significantly raised by the inclusion of the high-reflectivity mirror. The internal fields are predicted to be higher for the asymmetric case, which is confirmed by the field plots in Figure 4.8. Overall, this configuration offers higher nonlinear conversion and has the

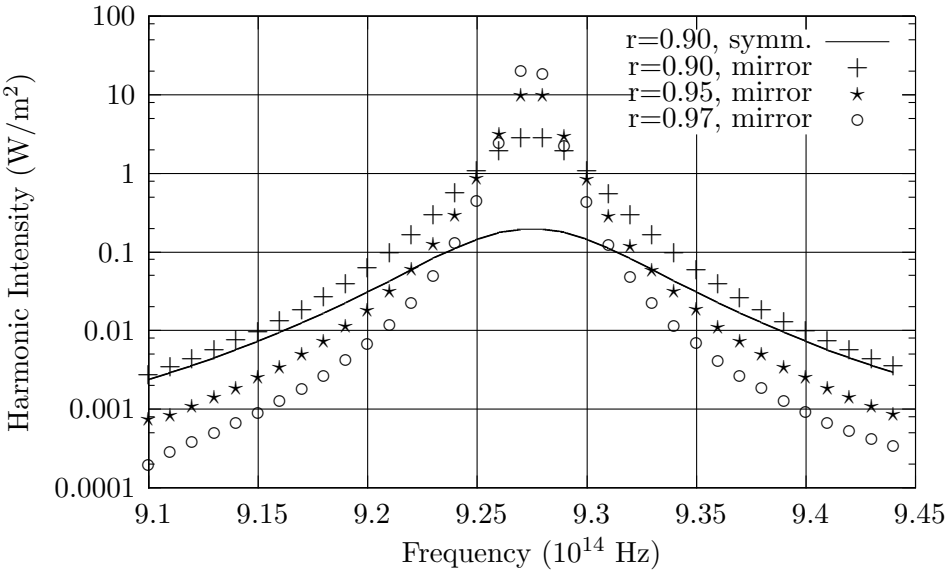

Figure 4.7: SHG output from a resonant cavity with a broadband, high-reflectivity mirror on one side.

benefit of only requiring one engineered mirror. A drawback is that the nonlinear output must be separated from the input beam, which can add loss.

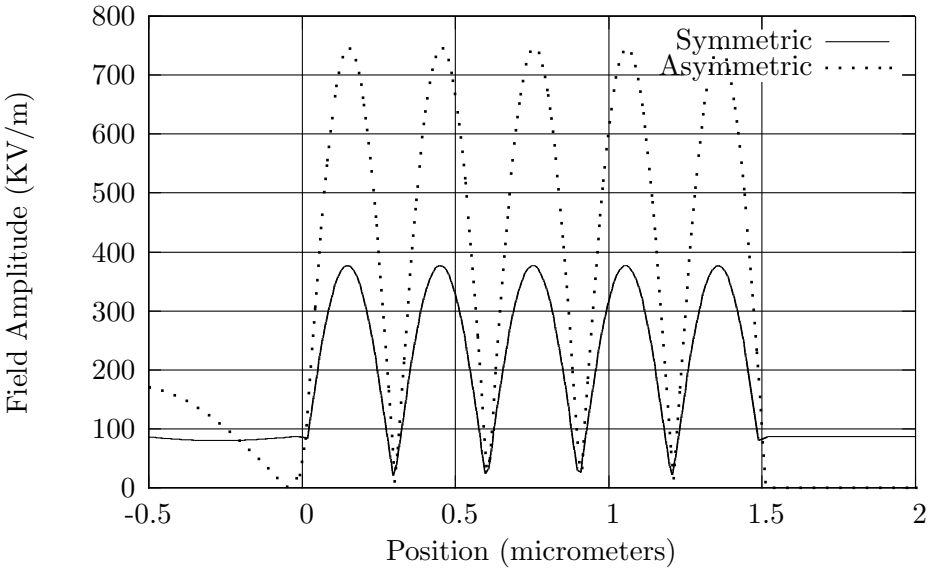

Figure 4.8: Field magnitudes at the fundamental frequency for the cases of symmetric mirrors with r=0.9 and asymmetric mirrors, r=0.9 and r=1.0.

4.6 Summary

This chapter examined the conditions that must be met in the design of efficient nonlinear optical resonant structures. These conditions derive from basic laws such as conservation of energy and conservation of momentum, as well as the resonance effect in the structure. These conditions translate into equations concerning cavity parameters such as cavity length and mirror reflection coefficients, as well as material dispersion. The designer must satisfy all of the equations and the application goals. There will, in general, be a range of design parameters that satisfy the required conditions. The choice of specific values is then made to maximize the efficiency of the nonlinear effect.

Example cases were used to determine the effect of design parameters on the efficiency. If the mirror reflection coefficients can be arbitrarily designed, then any cavity length can be used. The examples show, however, that the optimal cavity length is one coherence length. At this length there is no net back-conversion taking place within

the structure. The magnitude of the mirror reflection coefficients should be as high as possible, as expected, to increase the positive feedback effects at resonance. For processes involving more than one frequency, approximately one order of magnitude increase in the output power can be achieved with each frequency that resonates.

Asymmetric mirrors were also examined through the use of numerical examples. Using mirrors with different reflection coefficient magnitudes was found to generally yield lower efficiency than the symmetric-mirror case. In approximate terms, the asymmetric-mirror cavity can be conceptualized as a symmetric cavity with an extra reflection placed at one end. The extra reflection degrades the interference effects of resonance. For example, the reflected field is not completely canceled at resonance. Placing the higher-reflection mirror first in the cavity is a poor design choice, because the energy is reflected before it can enter the cavity. In the specific case where the last mirror is a broadband, completely-reflecting mirror, the efficiency can be as high or higher than the symmetric case. In that case, however, the output is reflected back in the direction of the input and must be separated.

4.7 Appendix: Circuit-Simulator Design of Dispersive Mirror Structure

4.7.1 Dispersive Mirrors for Cavity Resonance

The example structure of Section 4.4 requires a mirror that has the correct reflection phase angles at 1.55, 2.617 and 3.8 micrometers; this appendix describes a design method for mirrors meeting these types of requirements. The transmission through the example structure, when designed mirrors are used, is shown in Figure 4.9. The mirrors are made up of GaAs and AlAs in alternating layers, with layer thicknesses given by Figure 4.10. In the following, the circuit simulator-based method that was used to find

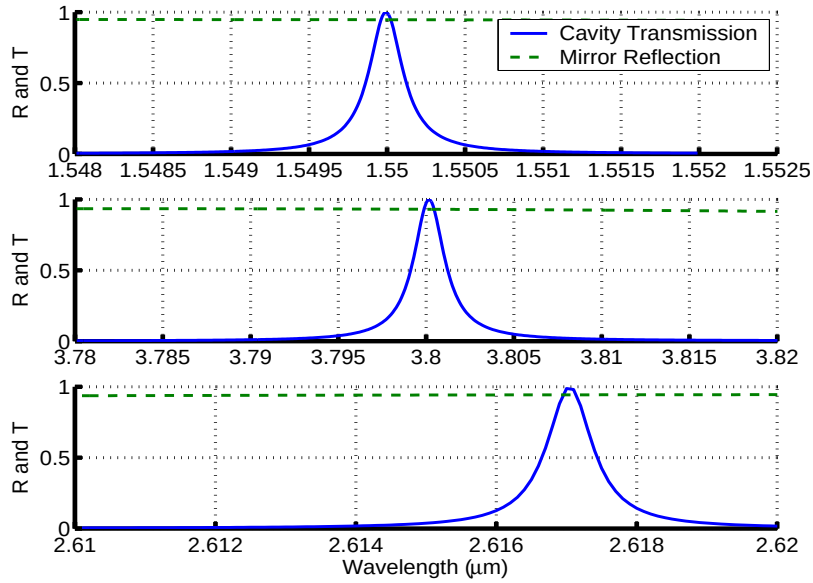

Figure 4.9: Reflection and transmission of the example structure of Section 4.4 using stacks of dielectric layers as mirrors. Shown is the transmission through the entire structure, and reflection from inside the cavity looking outward.

the layer thicknesses of Figure 4.10 is explained.

4.7.2 Transmission Line Representation of Multi-Layered Dielectrics

In order to analyze the optical transmission and reflection from a multi-layer structure, the structure and the waves must first be represented in circuit terms. An analogy exists between plane-wave propagation through dielectric layers and electrical propagation through sections of transmission line. The equations describing the two cases are identical, if the correct translation of parameters is made. The wave propagation constant is the same for both cases, and can be related to the operating wavelength, λ, or the frequency, ω, by

$$k = \frac{2\pi n}{\lambda} = \frac{\omega n}{c}. \tag{4.14}$$

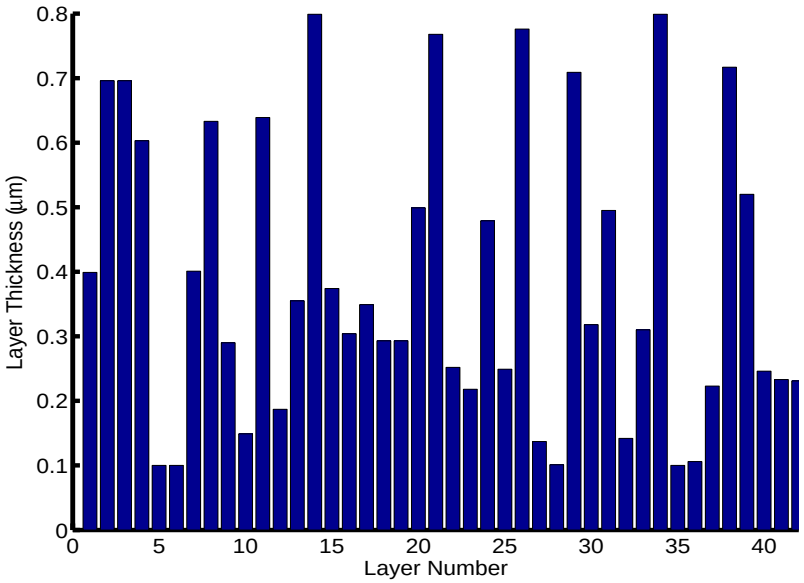

Figure 4.10: Layer thicknesses for a dielectric stack to produce the transmission and reflection response of Figure 4.9. The layers are alternating between GaAs and AlAs.

This term directly translates from the dielectric case to the transmission line case. The other term describing the media is the characteristic impedance given by

$$Z = \frac{Z_0}{n}. \tag{4.15}$$

For a propagating electromagnetic wave, Z_0 is the ratio of electric field to magnetic field at each point. It has units of resistance and takes the value in a vacuum of approximately 376.76 Ohms. There is more latitude to pick the value of Z_0 in the transmission line case. Traditionally, microwave circuits are based on a characteristic impedance of 50 Ohms, although a more convenient value such as 1 Ohm can be used. For both the transmission line and the dielectric layer case, any value of Z_0 used will yield the same reflection and transmission results as long as the value is used consistently. Material dispersion can be included by specifying the index n as a function of frequency.

The most direct simulation method to use for this application is an S-parameter analysis. In this simulation, ports are placed on the circuit and electrical waves are

sent from each port. The waves arriving at each port from every other port are then normalized to the port impedance and assembled into the S-parameter matrix. For a two-port system, S_{11}, the wave measured coming out of port one due to a wave being sent into port one is the reflection coefficient, and S_{21}, the measured wave at port two from a stimulus at port one, is the transmission coefficient.

The setups for analyzing resonant cavities in a circuit simulator are shown in Figures 4.11 and 4.12. The setup of Figure 4.11 is to find the reflection from within the cavity looking out through the mirror. A resistor of value Z_0 Ohms represents the space outside the cavity. Each transmission line segment is characterized by material parameters Z, the characteristic impedance, and k, the propagation constant. A circuit analysis for transmission is diagrammed in Figure 4.12. The cavity, represented by a transmission line, is also included in this case. The goal of the design is to find transmission line lengths that would yield a high reflection coefficient for the first setup and a high transmission coefficient for the second setup at the relevant frequencies. By setting the transmission line lengths to be variables, and by creating goals based on the reflection and transmission parameters, the circuit simulator's design optimization routines can be used to find an adequate set of segment lengths. This method was used to find the mirror design with the transmission and reflection responses shown in Figure 4.9.

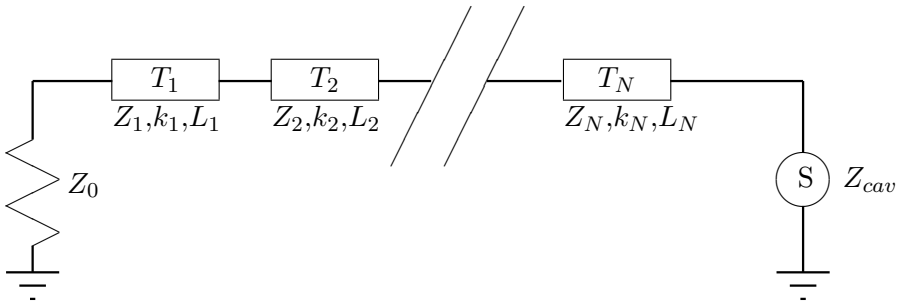

Figure 4.11: Setup in a circuit simulator for determining the reflection from inside the cavity looking into the mirror.

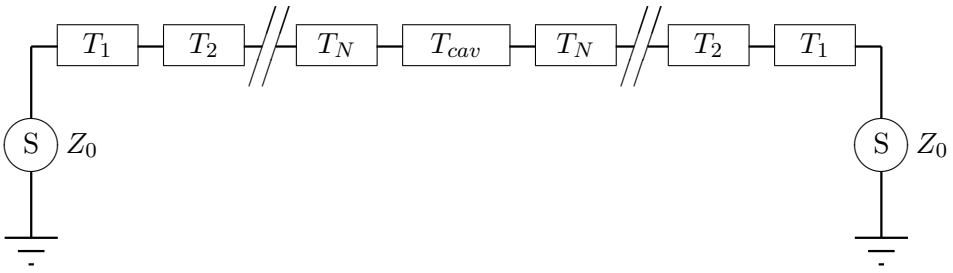

Figure 4.12: Setup in a circuit simulator for determining the transmission through a resonant cavity with a layered dielectric mirror.

5

Intensity-Dependent Nonlinear Effects in Resonant Microstructures

5.1 Introduction

Multi-stable resonant cavities have potential uses as optical limiters, all-optical switches, and in optical computing [42], and have therefore been studied in various ways. The basic principle of operation is that the field intensity within the cavity determines its transmission parameters. If the incident field is switched off or significantly lowered, the field intensity within the cavity will remain high for approximately the cavity lifetime, creating memory. A bistable optical cavity was first demonstrated in 1969, consisting of a 2 centimeter long resonator filled with SF_6 gas [43]. The gas is highly absorptive, unless driven to saturation with a high field intensity, thereby providing a response that varies with the input intensity. Resonators based on semiconductors, such as gallium arsenide (GaAs) and indium antimonide (InSb), have also been examined [44]. These

devices achieve their bistability through the Kerr effect, where the internal intensity of the cavity adjusts the refractive index, and therefore changes the resonance condition. Coupled resonators using Kerr nonlinearities have also been proposed to perform all-optical signal processing functions, such as optical phase shifting and switching [45, 46].

Analysis methods used to calculate the performance of bistable optical structures have made use of various approximations and are not generally applicable to every case. An early method is to assume a static resonator, and introduce the Kerr nonlinearity as a shift in the transmission curve [47]. Another method is to solve the differential wave equations in the cavity, using either an approximate analytic solution [48], or computationally [49]. These methods are limited in their applicability since they assume one homogeneous cavity. Coupled cavities, or a single cavity made up of multiple layers of materials would be difficult to solve, calling for approximate methods [45].

This chapter presents an optimization-based analysis of multistable optical resonators. The approach used is similar in principle to that of Chapter 3. For a given structure, the boundary conditions, resonance conditions, nonlinear effects, loss and gain, and other relevant effects are represented by equations. A set of field values is assumed and then tested by placing those values into the equations. The results are evaluated by physical considerations. For example, the field value incident from one side of the cavity, when translated through the cavity, should be equal to the assumed field value exiting the cavity on the other side. If the set of assumed field values does not produce a self-consistent solution, then an error term can be defined, and the set of values adjusted to lower the error. This method avoids a direct solution of the equations describing the structure, which can become prohibitively complex for structures with many features or if numerous effects are included.

The next section explains the use of this method for a one-dimensional resonant structure with Kerr nonlinearity. Explicit equations are given for a simple loss-less case,

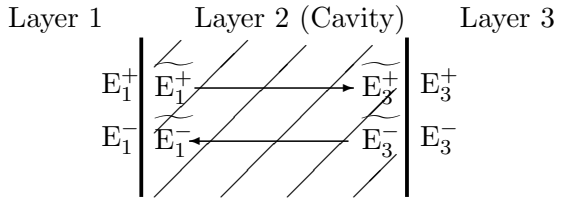

Figure 5.1: Solution method for a single cavity. External fields are translated to internal cavity values. After propagation, $\widetilde{E_1^+}$ and $\widetilde{E_3^-}$ should match $\widetilde{E_3^+}$ and $\widetilde{E_1^-}$, respectively.

and direction is provided for the inclusion of more effects such as loss, gain, or multi-frequency operation. The following section presents examples of this technique in use on semiconductor cavities. The first example is a single cavity that could be used as an optical limiter or as a bistable device. The second example is a device consisting of two adjacent cavities and three mirrors, meant to demonstrate the flexibility of this method.

5.2 Analysis Method

The analysis method for intensity-dependent effects is similar in outline to the method presented in Chapter 3. The case of a single cavity, as outlined in Figure 5.1, is defined by the complex variables representing the incident wave, E_1^+, the reflected wave, E_1^-, the transmitted wave, E_3^+, and any wave incident from the right, E_3^-. In a typical situation, E_1^+ is known and E_3^- is uniformly set to zero, leaving E_1^- and E_3^+ to be found. Considering these two quantities to be complex, there are four unknowns to be found.

5.2.1 Fields at the Cavity Boundaries

The external fields can be translated across the cavity boundaries by matrix multiplication. The fields on either side of the left cavity boundary, for example, are

related by

$$\begin{pmatrix} E_1^+ \\ E_1^- \end{pmatrix} = \frac{1}{\tau} \begin{pmatrix} 1 & \rho \\ \rho & 1 \end{pmatrix} \begin{pmatrix} \widetilde{E_1^+} \\ \widetilde{E_1^-} \end{pmatrix}, \tag{5.1}$$

where ρ and τ represent the reflection and transmission coefficients of the boundary, respectively. These coefficients can be made complex-valued to represent phase-shifting reflective structures. For a mirror made up of multiple layers, the field propagation across each layer can be represented by relations such as Equation 5.1. Through matrix multiplication, the matrices of the multiple layers can be condensed into one overall transition matrix.

5.2.2 Nonlinear propagation equation

The internal fields are then propagated across the cavity using nonlinear differential equations. Including the third-order nonlinear polarization in Maxwell's equations yields the differential equations to use [6]. The dynamic Maxwell's equations for electric and magnetic fields at one frequency are

$$\nabla \times E = -i\omega\mu H, \tag{5.2}$$

$$\nabla \times H = i\omega D. \tag{5.3}$$

The nonlinearity originates in the electric displacement, D. Including the third-order nonlinear constant $\chi^{(3)}$, the displacement is related to the electric field by

$$D = \epsilon_0 \epsilon_r E + \epsilon_0 \chi^{(3)} EEE. \tag{5.4}$$

Taking the curl of Equation 5.2, and substituting Equations 5.3 and 5.4 where appropriate produces a wave equation. For the case of one-dimensional propagation in the z-direction the equation is

$$\frac{d^2E}{dz^2} = -\frac{\omega^2}{c^2}\left(n^2 + \chi^{(3)}\left|E\right|^2\right)E, \tag{5.5}$$

where E is the complex field amplitude, ω is the frequency, c is the vacuum speed of light, n is the medium refractive index and $\chi^{(3)}$ is the medium nonlinear coefficient. The nonlinear coefficient is commonly given in units of m^2/W, although in Equation 5.5 it is in units of m^2/V^2.

Terms can also be included in Equation 5.5 to account for loss or gain in the cavity. If multiple frequencies are present, the nonlinear interaction between them can be characterized by a set of coupled differential equations, as was done in the frequency conversion examples in Chapter 3. Unless the frequencies are phase-matched, however, the coupled energy will be small. The second-order differential equation can also be simplified by using the slowly varying envelope approximation. The electric field is described as a constant amplitude plane wave with an envelope modulation multiplier,

$$E(z) = A(z)e^{-ikz}, \tag{5.6}$$

where $k = \frac{\omega n}{c}$. Using this definition in Equation 5.5, and assuming the envelope function $A(z)$ varies slowly on the optical wavelength scale, some small terms can be discarded. This yields a first-order differential equation,

$$\frac{dA}{dz} = -i\frac{\omega\chi^{(3)}}{2cn}\left|A\right|^2 A. \tag{5.7}$$

The solution of Equation 5.7 requires less computation than Equation 5.5; however, more simplification is possible in many cases. If loss, gain, and frequency conversion are not included, then the differential equations are unnecessary. For each of the two waves in the cavity, one going left and one going right, the magnitude $|E|$ remains constant. The propagation calculation only involves advancing the phase of E by

$$\Delta\phi = -\frac{\omega}{c}\sqrt{n^2 + \chi^{(3)}\left|E\right|^2}\Delta z, \tag{5.8}$$

with Δz being the incremental change in distance. The term $\sqrt{n^2 + \chi^{(3)}\left|E\right|^2}$ is the effective index of the medium, including the intensity-dependent Kerr effect. Note that

the term $|E|^2$ in Equations 5.5 and 5.8 is for the total field at point z, including left-traveling and right-traveling waves, as well as waves at other frequencies. While the magnitude of each of the two counter-propagating waves remain constant, their sum does not. Equation 5.8 therefore must be evaluated point-by-point across the cavity.

5.3 Demonstrations

5.3.1 Single Cavity

To demonstrate the use of this method to show bistability, consider a single cavity of semiconductor material. Assume a 200 micrometer cavity of gallium arsenide (GaAs) and an operating wavelength of 2 micrometers. The nonlinear coefficient of GaAs is approximately $10^{-13}\mathrm{m}^2/W$. A higher coefficient can be obtained by operating near the GaAs bandgap-edge at a wavelength of approximately 885 nm, although at the expense of increased loss in the cavity [44]. The end mirrors are given a reflection coefficient of 0.95, and the cavity length is adjusted to be slightly less than that of resonance. The transmission coefficient and the transmitted intensity are shown in Figure 5.2. By increasing the internal fields of the cavity, the Kerr effect puts the cavity into resonance. Further increasing the incident intensity moves the cavity beyond the resonance point. This produces the binary output plot of the transmitted intensity, with a low-transmission setting for incident intensity of 0 to 0.25 MW/m^2, and a high-transmission setting for incident intensity greater than approximately 0.3 MW/m^2. If the cavity length were set to be at resonance by default, then increasing the incident intensity would move the cavity off of resonance and lower the transmission, creating an optical limiter.

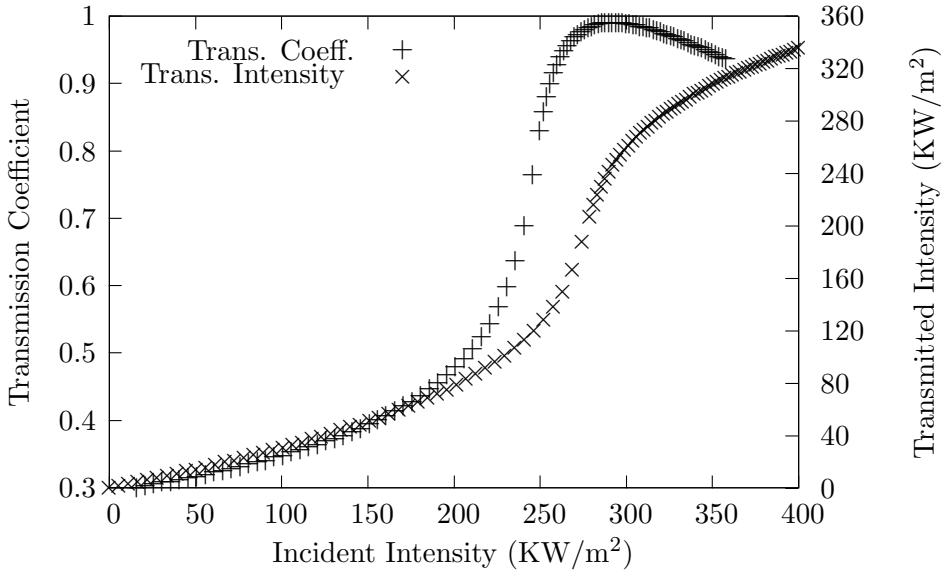

Figure 5.2: Calculated transmission intensity and transmission coefficient as a function of incident intensity. A single cavity of GaAs is assumed, with operation at 2 micrometers and end mirrors with reflection coefficients set to 0.95.

5.3.2 Bistability and Hysteresis Loops

Besides the variation of transmission dependent on input intensity discussed in the previous section, the cavities under consideration here are also able to show bistable behavior. This occurs when two possible field distributions exist that satisfy the boundary conditions, propagation equations, and any other enforced requirements. The cavity will remain in the state until a strong enough perturbation causes it to switch states.

In the optimization-based method utilized here, bistability is evident in the existence of two error residual minima. The minimum that is found is generally the one that is closest to the starting point. When bistability is expected, a search can be conducted for the minima by varying the starting point. Once the minima have been found, they can be used as the starting points to find the new minima for a slightly different input power. In this manner transmission curves can be created. The plots of transmission coefficient and transmitted intensity from Figure 5.2 are recreated in

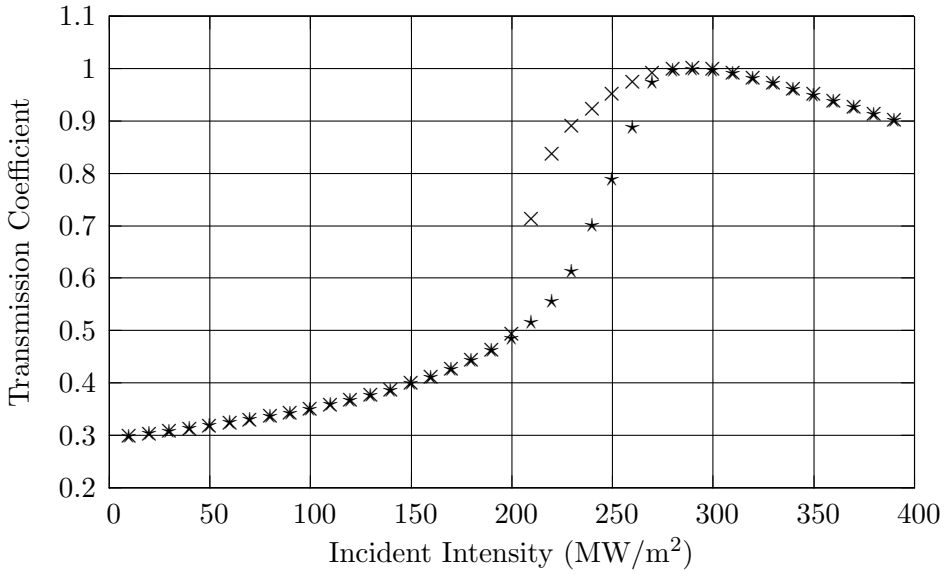

Figure 5.3: Calculated transmission coefficient as a function of incident intensity for a single cavity, with hysteresis loop included.

Figures 5.3 and 5.4, with the full bistability shown. The hysteresis loops are evident in both figures.

5.3.3 Design Parameters

The primary parameters available for the design of a bistable resonant structure are the cavity length and the cavity finesse. The effect of varying these parameters is to move the transmission curve inflection point to a lower or higher input power. From Equation 5.8, a long cavity length is expected to produce a greater index shift for a given applied intensity. The transmission curves corresponding to different cavity lengths are shown in Figure 5.5. A long cavity of GaAs allows for the use of lower input intensities to exhibit the transmission variation. Thick GaAs dies can be difficult to obtain, however, since typical wafers fabricated for electronics are 200 to 500 micrometers thick [5]. The wafers can be polished down to lesser thicknesses accurately, but thicker wafers would require custom fabrication. Also, cavities that are relatively long will not have a high

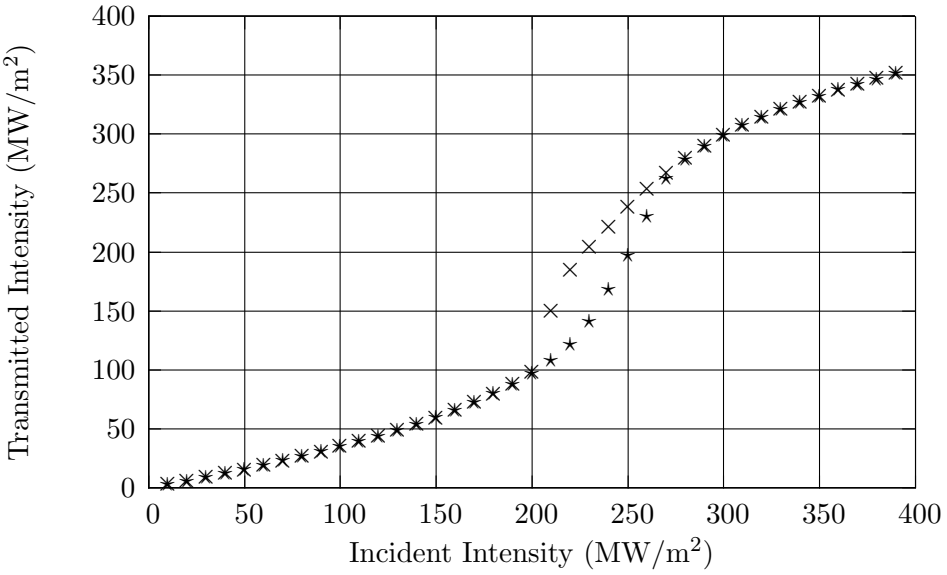

Figure 5.4: Calculated transmitted field as a function of incident intensity, showing hysteresis loop.

bandwidth for modulation, as described in Section 3.6. Transmitting data requires that a signal leave the cavity before the next signal enters. For example, by Equation 3.25 we can estimate that the maximum bandwidth of a 10 mm long cavity of GaAs with a finesse of 30 is approximately 130 Mbps (bits per second).

An alternative to increasing the cavity length is to increase the cavity finesse. A high finesse, with the high mirror reflectivities, corresponds to a long cavity lifetime, as signals that enter the cavity reflect between the mirrors before exiting. A short cavity with high finesse is therefore equivalent to a long cavity length. The fabrication difficulties in creating a long cavity are avoided, but the bandwidth restrictions still apply. The high finesse cavity, however, also has increased internal field intensity, which lowers the required input intensity. Due to the higher internal intensity, the effective length is not required to be as large as a long, low-finesse cavity to meet a particular input intensity requirement. Plots of transmission coefficient as a function of input intensity for different cavity finesse values are shown in Figure 5.6. The cavity in this case is only 10

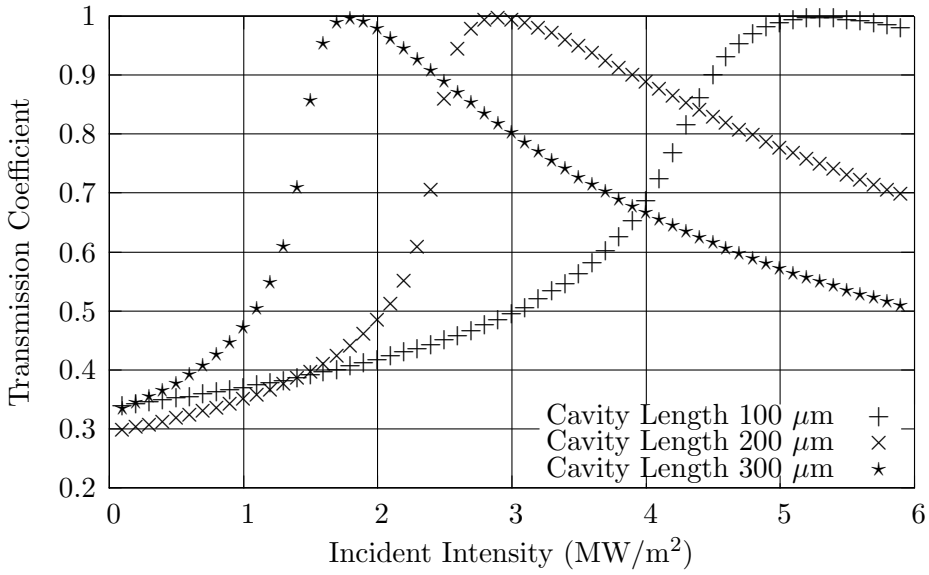

Figure 5.5: Calculated transmission intensity and transmission coefficient as a function of incident intensity for different cavity lengths.

micrometers long. For high cavity finesse, the transmission inflection point is less than that of the low-finesse case. Additionally, in the high finesse case, the internal fields are suppressed more strongly when off-resonance than in the low-finesse case, resulting in a steep transmission curve. A relatively short cavity with highly-reflective mirrors is therefore promising for creating cavities that clearly show intensity-dependent operation.

The flexibility of the solution method employed here allows us to also examine the effects of asymmetry in the mirrors. Up to this point we have assumed the two mirrors, one on each end of the cavity, to be identical. An interesting question is which mirror is most important in determining the cavity nonlinear response. A plot of transmission coefficient as a function of input intensity for two asymmetric cavities is shown in Figure 5.7. In one trace, the left mirror has a higher reflection coefficient than the right mirror, and in the other trace the reflection coefficients are exchanged. A reflection coefficient of 0.95 was used for the low value and 0.975 was used for the high value. In both cases the internal fields are unbalanced; the waves traveling in one direction have

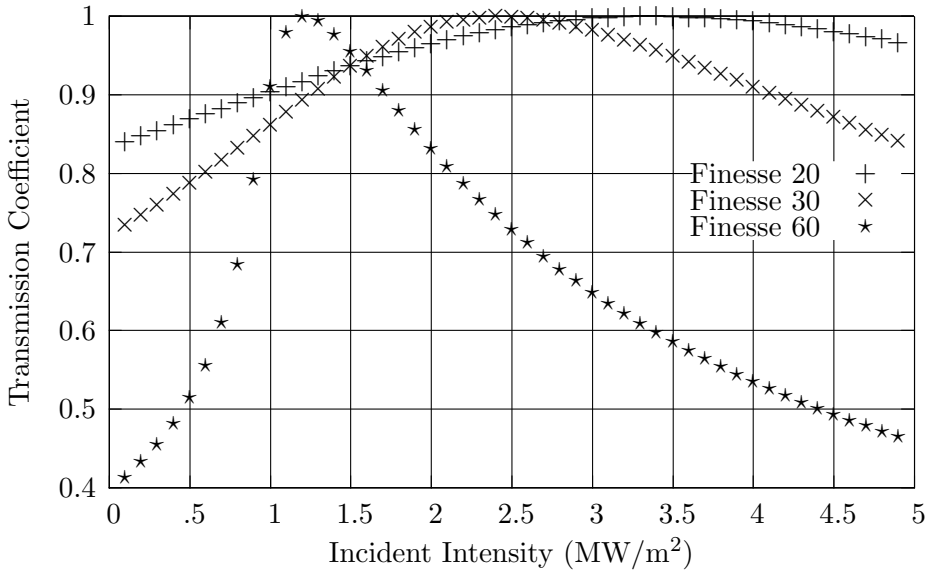

Figure 5.6: Transmission coefficient as a function of input intensity for varying finesses in a 10 micrometer cavity.

higher magnitudes than the waves traveling in the other direction. At resonance, the reflected field is therefore not completely canceled, and the transmission does not reach 1.0. Between the two cases, placing the high-reflectance mirror on the far side of the cavity from the input beam yields the strongest cavity response. This is because placing a high-reflectivity mirror on the input side would reflect much of the input beam before it can enter the cavity. Another way of framing the asymmetric case is to consider the cavity to be a combination of a symmetric resonator with both mirror reflectivities set to 0.95, and an added mirror placed on one side.

5.3.4 Multiple Cavities

A second example that further shows the flexibility of this method is the dual cavity shown in Figure 5.8. Including the cavity defined by the two outermost mirrors, there are three interacting cavities. The third interface adds two more complex variables over that of Figure 5.1, although the solution method is the same. For the example,

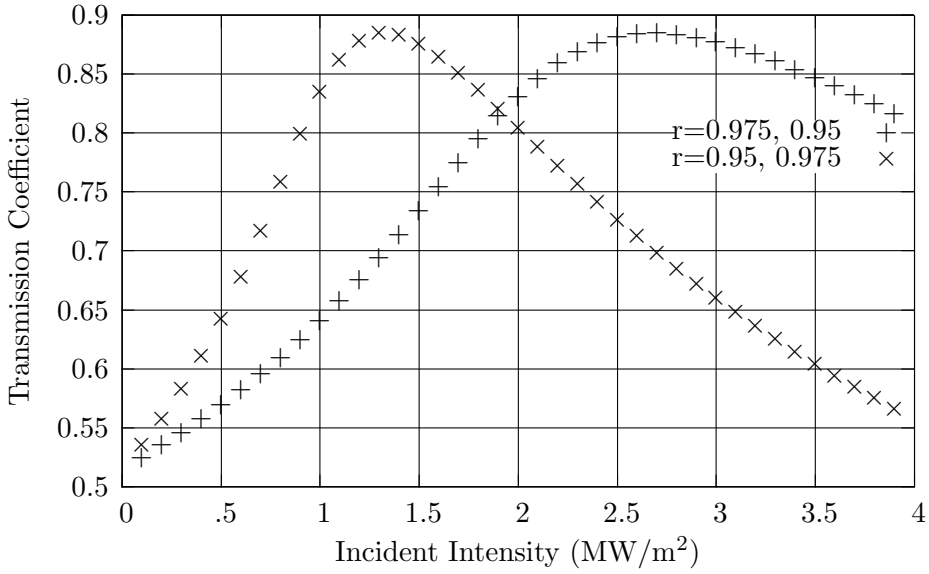

Figure 5.7: Transmission coefficient as a function of input intensity for asymmetric mirrors in a 10 micrometer cavity

two cavities of GaAs with a length of 400 micrometers was used. The mirror reflection coefficients from left to right are 0.5, 0.6, and 0.5. As in the previous example, the wavelength of operation is 2 micrometers. The calculated transmission coefficient as a function of incident intensity is shown in Figure 5.9 for a range of intensities.

The solution method also allows us to examine the fields internal to the structure. Figure 5.10 plots the electric field strength as a function of position for three input

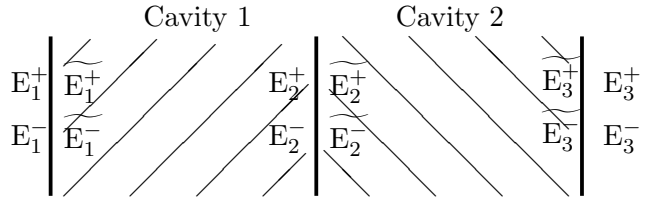

Figure 5.8: Two cavity configuration defined by complex variables E_1^+, E_1^-, E_2^+, E_2^-, E_3^+ and E_3^-. A self-consistent set will yield matching results when propagating across the cavities right-to-left or left-to-right.

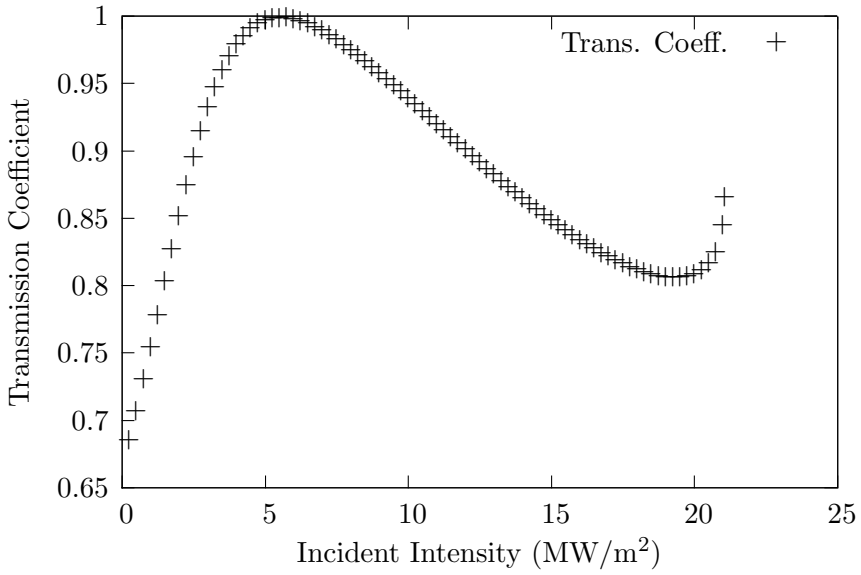

Figure 5.9: Calculated transmission coefficient as a function of incident intensity for the multi-cavity configuration of Figure 5.8. The cavities are each 400 micrometers long, and the reflection coefficients of the mirrors are 0.5, 0.6 and 0.5, from left to right.

power intensities. The internal fields form hundreds of waves within the cavity, so only the field envelopes are plotted for clarity. For low power levels the first cavity is closer to resonance than the second cavity, and for high power levels the situation is reversed. We see that at 5.5 MW/m^2 the total structure is in resonance, including both cavities.

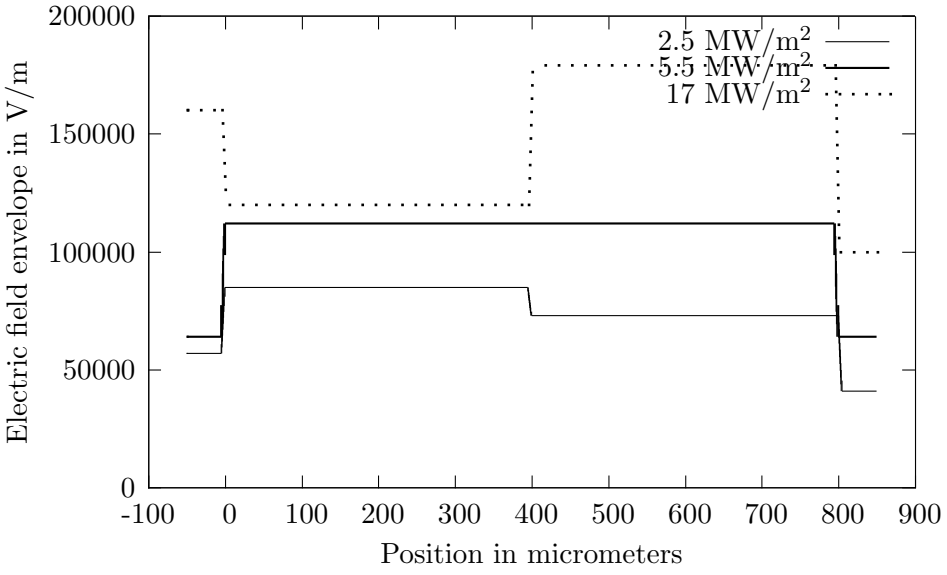

Figure 5.10: Electric field envelope for the structure of Figure 5.9 for three representative input power intensities.

5.4 Summary

This chapter has demonstrated an optimization-based method for the calculation of the optical response of cavities with Kerr nonlinearity. The basis of this method is that field values are assumed at each interface, and then calculations are made to determine if that set of values is self-consistent. If the field values are not self-consistent, the error residual can be minimized using optimization algorithms. This method has more flexibility and is more generally applicable than previously used calculation methods. In this chapter, the use of this technique for a single cavity that could be used as a bistable device or as an optical limiter was demonstrated. Unlike plots in the literature, which are based on approximate methods, every point in the transmission plots shown corresponds to a complete solution of all the relevant equations. Bistability and hysteresis curves can be constructed by searching for multiple field values that satisfy the conditions. This calculation method can also be applied to more complex cases, such

as coupled cavities, or cavities with asymmetric mirrors. This technique offers a way to analyze resonator-based optical nonlinear systems with a level of accuracy that is better than currently-used approximate methods.

6

Modulation Instability in Resonant Structures

6.1 Introduction

Wave packets propagating through a nonlinear, dispersive medium can, under the right conditions, lose energy to nearby frequencies. This effect, called Modulation Instability (MI), has been theoretically analyzed [50] and experimentally observed [51, 52] for the case of light propagating through fibers. Due to the dispersion in a medium, waves at different frequencies travel at different speeds, thereby limiting the coupling of energy between the waves (the phase-mismatch effect). In a Kerr medium, the local refractive index is affected by the intensity of the light passing through it. If the dispersion, the nonlinear Kerr constant, and the amplitude of the propagating wave meet certain conditions, then the nonlinear effect compensates for the dispersion. Efficient frequency conversion can then occur, creating MI.

The analysis of MI has followed two tracks, and both have been applicable only to propagation in an unlimited fiber length. The first analysis method is an analytical

technique in which approximations are applied to the nonlinear wave equation, producing an expression in the form of a nonlinear Shrödinger equation. Substituting a continuous wave function with a small perturbation into the equation, it can be shown that there is gain in the perturbation at frequencies around the that of the main wave. The second analysis method uses coupled differential equations to represent the energy transfer between the waves of different frequencies [53, 54]. This method forms the basis of the optimization-based technique presented here and is further elucidated in the following section. Neither of these analysis methods are applicable in the case of a resonant cavity. In such a cavity, reflections can produce many waves traveling in each direction. All of the waves, including their amplitudes and relative phases, must be taken into account in the calculation of the nonlinear effects, which complicates the problem. Alternatively, a time domain technique, such as the Finite-Difference Time Domain (FDTD) method, could be used, although with its own complicating factors. The index dispersion becomes a convolution in the time domain, and nonlinear effects become second and third order convolutions. Furthermore, obtaining high frequency resolution requires a long run time. For a high-finesse cavity, the run time will also be long due to the presence of transients which must dissipate before the steady-state solution is reached.

The procedure used here assumes the steady-state has been reached, and tests input and output field values to find a set that satisfies all boundary conditions and nonlinear equations. Balance is reached when the field values at the left of the cavity, when applied to the boundary conditions and the nonlinear equations, produce the field values on the right of the cavity, and similarly for propagation from right to left in the cavity. If the set of field values does not balance, then an error term can be defined and the set adjusted to lower the error.

The following section explains the use of this method for a one-dimensional resonant structure. This includes stating the equations involved and showing how vary-

ing levels of approximation can be used in the calculations. The subsequent section demonstrates the use of this technique with numerical examples.

6.2 Mathematical Origin of Modulation Instability

6.2.1 Analysis Based on Nonlinear Propagation

This section offers an outline of the derivation of MI that is commonly offered in the literature and in nonlinear optics texts. Some insight into MI can be gained by using this method, although the solution method presented in this chapter for MI in resonant cavities follows another track. As described in Section 6.3, that method will use a differential equation approach to MI.

As a starting point, consider the definition of wave number with intensity-dependent nonlinearity included:

$$k = \frac{\omega n}{c} = \frac{\omega}{c}\left(n_0 + d|E|^2\right). \tag{6.1}$$

Expanding k for small variations from a central value of k_0 yields

$$k - k_0 = \frac{\partial k}{\partial \omega}(\omega - \omega_0) + \frac{1}{2}\frac{\partial^2 k}{\partial \omega^2}(\omega - \omega_0)^2 + k_0 d|E|^2, \tag{6.2}$$

where the variation in frequency from ω_0 is expanded to include the second-order derivative. For a wave based on the function $\exp\left[i\left(\omega - \omega_0\right)t - i\left(k - k_0\right)z\right]$, the derivative in t is seen to correspond to multiplication by $i(\omega - \omega_0)$ and the derivative in z corresponds to multiplication by $-i(k - k_0)$. Substituting the derivative operators into Equation 6.2 gives the operator equation

$$-i\frac{\partial}{\partial z} = i\frac{\partial k}{\partial \omega}\frac{\partial}{\partial t} - \frac{1}{2}\frac{\partial^2 k}{\partial \omega^2}\frac{\partial^2}{\partial t^2} + k_0 d|E|^2. \tag{6.3}$$

Applying this operator to an amplitude function $A(z,t)$ yields

$$i\left(\frac{\partial A}{\partial z} + \frac{\partial k}{\partial \omega}\frac{\partial A}{\partial t}\right) - \frac{1}{2}\frac{\partial^2 k}{\partial \omega^2}\frac{\partial^2 A}{\partial t^2} + k_0 d|A|^2 A = 0 \tag{6.4}$$

In the absence of group velocity dispersion ($\frac{\partial^2 k}{\partial \omega^2} = 0$)and a nonlinearity ($d = 0$), only the first parenthetical term of Equation 6.4 remains, and the solution will take the form of $A\left(x - v_g t\right)$. The group velocity, v_g, is seen to be $\frac{\partial \omega}{\partial k}$. We can also see that for certain values of group velocity dispersion and nonlinearity, the second and third terms of Equation 6.4 will be equal and opposite in sign. For such cases, the two effect compensate for each other and waves will be able to propagate without distortion.

The MI literature commonly rewrites Equation 6.4 in group velocity coordinates, which simplifies solving for MI gain. Substituting $\tau = t - \frac{1}{v_g} z$ into Equation 6.4 and using $\frac{\partial z}{\partial t} = v_g$,

$$\frac{\partial A}{\partial z} - i\frac{1}{2}k_0'' \frac{\partial^2 A}{\partial \tau^2} - ik_0 d|A|^2 A = 0. \tag{6.5}$$

This equation describes the evolution of a pulse envelope moving at the group velocity, from the perspective of moving with the pulse. If the signal is a single continuous wave, rather than a pulse, the envelope remains constant in the group velocity time coordinates, so the second term of Equation 6.5 is zero. In other words, if the wave is monochromatic, the dispersion has no effect. The solution for this case is then

$$A(z) = A_0 \exp\left(ik_0 d A_0^2 z\right). \tag{6.6}$$

The complex exponential indicates self-modulation caused by the varying intensity of the wave in a material with an intensity-dependent refractive index. To find the MI effect, assume a constant envelope carrier like the above and a small amplitude perturbation, $a(z, \tau)$:

$$A(z, \tau) = \left(A_0 + a\right) e^{\left(ik_0 d A_0^2 z\right)}. \tag{6.7}$$

Substituting Equation 6.7 into Equation 6.5 gives

$$\frac{\partial a}{\partial z} = i\frac{1}{2}k_0'' \frac{\partial^2 a}{\partial \tau^2} - ik_0 d|A_0|^2(a + a^*), \tag{6.8}$$

where it is assumed that $A_0 >> a$, so that higher powers of a could be removed. This equation determines the evolution of the perturbation. Since we are interested in perturbations that take the form of waves, we give $a(z,\tau)$ the form

$$a(z,\tau) = m_1 e^{i(Kz-\Omega\tau)} + m_2 e^{-i(Kz+\Omega\tau)}. \tag{6.9}$$

When K is real, Equation 6.9 represents forward and backward traveling waves, while when it is imaginary, it represents growing and attenuating signals. The appearance of MI depends on the growth of noise signals, so we look for the conditions that cause K to be imaginary. Using Equation 6.9 in Equation 6.8, produces the system of equations

$$\begin{pmatrix} K + \frac{1}{2}k_0''\Omega^2 + k_0 d|A_0|^2 & k_0 d|A_0|^2 \\ k_0 d|A_0|^2 & -K + \frac{1}{2}k_0''\Omega^2 + k_0 d|A_0|^2 \end{pmatrix} \begin{pmatrix} m_1 \\ m_2 \end{pmatrix} = \begin{pmatrix} 0 \\ 0 \end{pmatrix}. \tag{6.10}$$

Other than the case of $m_1 = m_2 = 0$, the only way to satisfy Equation 6.10 is to find values that cause the matrix to be singular. Setting the determinant to zero, the condition on K is

$$K = \pm\frac{1}{2}|k_0''|\Omega\sqrt{\Omega^2 + \frac{4k_0 d|A_0|^2}{k_0''}}. \tag{6.11}$$

For K to be imaginary, the group velocity dispersion, k_0'', must be negative and $\frac{4k_0 d|A_0|^2}{k_0''} > \Omega^2$. From this condition we see that as the main signal field amplitude, $|A_0|$, rises, the frequency at which MI gain appears can also be higher.

6.2.2 Analysis Based on Coupled Differential Equations

The starting point of the analysis is to represent Maxwell's equations with the third-order nonlinearity in the form of coupled differential equations [6]. For a plane wave traveling along the z-axis, the wave equation for the electric field is

$$\frac{\partial^2 E}{\partial z^2} = \frac{\partial^2}{\partial t^2}\left[\varepsilon_0 n^2 E + \varepsilon_0 d E E E\right], \tag{6.12}$$

where ε_0 is the permittivity of free space, n is the (frequency-dependent) refractive index, and d is the third-order nonlinear coefficient. We consider here a wave at frequency

ω_0, which we call the pump beam, and two equally-spaced side-band frequencies of $\omega_+ = \omega_0 + \Omega$ and $\omega_- = \omega_0 - \Omega$. Accordingly, the electric field in Equation 6.12 is expanded as $E = E_0 e^{-i\omega_0 t} + E_+ e^{-i\omega_+ t} + E_- e^{-i\omega_- t} + c.c.$, with $c.c.$ denoting complex conjugate. Including this definition, and grouping frequency terms, gives three coupled differential equations:

$$\begin{aligned}\frac{d^2E_0}{dz^2} = -\frac{3\omega_0^2}{c^2}[n_0^2 E_0 + d\left(|E_0|^2 + 2|E_+|^2 + 2|E_-|^2\right)E_0 \\ +2dE_+E_-E_0^*],\end{aligned} \tag{6.13}$$

$$\begin{aligned}\frac{d^2E_+}{dz^2} = -\frac{3\omega_+^2}{c^2}[n_+^2 E_+ + d\left(2|E_0|^2 + |E_+|^2 + 2|E_-|^2\right)E_+ \\ +dE_0E_0E_-^*],\end{aligned} \tag{6.14}$$

$$\begin{aligned}\frac{d^2E_-}{dz^2} = -\frac{3\omega_-^2}{c^2}[n_-^2 E_- + d\left(2|E_0|^2 + 2|E_+|^2 + |E_-|^2\right)E_- \\ +dE_0E_0E_+^*].\end{aligned} \tag{6.15}$$

If needed, terms can be included to account for propagation loss. These equations are sufficient for solving using a numerical method such as Runge-Kutta. For most applications, however, they can be simplified, and the solution reached more quickly and efficiently, by using an envelope representation for the fields. For example, E_0 is represented as a constant plane wave and a varying envelope as $E_0 = A_0(z)e^{-ik_0 z}$, with k_0 the wavenumber at ω_0. Using the slowly-varying envelope approximation to discard second-order derivatives, Equations 6.13-6.15 then simplify to

$$\begin{aligned}\frac{dA_0}{dz} = -i\frac{3\omega_0 d}{2cn_0}[\left(|A_0|^2 + 2|A_+|^2 + 2|A_-|^2\right)A_0 + \\ 2A_+A_-A_0^*e^{i\Delta z}],\end{aligned} \tag{6.16}$$

$$\begin{aligned}\frac{dA_+}{dz} = -i\frac{3\omega_0 d}{2cn_+}[\left(2|A_0|^2 + |A_+|^2 + 2|A_-|^2\right)A_+ \\ +A_0A_0A_-^*e^{-i\Delta z}],\end{aligned} \tag{6.17}$$

$$\begin{aligned}\frac{dA_-}{dz} = -i\frac{3\omega_0 d}{2cn_-}[\left(2|A_0|^2 + 2|A_+|^2 + |A_-|^2\right)A_- \\ +A_0A_0A_+^*e^{-i\Delta z}],\end{aligned} \tag{6.18}$$

with c being the free-space speed of light and $\Delta = 2k_0 - k_+ - k_-$. In a case containing both forward and backward traveling waves there will be six equations. Due to the inherent phase mismatch between counter-propagating waves, the three forward-traveling equations can be decoupled from the three backward-traveling equations. The parenthetic intensity terms in Equations 6.13-6.15 or 6.16-6.18 apply to the total field intensity including forward and backward waves.

Solving these equations numerically will show MI for a propagation length without a cavity. The calculation is done for a set of three frequencies, ω_0, $\omega_0 + \Omega$ and $\omega_0 - \Omega$. By sweeping Ω from a small value to several terahertz we can characterize the MI gain sidebands. A small initial value of A_+ and A_- is needed for all cases to show MI output. Without a nonzero initial value for the sideband amplitudes, there are no signals to experience gain. Physically, these small initial values are noise that exists inherently in the medium or are provided by the signal source.

The emergence of MI gain from these differential equations can be found with an approximate analysis. The procedure followed here is similar to that used in [6] to approximately analyze second harmonic generation. Whereas the case in the cited literature involved two coupled equations, a pump and a harmonic, MI uses three coupled equations. The overall analysis method, however, is the same. Applying a non-depleted pump analysis, we assume that the pump amplitude, A_0, remains constant and is always much larger than the sideband amplitudes of A_+ and A_-. Equations 6.17 and 6.18 then approximately become

$$\frac{dA_+}{dz} = -iC_+ \left(2|A_0|^2 A_+ + A_0 A_0 A_-^* e^{-i\Delta z}\right), \tag{6.19}$$

$$\frac{dA_-}{dz} = -iC_- \left(2|A_0|^2 A_- + A_0 A_0 A_+^* e^{-i\Delta z}\right), \tag{6.20}$$

where relatively small terms have been discarded and constant terms have been grouped into constants C_+ and C_-. Next the equations are simplified by a moving coordi-

nate system, which is achieved with the substitutions $A_+ = B_+ e^{-i2C_+|A_0|^2 z}$ and $A_- = B_- e^{-i2C_-|A_0|^2 z}$:

$$\frac{dB_+}{dz} = -iC_+ A_0 A_0 B_-^* e^{i2|A_0|^2(C_+ + C_-)z - i\Delta z}, \tag{6.21}$$

$$\frac{dB_-}{dz} = -iC_+ A_0 A_0 B_+^* e^{i2|A_0|^2(C_+ + C_-)z - i\Delta z}. \tag{6.22}$$

Expanding the complex quantities into a magnitude and angle as $B_+ = \rho_+ e^{i\phi_+}$ and $B_- = \rho_- e^{i\phi_-}$ yields three real equations:

$$\frac{d\rho_+}{dz} = C_+ A_0 A_0 \rho_- \sin\theta, \tag{6.23}$$

$$\frac{d\rho_-}{dz} = C_- A_0 A_0 \rho_+ \sin\theta, \tag{6.24}$$

$$\frac{d\theta}{dz} = 2A_0 A_0 \left(C_+ + C_-\right) - \Delta + A_0 A_0 \cos\theta \left(C_+ \frac{\rho_-}{\rho_+} + C_- \frac{\rho_+}{\rho_-}\right), \tag{6.25}$$

with $\theta = 2A_0 A_0 \left(C_+ + C_-\right) z - \Delta z - \phi_+ - \phi_-$. The growth of ρ_+ and ρ_- are maximized when θ stays constant at $\frac{\pi}{2}$. Setting $\theta = \frac{\pi}{2}$ and $\frac{d\theta}{dz} = 0$, Equation 6.25 becomes

$$2A_0 A_0 \left(C_+ + C_-\right) = \Delta. \tag{6.26}$$

MI gain is expected to occur when the condition of Equation 6.26 is satisfied. This is demonstrated in Section 6.4.

6.3 Resonant Cavity Analysis Method

In this section the analysis method for finding the modulation instability gain in a resonant cavity is detailed. Section 6.2.2 described the use of coupled differential equations, solved numerically, to calculate the MI in a freely propagating wave. Mirrors are now added to each end of the propagation distance to create a cavity that resonates at some wavelengths.

6.3.1 Cavity Boundaries

The fields can be translated across the cavity boundaries using matrix techniques. To use this method, we represent the field on each side of a boundary by a vector consisting of the forward-traveling wave, E^f, and the backward-traveling wave, E^b. From the electromagnetic boundary conditions, the relation between the vectors is

$$\begin{pmatrix} E^f \\ E^b \end{pmatrix}_{Side1} = \frac{1}{\tau} \begin{pmatrix} 1 & \rho \\ \rho & 1 \end{pmatrix} \begin{pmatrix} E^f \\ E^b \end{pmatrix}_{Side2}, \tag{6.27}$$

where ρ and τ represent the reflection and transmission coefficients of the boundary, respectively, from side 1 to side 2. These coefficients can be made complex-valued to represent phase-shifting reflective structures.

6.3.2 Optimization-Based Solution Method

The solution procedure is outlined in Figure 6.1. There are 12 complex variables made up of the forward and backward traveling waves at both sides of the cavity at the three frequencies. We will assume that there are no waves coming in from the right side, so $E_0^{b,R}$, $E_+^{b,R}$, and $E_-^{b,R}$ are all held constant at zero. Also, the waves entering from the left side, $E_0^{f,L}$, $E_+^{f,L}$, $E_-^{f,L}$, are set to known values. This leaves six complex variables, representing the reflected and transmitted waves, to be solved. Since each complex variable contains two components, there are 12 unknowns.

Values are assumed for the six complex variable and then the calculations are performed to find if the case is balanced. First the external variables are translated inside the cavity using Equation 6.27. The internal field values are represented in Figure 5.1 with tildes. Then variables $\widetilde{E_0^{f,L}}$, $\widetilde{E_+^{f,L}}$, and $\widetilde{E_-^{f,L}}$ are used as starting values in the coupled differential equations. Either Equations 6.13-6.15 or 6.16-6.18 can be used. The resulting values are compared with $\widetilde{E_0^{f,R}}$, $\widetilde{E_+^{f,R}}$, and $\widetilde{E_-^{f,R}}$ for a match. Similarly, the

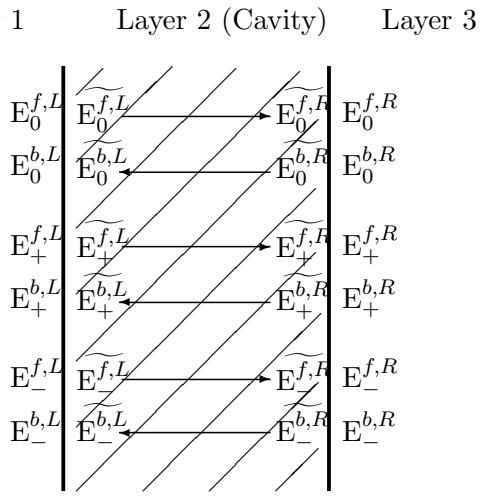

Figure 6.1: Solution method for MI in a single cavity. External fields are translated to internal cavity values.

backward traveling waves at the right interface are propagated across the cavity and the results compared with the values at the left interface. The six comparisons will show no differences in values for a balanced case, meaning that the set of values is self-consistent with all of the boundary conditions and the nonlinear equations. If the comparisons do not yield a match, then an error term can be defined as the sum of the squares of the differences. Optimization methods can then be used to re-assign values to the complex variables to lower the error. I used an algorithm based on the conjugate gradient method [29] to carry out the optimization. Once calculation shows that the error term associated with a set of values is below some pre-set, application-dependent threshold, then those values can be used as the solution.

6.4 Baseline Case

It is instructive to test the equations and methods of Section 6.3 by comparison with a published example. There are no published examples of MI in a resonant cavity, but a favorable comparison with measurements from an open propagation length can

build confidence. Calculations are made here with the parameters presented in [51]. In that paper, spectral measurements are made after 1 kilometer of propagation in a fiber, yielding the plot shown in Figure 6.2.

The parameters of the fiber and the signal used in [51] were used with Equations 6.16–6.17. The nonlinear coefficient of the fiber was given as $1.22 \times 10^{-22} \frac{\mathrm{m}^2}{V^2}$ and the group velocity dispersion is $-4 \frac{psec^2}{\mathrm{km}}$. The input signal power at the wavelength of 1.319 micrometers is 7.1 W over a fiber area of 60 $\mu\mathrm{m}^2$. Assuming an even power distribution over the fiber cross-section gives an intensity of $1.2 \times 10^{11} \frac{W}{\mathrm{m}^2}$. Initial values of 1 $\frac{W}{\mathrm{m}^2}$ were used for the sidebands.

The results of the simulation run are shown in Figure 6.3 and compare well with the measurements of Figure 6.2. The gain peaks are evident in both figures, although they do not align exactly. The discrepancy may be due to variation in the parameters listed with the experimental data. The amplitudes of the sidebands are difficult to compare due to the uncertainty in the starting values. The MI process causes gain, which is what is plotted in Figure 6.3. The measured signal is noise in the fiber that has been amplified by that gain.

The condition of Equation 6.26 can be tested with this case. Curves representing the left side and the right side of the equation are plotted in Figure 6.4. Where they cross is the expected location of the MI gain maximum. The solid curved line is the right side of the equation, which is determined by the material dispersion. The dotted line is a plot of the left side of the equation, and is set by the nonlinear coefficient and the amplitude of the pump wave. Increasing the amplitude of the pump causes the dotted line to rise, moving the cross-over point away from the pump wavelength.

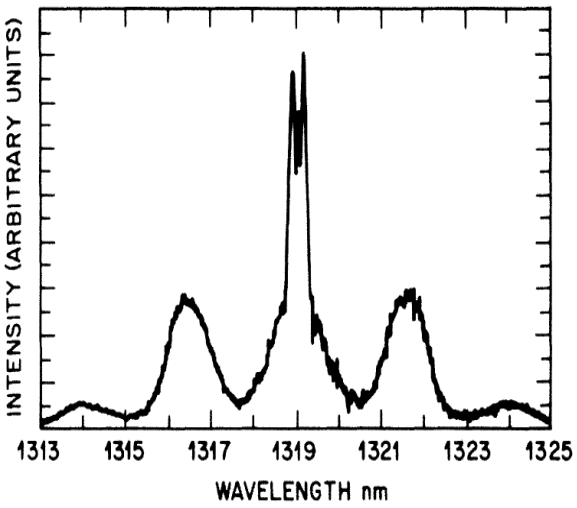

Figure 6.2: Measured spectral output of a fiber, showing MI sidebands. Figure from [51].

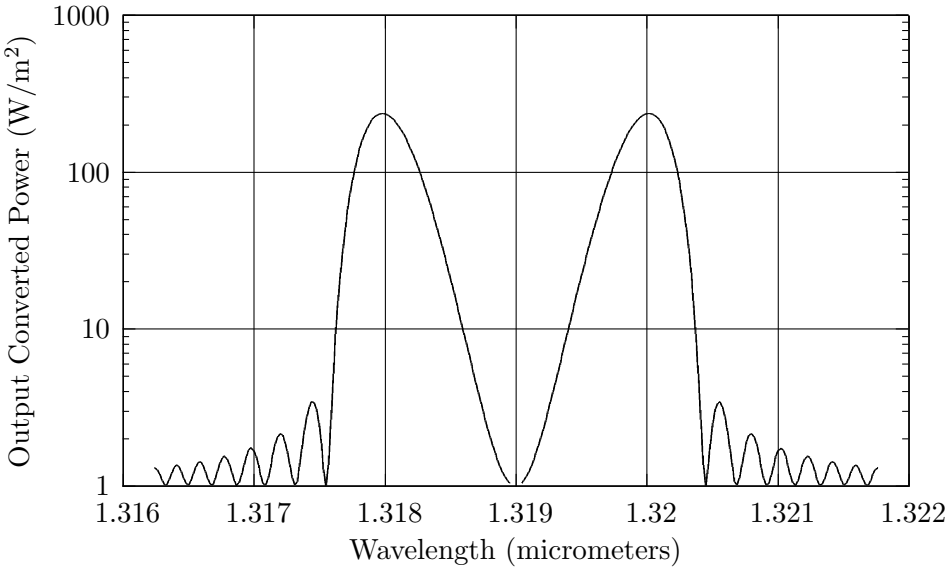

Figure 6.3: Calculated MI output of a length of fiber with parameters as given in the text.

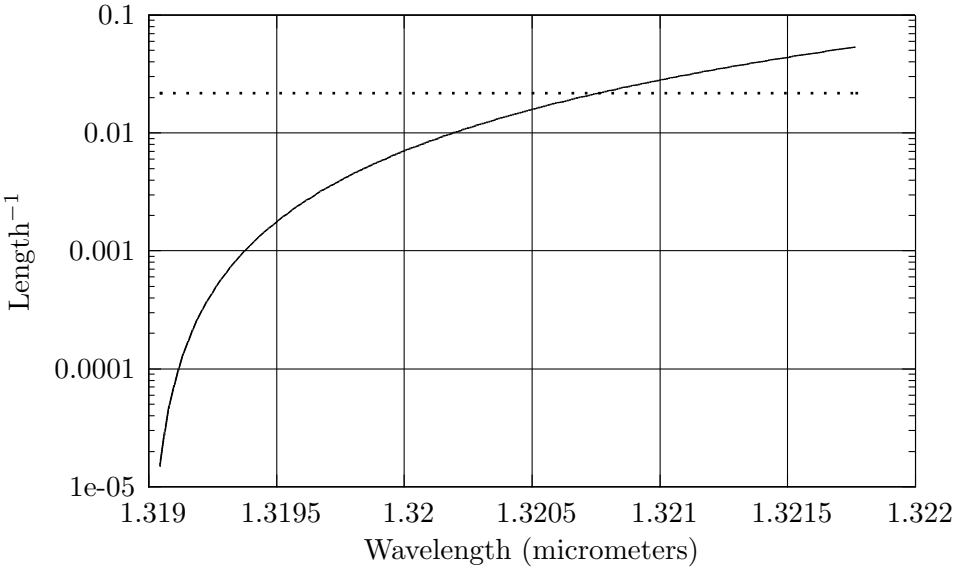

Figure 6.4: Plot of the two sides of Equation 6.26 for the case of Figure 6.3. The solid line is the phase mismatch, which is governed largely by the material dispersion. The dotted line is the left-hand side of the equation, which is determined by the nonlinearity and the amplitude of the pump wave. The maximum gain is expected to occur approximately where the two curves meet.

6.5 Examples

6.5.1 Small Cavity Examples

To clearly show the effects of the resonant cavity on MI, it is instructive first to construct a fictional case. We set the material dispersion and nonlinear coefficient so that MI can be visible over a propagation length of only 10 centimeters (d=$5 \times 10^{-14} \frac{\mathrm{m}^2}{V^2}$, $n'' = -10^{-29} sec^2$, $A_0 = 4 \times 10^5 \frac{V}{\mathrm{m}}$). The free spectral range of the resulting resonant cavity is therefore a visible quantity in the plots. The effect of adding mirrors to the ends of the propagation length are shown in Figure 6.5. The peak of MI gain occurs at the same sideband frequency, although the magnitude is changed and the resonances of the cavity are clearly visible. Increasing the reflection coefficient of the mirrors further increases the MI output.

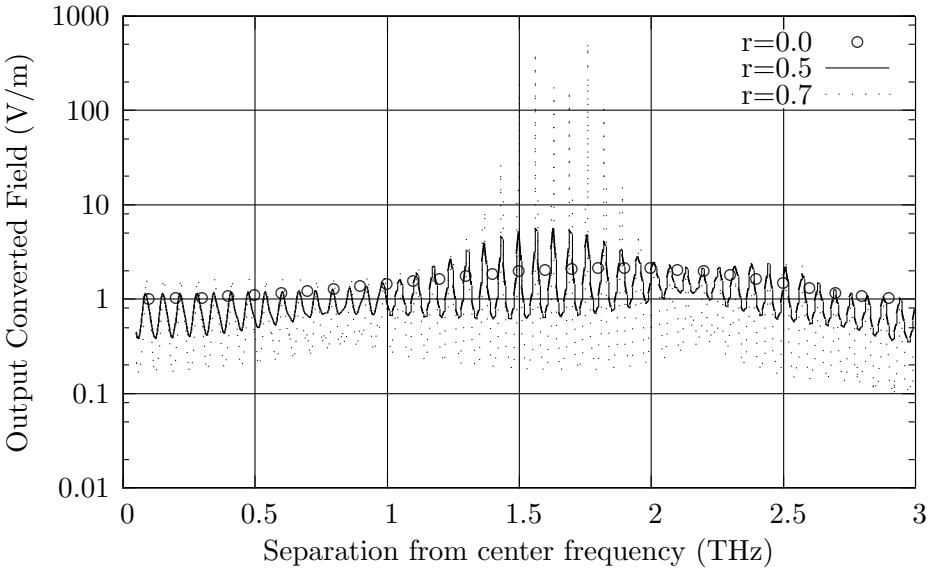

Figure 6.5: Calculated MI output of a 0.01 m cavity, with and without end mirrors. The sideband initial values were 1 V/m. Fictional values of index dispersion and nonlinear constant were used to clearly show the effects of the resonant cavity.

6.5.2 Semiconductor Cavity

Semiconductors have a relatively high nonlinear coefficient (on the order of $10^{-14}\frac{\text{cm}^2}{V^2}$ compared to $10^{-16}\frac{\text{cm}^2}{V^2}$ for glass). This section considers the calculation of MI in semiconductor resonant cavities. Specifically, the material used is gallium arsenide (GaAs), with the pump beam at a wavelength of 1.319 micrometers and amplitude $A_0 = 3 \times 10^5 \frac{V}{\text{m}}$. Figure 6.6 shows the results of several optimization-based calculation runs. The open propagation length without the cavity is a theoretical 2 meter length of GaAs, and shows MI gain. The subsequent data points in the figure are for cavity lengths of 0.2 m and 0.05 m, with the mirror reflectivity increased to compensate for the shorter propagation lengths. As the reflectivity of the end mirrors increases, the frequency of maximum MI gain shifts upward. This is predicted by Equation 6.11, since the pump amplitude, A_0, is higher in a resonant cavity due to the constructive interference of the reflected beams. This analysis shows that MI can be observed in a

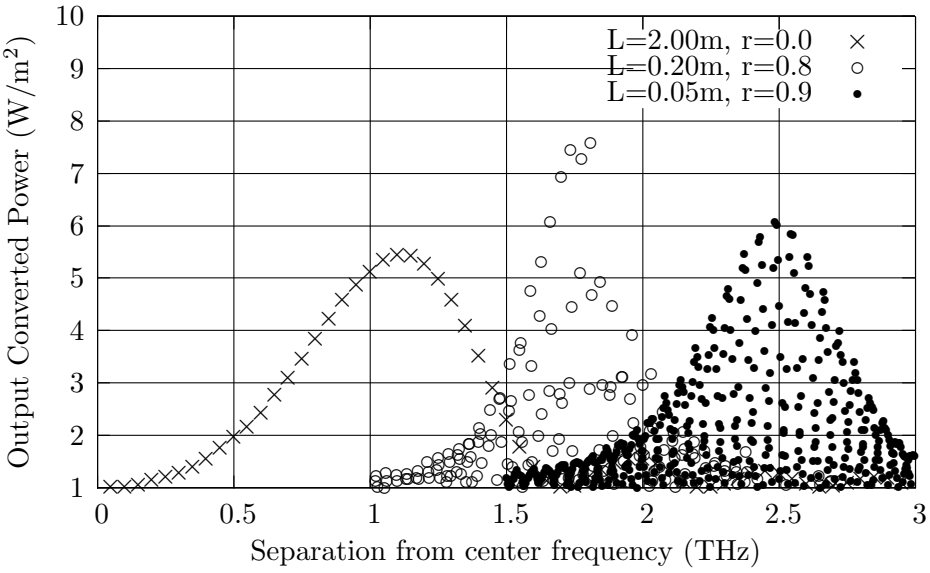

Figure 6.6: Calculated MI output of a GaAs cavity of different lengths and end-mirror reflectivity. The high-finesse cavities have very narrow and closely-spaced peaks, which are only approximately indicated in this figure.

realizable semiconductor cavity if the finesse is sufficiently high.

We can approximately predict the frequency shift of the MI gain maximum in a resonant cavity by using the cavity finesse. The cavity finesse, which is calculated from the mirror reflection coefficient, r, by $F = \pi r / (1 - r^2)$, is approximately equal to the number of interfering beams in the cavity. The pump beam propagating in each direction is therefore increased by a factor of 0.5 F. The reflection coefficients of 0.86 and 0.95 in Figure 6.6 correspond to cavity finesses of 10 and 30. In Figure 6.7 the multiplicative factors of 5 and 15 have been applied to the pump beam amplitude for a propagation length with no end mirrors. It is seen that the frequencies of peak MI gain occur at the same locations as for the resonant cavities of Figure 6.6. The amplitudes of output MI are different, however, due to the different propagation lengths used to generate the two figures.

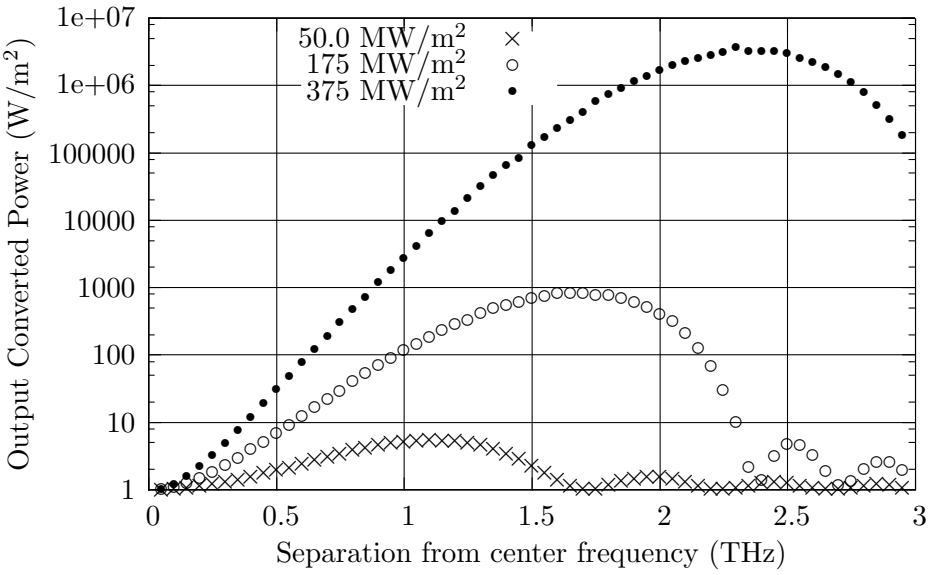

Figure 6.7: Calculated MI output of a GaAs propagation length with no end mirrors. The pump beam is increased in each data set to correspond with the finesses of the resonant cavities in Figure 6.6.

6.6 Summary

By testing trial solutions of the field values and converging on a set of values that satisfies all boundary conditions and propagation equations, we can efficiently solve for the effects of MI in a resonant cavity. The complications involved in a transient analysis or an analytic solution are avoided. For modulation instability in a cavity, the complications can become excessive since each case contains at least six interacting waves, along with all of their reflections. Furthermore, an optimization-based method offers flexibility in the level of approximation made and the effects, such as loss, that can be included. The basic outline of this technique has had success in the field of nonlinear circuit analysis as the harmonic balance method. Applying this new solution method to resonant cavities, shows that the resonance increases the MI output over what would appear in a similar cavity length with no end mirrors. Furthermore, in a high-finesse cavity the pump beam can be increased in magnitude enough to shift the frequency of

the MI gain maximum higher. MI could therefore occur in a relatively short propagation length if there are end-mirrors with sufficient reflectivity and the cavity is in resonance.

7

Conclusions

7.1 Summary

This dissertation has presented a study of several aspects of nonlinear optics in engineered microstructures. While the field of nonlinear optics has been actively pursued since the invention of the laser in the early 1960's, developments in microfabrication have opened new areas of study. Feature sizes that are on the order of an optical wavelength or smaller allow the designer to make use of wave interference effects. By designing these structures, it is possible to overcome the two limiting factors in many nonlinear processes: the small nonlinear constant and phase mismatch.

Methods of enhancing second harmonic generation (SHG) were discussed in Chapter 2. This included using form birefringence to achieve phase matching, using a program based on rigorous coupled wave analysis to perform the calculations. Experiments were also discussed in which SHG was achieved in a material without a second-order nonlinearity by applying a strong DC electric field across a crystal sample. The electric field effectively creates a second-order nonlinearity from a third-order nonlinearity. Chapter 3 concerned a new analysis method for calculating nonlinear effects in a

resonant cavity. This is a significant contribution of this dissertation, and is discussed in more detail below. Chapter 4 then examined the conditions that must be satisfied in engineered microstructures for efficient nonlinear frequency conversion. A method of designing mirrors that have prescribed complex reflection coefficients was presented. As in the method of Chapter 3, the mirror design method is based on circuit design techniques. The new analysis technique is applied to third-order nonlinear processes in Chapter 5. These effects include bistable devices that can exhibit memory. The design and analysis of these types of resonant cavities has been limited by the lack of an adequate technique. Another nonlinear effect in a resonant cavity that has not been adequately calculated is modulation instability (MI), which is described in Chapter 6. The resonance in the cavity is able to affect the MI by changing the magnitude and by shifting the frequency of maximum gain.

A contribution of this dissertation is in the optimization-based analysis method for nonlinear effects in a resonant cavity. There are no other analysis methods that have sufficient generality and sufficient accuracy for the cases we are interested in examining, thereby necessitating the creation of this new method. After a search of available techniques, a method was found that is used by circuit simulators to calculate the response of resonant circuits containing nonlinear elements. That method, called harmonic balance, works by making a guess at branch currents and then testing those values. The currents are used in the linear and nonlinear circuit equations to find the corresponding voltages. The calculated voltages must satisfy circuit rules such as Kirchhoff's Voltage Law. If the set of currents are not satisfactory, an optimization algorithm is used to pick a new set. I translated the outline of this method to nonlinear optics in order to apply it to the cases we are interested in running, and implemented the technique in several C++ programs. A simple optimization algorithm was used which was sufficient for small problems with few unknowns. For larger problems, efficient optimization routines are available and can

be used in the solution.

7.2 Future Directions

Nonlinear optics is a broad field and presents many opportunities for development. The capability of fabricating micrometer-sized structures with precisely designed lengths in particular has opened new areas for exploration. This dissertation examined the design and analysis of several types of nonlinear processes carried out in resonant microstructures, but many others exist. Some of these applications, such as modulators and switches, were listed in the Introduction. The analysis methods used here should be applicable to all of these applications. Besides the design of the nonlinear structure in isolation, the integration of the structure into an optical processing system is also an upcoming field. A surface area of several square millimeters could contain several components such as nonlinear resonators, waveguides, branches and modulators. Ideally, electronic components would also be integrated to create a single processing chip. Silicon, which is widely used for integrated transistors, however, has high material loss for the commonly used optical frequencies. Gallium arsenide is transparent for most infra-red frequencies, and is therefore a more suitable choice for optical components, but is not as widely used in the electronics industry. Other materials, or compounds created by mixing or embedding materials within each other may eventually prove useful for this purpose.

Another conclusion of this dissertation is that much work has been done in other analysis fields that can be applied to nonlinear optics. The computational method presented in Chapter 3 is conceptually related to harmonic balance solvers used to find the performance of oscillating circuits containing nonlinear components. A problem that was inadequately solved in the optical literature has been thoroughly examined in the

circuit literature. Besides this method, there are other radiofrequency (RF) techniques that can be applied to optical applications. For example, cross-modulation effects, when two or more frequencies and their products all interact, are called two-tone (or multi-tone) analyses in RF solvers, and have been widely studied. Optimization-based transient solvers are also in use for nonlinear oscillating circuits and could be applied to nonlinear optics. Section 4.7 described the translation of a linear optical problem into circuit terms so that it could be solved in a circuit simulator. A translation of nonlinear optical problems into circuit terms may also be possible. This would allow the use of commercial circuit solvers, opening new possibilities in the efficient simulation of nonlinear optical devices.

Bibliography

[1] N. Bloembergen, "Nonlinear optics: past, present and future," *IEEE Journal on Selected Topics in Quantum Electronics*, vol. 6, pp. 876–880, Nov. 2000.

[2] E. G. Sauter, *Nonlinear Optics.* New York: Wiley, 1996.

[3] R. W. Boyd, *Nonlinear Optics, 2nd Ed.* San Diego: Academic Press, 2003.

[4] T. H. Maiman, "Stimulated optical radiation in ruby," *Nature*, vol. 187, pp. 493–494, Aug. 1960.

[5] R. C. Jaeger, *Introduction to Microelectronic Fabrication, 2nd Ed.* New Jersey: Prentice Hall, 2002.

[6] J. A. Armstrong, N. Bloembergen, J. Ducuing, and P. S. Pershan, "Interactions between light waves in a nonlinear dielectric," *Physical Review*, vol. 177, pp. 1918–1939, Sept. 1962.

[7] A. Ashkin, G. D. Boyd, and J. M. Dziedzic, "Resonant optical second harmonic generation and mixing," *IEEE Journal of Quantum Electronics*, vol. 2, pp. 109–124, June 1966.

[8] D. S. Bethune, "Optical harmonic generation and mixing in multilayer media: analysis using optical transfer matrix techniques," *Journal of the Optical Society of America B*, vol. 6, pp. 910–916, May 1989.

[9] P. D. Maker, R. W. Terhune, M. Nisenoff, and C. M. Savage, "Effects of dipersion and focusing on the production of optical harmonics," *Physics Review Letters*, vol. 8, pp. 21–22, Jan. 1962.

[10] I. Shoji, T. Kondo, A. Kitamono, M. Shirane, and R. Ito, "Absolute scale of second-order nonlinear-optical coefficients," *Journal of the Optical Society of America B*, vol. 14, pp. 2268–2294, Sept. 1997.

[11] M. M. Fejer, G. A. Magel, D. H. Jundt, and R. L. Byer, "Quasi-phase-matched second harmonic generation: tuning and tolerances," *IEEE Journal of Quantum Electronics*, vol. 28, pp. 2631–2654, Nov. 1992.

[12] J. P. van der Ziel, "Phase-matched harmonic generation in a laminar structure with wave propagation in the plane of the layers," *Applied Physics Letters*, vol. 26, pp. 60–61, Jan. 1975.

[13] J. P. van der Ziel and M. Llegems, "Optical second harmonic generation in periodic multilayer gaas-al$_0$.3ga$_0$.7as structures," *Applied Physics Letters*, vol. 28, pp. 437–439, Apr. 1976.

[14] A. Fiore, V. Berger, E. Rosencher, P. Bravetti, and J. Nagle, "Phase matching using an isotropic nonlinear material," *Nature*, vol. 391, pp. 463–466, Jan. 1998.

[15] L. A. Eyres, P. J. Tourreau, T. J. Pinguet, C. B. Ebert, J. S. Harris, M. M. Fejer, L. Becouarn, B. Gerard, and E. Lallier, "All-epitaxial fabrication of thick, orientation-patterned gaas film for nonlinear optical frequency conversion," *Applied Physics Letters*, vol. 79, pp. 904–906, Aug. 2001.

[16] T. K. Gaylord and M. G. Moharam, "Planar dielectric grating diffraction theories," *Applied Physics B*, vol. 28, pp. 1–14, Jan. 1982.

[17] M. G. Moharam and T. K. Gaylord, "Diffraction analysis of dielectric surface relief gratings," *Journal of the Optical Society of America*, vol. 72, pp. 1385–1392, Oct. 1982.

[18] L. Li, "Formulation and comparison of two recursive matrix algorithms for modeling layered diffraction gratings," *Journal of the Optical Society of America A*, vol. 13, pp. 1024–1035, May 1996.

[19] L. Li, "Use of fourier series in the analysis of discontinous periodic structures," *Journal of the Optical Society of America A*, vol. 13, pp. 1872–1876, Nov. 1996.

[20] G. Klemens, W. Nakagawa, R. C. Tyan, and Y. Fainman, "Phase matching in anisotropic form-birefringent nanostructures," *OSA Annual Meeting, Long Beach*, 2001.

[21] B. P. Antonyuk, "All optical poling of glasses," *Optics Communications*, vol. 181, pp. 191–195, July 2000.

[22] G. H. Haertling, "Plzt electrooptic materials and applications–a review," *Ferroelectric*, vol. 75, pp. 25–55, Jan. 1987.

[23] A. Mukherjee, S. R. J. Brueck, and A. Y. Wu, "Electric field induced second harmonic generation in plzt," *Optics Communications*, vol. 76, pp. 220–224, May 1990.

[24] R. G. Smith, "Theory of intracavity optical second-harmonic generation," *IEEE Journal of Quantum Electronics*, vol. 6, pp. 215–223, Apr. 1970.

[25] A. Calderone and J. P. Vigneron, "Computation of the electromagnetic harmonics generation by stratified systems containing nonlinear layers," *International Journal of Quantum Chemistry*, vol. 70, no. 4, pp. 763–770, 1998.

[26] M. G. Martemyanov, T. V. Dolgova, and A. A. Fedyanin, "Optical third-harmonic generation in one-dimensional photonic crystals and microcavities," *Journal of Experimental and Theoretical Physics*, vol. 98, no. 3, pp. 463–477, 2004.

[27] G. Klemens and Y. Fainman, "Optimization-based calculation of optical nonlinear processes in a micro-resonator," *Optics Express*, vol. 14, pp. 9864–9872, Oct. 2006.

[28] S. El-Rabaie, V. F. Fusco, and C. Stewart, "Harmonic balance evaluation of nonlinear microwave circuits–a tutorial approach," *IEEE Transactions on Education*, vol. 31, pp. 181–192, Aug. 1988.

[29] K. E. Atkinson, *An Introduction to Numerical Analysis*. New York: Wiley, 1989.

[30] W. H. Press, S. A. Teukolsky, W. T. Vetterling, and B. P. Flannery, *Numerical Recipes in C, 2nd Ed.* Cambridge: Cambridge, 1999.

[31] W. J. Tropf, M. E. Thomas, and T. J. Harris, *Handbook of Optics: Volume II*. McGraw-Hill, 1995.

[32] M. D. Sturge, "Optical absorption of gallium arsenide between 0.6 and 2.75 ev," *Physical Review*, vol. 127, pp. 768–773, Aug. 1962.

[33] M. Born and E. Wolf, *Principles of Optics, 7th Ed.* Cambridge: Cambridge, 1999.

[34] A. Yariv, *Quantum Electronics, 3rd Ed.* New York: Wiley, 1989.

[35] C. H. Chen, K. Tetz, W. Nakagawa, and Y. Fainman, "Wide-field-of-view gaas/alxoy one-dimensional photonic crystal filter," *Applied Optics*, vol. 44, pp. 1503–1511, Mar. 2005.

[36] V. Berger, "Second-harmonic generation in monolithic cavities," *Journal of the Optical Society of America B*, vol. 14, pp. 1351–1360, June 1997.

[37] C. Simonneau, J. P. Debray, J. C. Harmand, P. Vidakovic, D. J. Lovering, and J. A. Levenson, "Second-harmonic generation in a doubly resonant semiconductor microcavity," *Optics Letters*, vol. 22, no. 23, pp. 1775–1777, 1997.

[38] F. F. Ren, R. Li, C. Cheng, H. T. Wang, J. Qiu, J. Si, and K. Hirao, "Giant enhancement of second harmonic generation in a finite photonic ctrystal with a single defect and dual-localized modes," *Physical Review B*, vol. 70, p. 245109, Dec. 2004.

[39] R. Haidar, N. Forget, and E. Rosencher, "Optical parametric oscillation in microcavities based on isotropic semiconductors: a theoretical study," *IEEE Journal of Quantum Electronics*, vol. 39, pp. 569–576, Apr. 2003.

[40] C. Diederichs, J. Tignon, G. Dasbach, C. Ciuti, A. Lemaitre, J. Bloch, P. Roussignol, and C. Delalande, "Parametric oscillation in vertical triple microcavities," *Nature*, vol. 440, pp. 904–907, Apr. 2006.

[41] G. Klemens, C. H. Chen, and Y. Fainman, "Design of optimized dispersive resonant cavities for nonlinear wave mixing," *Optics Express*, vol. 13, pp. 9388–9397, Nov. 2005.

[42] S. D. Smith, "Optical bistability: towards the optical computer," *Nature*, vol. 307, no. 3, pp. 315–316, 1984.

[43] A. Szoke, V. Daneu, J. Goldhar, and N. A. Kurnit, "Bistable optical element and its applications," *Applied Physics Letters*, vol. 15, pp. 376–379, Dec. 1969.

[44] D. A. B. Miller, S. D. Smith, and C. T. Seaton, "Optical bistability in semiconductors," *IEEE Journal of Quantum Electronics*, vol. 17, pp. 312–317, Mar. 1981.

[45] G. Priem, I. Notebaert, B. Maes, P. Bienstman, G. Morthier, and R. Baets, "Design of all-optical nonlinear functionalities based on resonators," *IEEE Journal of Quantum Electronics*, vol. 10, pp. 1070–1078, Sept. 2004.

[46] G. Priem, I. Notebaert, P. Bienstman, B. Maes, G. Morthier, and R. Baets, "Resonator-based all-optical kerr-nonlinear phase shifting: Design and limitations," *Journal of Applied Physics*, vol. 97, p. 023104, Dec. 2005.

[47] F. S. Felber and J. H. Marburger, "Theory of nonresonant multistable optical devices," *Applied Physics Letters*, vol. 28, pp. 731–733, June 1976.

[48] J. H. Marburger and F. S. Felber, "Theory of a lossless nonlinear fabry-perot interferometer," *Physical Review A*, vol. 17, pp. 335–342, Jan. 1978.

[49] P. K. Kwan and Y. Lu, "Computing optical bistability in one-dimensional nonlinear structures," *Optics Communications*, vol. 238, no. 1, pp. 169–175, 2004.

[50] A. Hasegawa and W. F. Brinkman, "Tunable coherent ir and fir sources utilizing modulational instability," *IEEE Journal of Quantum Elecronics*, vol. 16, pp. 694–697, July 1980.

[51] K. Tai, A. Hasegawa, and A. Tomita, "Observation of modulation instability in optical fibers," *Physical Review Letters*, vol. 56, pp. 135–138, Feb. 1986.

[52] M. J. Potasek and G. P. Agrawal, "Self-amplitude-modulation of optical pulses in nonlinear dispersive fibers," *Phys. Rev. A*, vol. 36, pp. 3862–3867, Aug. 1987.

[53] W. Huang and J. Hong, "A coupled-mode analysis of modulation instability in optical fibers," *IEEE Journal of Lightwave Technology*, vol. 10, pp. 152–162, Feb. 1992.

[54] T. Tanemura, Y. Ozeki, and K. Kikuchi, "Modulation instability and parametric amplification induced by loss dispersion in optical fibers," *Physical Review Letters*, vol. 93, no. 16, p. 163902, 2004.